

DEVELOPMENT AND MODELING OF A COLONOSCOPY ROBOT

by

Cem Tutcu

B.S., Mechanical Engineering, Yeditepe University, 2011

M.S., Mechanical Engineering, Yeditepe University, 2014

Submitted to the Institute for Graduate Studies in
Science and Engineering in partial fulfillment of
the requirements for the degree of
Doctor of Philosophy

Graduate Program in Mechanical Engineering
Boğaziçi University

2020

ACKNOWLEDGEMENTS

No words can express my appreciation to my thesis supervisor Dr. Evren Samur for his guidance through this thesis and his efforts for my technical development. It is not only his technical expertise that I am inspired by but also his outstanding personality of being patient and humble. A priceless gift of new skills and knowledge I received with his never-ending devotion to teaching. I am also thankful to Dr. Özgür Kocatürk, Dr. Nurdan Tözün, and Dr. Çetin Yılmaz for their guidance and expertise through my thesis work.

I am pleased to work in a very talented workgroup with Bora A. Baydere, Şeref K. Talaş, and Timur Altınsoy, and grateful for their help on developing the robotic system presented in this thesis. I also would like to thank to my friends Hüseyin Demircioğlu, and Onur M. Erkan, for their support and camaraderie.

My special thanks to my family Ümran Tutcu, Erol Tutcu, and Ferah Feza Sümer for their support for all the decisions I made, and their tremendous effort to facilitate my education.

It was such a challenge, but no challenge I am afraid of with support of my beloved wife Sinem Tutcu. I am motivated and filled with life with the love of my newborn daughter Mercan, who allowed me to enjoy even at times with the strongest headwinds. I am looking forward to the days to come when she can read this thesis.

I would like to thank Şeyma Ünal for her never-ending support. I appreciate her patience for long period as I failed to allocate enough attention to this close friendship.

This project is supported by the Scientific and Technological Research Council of Turkey (TUBITAK #115E717)

ABSTRACT

DEVELOPMENT AND MODELING OF A COLONOSCOPY ROBOT

Colorectal cancer is the second leading mortality cause among all cancer types. Similar to the other cancer types, early detection plays a vital role in the prevention of mortality. Colonoscopy is an endoscopic method that is widely used to screen colon, and remove lesions, which is considered to be the most reliable method for detecting colorectal cancer. Conventional colonoscopes are propelled and positioned manually. This operation presents the risk of colon perforation, and patient discomfort due to high reaction forces applied to the colon wall. The conventional approach also often emerges the problem of colonoscope shaft looping inside the convoluted colon that causes loss of haptic feedback from the tip. Due to these post-colonoscopy complications, scans are not performed as frequently as required to mitigate the risks. In this study, a novel robotic solution is proposed for colonoscopy operations that will reduce operational risk, and improve patient comfort which will have an impact to increase colonoscopy scan rate. The robotic system also aims to provide a more ergonomic working environment for the colonoscopist to reduce long term usage complications. This thesis focuses on the colonoscopy robot development; particularly the design of an in-vivo shaft, kinematics and quasi-static modeling of the robot, and a medical application scenario. An experimental study is performed to prove navigation and position control capabilities of the system using a large scale prototype. Experiments showed that wall reaction forces are considerably lower than the conventional colonoscopy. Positioning tests have demonstrated close correlation with a model estimate up to a certain robot body length. This thesis proves the concept of a growing soft robot that can be further developed to be used in colonoscopy in future studies.

ÖZET

KOLONOSKOPİ ROBOTU GELİŞTİRİLMESİ ve MODELLENMESİ

Kolon kanseri, diğer kanser türleri arasında ölüm oranı en yüksek olan ikinci kanser tipidir. Diğer kanser türlerine benzer olarak kolon kanseri için de erken teşhis, kanserin engellenmesi için hayati önem taşımaktadır. Kolonoskopi kolon kanseri görüntülemesinde ve gerektiğinde kanserli dokunun alınmasında kullanılan en güvenilir metoddur. Konvansiyonel kolonoskoplar elle kuvvet uygulanarak ilerletilmektedir. Bu uygulama şekli kolon duvarına aşırı kuvvet uygulayarak hastada acı ve ağrıya ve bazı nadir durumlarda kolon perforasyonuna neden olabilmektedir. Hastaların kolonoskopi sırasında ve sonrasında yaşadığı rahatsızlık ve operasyon kaynaklı komplikasyon risklerinden dolayı istenen görüntüleme sıklığına ulaşamamakta, ve bu da bireylerin kolon kanseri riskini artırmaktadır. Bu çalışmada operasyon kaynaklı riskleri azaltacak ve hasta rahatını iyileştirecek bir robotik kolonoskopi sistemi sunulmaktadır. Ayrıca bu sistem doktorlar için daha ergonomik bir çalışma ortamı sunmayı ve uzun süreli kolonoskopi kullanımı sonrası ortaya çıkan komplikasyonları engellemeyi amaçlamaktadır. Bu tez çalışmasında yeni bir kolonoskopi robotu geliştirilmiş olup özellikle in-vivo shaft tasarımı, kinematik ve quasi-statik modelleme, ve olası medikal kullanım için konseptin doğrulanma çalışmalarına odaklanılmıştır. Konsept, navigasyon ve pozisyon testleri ile büyük ölçekli bir prototip kullanılarak bir in-vitro test düzeneği üzerinde kanıtlanmıştır. Deneysel çalışma robotik kolonoskop sisteminin duvara uyguladığı kuvvetin konvansiyonel yöntemle göre düşük olduğunu göstermiştir. Model sonuçları pozisyon testlerinde alınan ölçümlerle karşılaştırılmış ve belirli bir robot uzunluğuna kadar uyumlu oldukları gösterilmiştir. Bu tezde kavramsal kanıtlaması yapılan yumuşak ve uzayabilen bir robotun, gelecekteki çalışmalarda kolonoskopi uygulaması için kullanılma potansiyeli gösterilmiştir.

TABLE OF CONTENTS

ACKNOWLEDGEMENTS	iii
ABSTRACT	iv
ÖZET	v
LIST OF FIGURES	viii
LIST OF TABLES	xvi
LIST OF SYMBOLS	xviii
LIST OF ACRONYMS/ABBREVIATIONS	xxi
1. INTRODUCTION	1
1.1. Motivation	1
1.2. Objectives	4
2. LITERATURE REVIEW	6
2.1. The Colon and Conventional Colonoscopy	6
2.2. Improvement Areas for Colonoscopy	8
2.2.1. Complications on Patient and Success of the Operation	9
2.2.2. Long Term Usage Complications on Colonoscopists	12
2.3. Future Expectation from Colonoscopy	13
2.4. Robotic Colonoscopy	15
2.5. Continuum Robots for Potential Colonoscopy Application	25
2.6. Continuum Robot Modeling	32
2.7. Novelty of proposed robotic system	34
3. MATERIALS & METHODS	40
3.1. The novel growing soft robot	40
3.1.1. System Design	42
3.2. Modeling of Growing Soft Robot	45
3.2.1. Kinematic Model	46
3.2.2. Quasi-static Model	48
3.2.2.1. Shaft stiffness	50
3.2.2.2. Static equilibrium	52

3.2.3. Stiffness FEA Model	56
3.3. Prototypes	56
3.3.1. Actuation Mechanism and Robot Body	57
3.3.2. Actuator Tubings	66
3.4. Validation Testing	70
4. RESULTS	75
4.1. Kinematic Model	75
4.2. Quasi-static Model	77
4.3. Path-following simulation	79
4.4. FEA Results Comparison with Analytic Stiffness Model	83
4.5. Robot Body Stiffness and Positioning Experiments	85
4.6. Navigation	89
4.7. Robot Wall Reaction Measurements	91
5. DISCUSSION	95
5.1. Medical Certification Procedure	101
6. CONCLUSION	103
6.1. Contributions and Originality	106
6.2. Outlook and Future Work	107
REFERENCES	108
APPENDIX A: BENDING STIFFNESS EQUATION OF THE INFLATED BEAM	
123	
APPENDIX B: TENDON FRICTION FORCE	126
APPENDIX C: COMPARISON OF ACTUATOR TUBINGS	128
APPENDIX D: MAIN ROBOT CONTROL ALGORITHM	131
APPENDIX E: TECHNICAL DRAWINGS	133

LIST OF FIGURES

Figure 2.1.	The large bowel. The large bowel is divided into sections as sigmoid colon, descending colon, transverse colon, ascending colon, and cecum.	7
Figure 2.2.	Conventional colonoscope. Main components of the conventional colonoscope are insertion tube, control body, light guide/umbilical cord, and connectors.	7
Figure 2.3.	Endoscope holding method. (a) Insertion tube is held by the right hand, and universal chord goes between the torso and the left forearm. (b) Control hub is manipulated by the left hand.	8
Figure 2.4.	Colonosight system working principle.	17
Figure 2.5.	AeroScope working principle.	18
Figure 2.6.	Neo Guide robotic colonoscopy system.	19
Figure 2.7.	Invendoscope working principle.	19
Figure 2.8.	Medrobotics flex robotic system.	20
Figure 2.9.	Flex Robotic System Tools.	21
Figure 2.10.	Endotics principle of locomotion.	22
Figure 2.11.	A conceptual image of robotic capsule endoscope (RCE) on the left, and the serial robot that controls the motion on the right.	23

Figure 2.12. Phill Cam capsule endoscopy.	24
Figure 2.13. Trunk-like continuum robot.	27
Figure 2.14. Different configurations of octopus arm-like manipulator.	28
Figure 2.15. Wine-like growing robot working principle.	28
Figure 2.16. Pneumatic flexible robot arm.	29
Figure 2.17. Soft, pneumatically actuated continuum robot.	30
Figure 2.18. Wedge type, roller and slider ball type flexible rod actuators.	31
Figure 2.19. Pneumatic reel actuator.	32
Figure 2.20. Concentric-tube robot.	33
Figure 2.21. Free-body diagram of a bowel section.	34
Figure 3.1. Novel growing soft robot (a) Detailed view of the EE with the pinch roller mechanism. (b) Section view of the robot including the EE and the shaft. The inner and outer sheath are cut at mid-plane to show interior components.	41
Figure 3.2. ROBOCOL overall system features. Outer sheath is not installed in the pictures. (a) Modules of the robot. Servo motors and control valves are located in the control hub placed in-vitro. (b) Features of the robot body and feed unit.	43
Figure 3.3. Pinch roller actuator working principle	44

Figure 3.4.	End effector of target size robot body.	44
Figure 3.5.	Force dimension Omega 6 haptic device.	45
Figure 3.6.	Forward and inverse kinematics functions of the soft continuum robot.	47
Figure 3.7.	Configuration space variables and model coordinate system. (a) The solid cyan line indicates the backbone curve of the soft continuum robot. (b) Actuator positions at the robot shaft hub. Actuators are numbered from 1 to 3.	48
Figure 3.8.	FBD of the EE. Coordinate system x'', y'', z'' is attached to the EE body. Normal vector \tilde{n} is always collinear with the y'' direction.	51
Figure 3.9.	FBD of the robot in two dimensions. (a) The EE and the shaft are joined together. (b) The EE is separated from the shaft to show reaction forces.	53
Figure 3.10.	HDPE uniaxial test data. Material behavior is more suitable for Yeoh hyper-elastic model due to the shape of the function.	55
Figure 3.11.	Single tubing and robot shaft FEA models, mesh and BCs.	57
Figure 3.12.	Single DOF prototype. Pinch roller drive mechanism is attached on a linear guide. The actuator tube is connected to pressure compressor. The test setup is used to prove pinch roller drive concept and test various actuator tubings.	58

Figure 3.13.	2D Prototype. CAD model on the left and manufactured assembly on the right. The assembly body is actuated by two pinch roller drive mechanisms that allow prototype to perform translation and rotation.	59
Figure 3.14.	Basic maneuvers of 2D prototype.	60
Figure 3.15.	Improved version of 2D prototype. (a) Aft looking forward view (b) Side view (c) Solid model of exploded view (d) Top view of the prototype assembled to in-vitro section.	61
Figure 3.16.	End effector of first 3D large scale prototype (PV1). Components are manufactured via 3D manufacturing from PA 12 material. . . .	63
Figure 3.17.	Assembly of the PV1. Robot is composed of three modules as air control unit, feed unit, and robot body.	64
Figure 3.18.	Schematic of air control unit, and feed unit.	65
Figure 3.19.	End effector of PV2. Layout of the features in radial direction is optimized to reduce total diameter of the end effector. Alignment between inflated tubing center and roller clamp edge is improved by implementing additional features.	66
Figure 3.20.	Prototype (PV2) features.	66
Figure 3.21.	. Components of the end effector shown on left and small scale end effector assembly is shown on right.	67

Figure 3.22.	Medical PA12 balloon welded using method 3 as explained above. On the connection area conical features can be observed. As also seen in the figure melted material accumulated and generating additional thickness at the weld edge.	68
Figure 3.23.	1D test setup. Generated force is measured via ATI Nano-17E load cell, and inflation pressure is measured via pressure sensor.	71
Figure 3.24.	2D test setup. The test setup is used to measure generated force by the 2D end effector and speed of the system for a 60° span.	72
Figure 3.25.	Schematic for validation tests performed with PV1. (a) Bending test, (b) force generation test, (c) speed test.	73
Figure 3.26.	Test setup for wall reaction measurement. (a) Top view of the test setup. Measurement coordinate system is depicted on up right corner. (b) Side view shows the marble spheres under the platform that allows frictionless planar motion.	74
Figure 4.1.	Shape of the soft continuum robot for four different goal points numbered as shown (length in millimeters). Curvature κ is given in mm^{-1}	76
Figure 4.2.	Model parameters for the four goal points given in Figure 4.1. (a) Actuator and backbone lengths. (b) Actuator bending moments. (c) Tendon tension forces at the root of robot shaft. (d) Friction forces applied by tendons on robot body.	76

Figure 4.3.	Iterative deformation correction shown with an exaggerated demonstration in 2D plane (a) Body shape and goal points plotted for each iteration (b) Magnitude of the error vector plotted on a logarithmic scale.	77
Figure 4.4.	The EE follows the blue solid spline path in the direction shown with arrows from point 1 to point 14. Black dashed curve shows the path that the EE follows if the shaft deflection correction is not applied.	79
Figure 4.5.	Robot control parameters at the 14 via-points given in Table 4.2 and plotted in Figure 4.4. Here $E = 1.5GPa, v = 0.3, d_{act} = 16mm, t = 0.088mm, a = 26mm, m_{roller} = 0.2, m_{tendon} = 0.1$	81
Figure 4.6.	Model parameters at the 14 via-points given in Table 2 and plotted in Figure 9 where $r=1=k$. Here $E = 1.5GPa, v = 0.3, d_{act} = 16mm, t = 0.088mm, a = 26mm, m_{roller} = 0.2, m_{tendon} = 0.1$	82
Figure 4.7.	(a) Massless EE following a linear path with 12 via-points on the xy plane. (b) Change in tendon tension forces and bending stiffness of the robot shaft for each via-point on the path.	82
Figure 4.8.	Comparison of FEM results to analytical calculation for single tubing. Solid curve represents analytic calculation and dashed curve represents FEM result.	83
Figure 4.9.	Comparison of FEM results to analytical calculation for whole robot body. Solid line represents analytic calculation and dashed line represents FEM result.	84

Figure 4.10.	(a) Measured force-deflection relationship (solid lines) compared to model estimation (dashed lines). Shaded area is the standard deviation. Measurement curves also represents the positioning error occurred due to deflection of robot body for various tip loading and body lengths (b) Positioning error after deflection correction. . . .	86
Figure 4.11.	Error between measured positions and model estimate for given goal points. Each node is plotted to the goal point coordinate and color of the node indicates error.	87
Figure 4.12.	2D prototype navigation on closed maze path.	89
Figure 4.13.	2D prototype navigation on open maze path.	90
Figure 4.14.	PV2 Navigation camera image.	91
Figure 4.15.	PV1 navigation tests. Lifting weight of 200 g (a) Navigation through open space (b) Passing through narrow obstacle and reaching to target (c) Entering to a tunnel and meets with the target (d) Following a closed cavity maze.	92
Figure 4.16.	Wall reaction force measurement.	93
Figure 4.17.	Robot progress in the maze during wall reaction measurements. . .	94
Figure A.1.	Inflated beam FBD.	123
Figure B.1.	Infinitesimal tendon element.	127
Figure C.1.	Actuator tubings tested as given in Table C.1.	129

Figure C.2.	Comparison of tubing force generation. Tests performed using 1D test setup. Force is normalized per the cross-section area that the pressure is acting on (a) Ranking of tubings per various significant application parameters	129
Figure D.1.	Main state control algorithm	132
Figure E.1.	Small scale end effector roller technical drawing.	133
Figure E.2.	Small scale end effector moving base technical drawing.	133
Figure E.3.	Exploded view of small scale end effector	134
Figure E.4.	Technical drawing of small scale end effector	135

LIST OF TABLES

Table 2.1.	Colonoscopy Quality Indicators	11
Table 2.2.	Competencies for alternative technology against conventional colonoscopy. 14	
Table 2.3.	Comparison of ROBOCOL with the robotic systems presented in literature.	36
Table 2.4.	Comparison of ROBOCOL with continuum robots presented in literature.	38
Table 3.1.	Large scale 3D prototype dimensions.	62
Table 3.2.	Tested off-the-shelf medical tubings. Only tubings that showed potential to be used in prototypes, and have length above 1000mm are listed in this table.	68
Table 3.3.	Prototype size comparison.	73
Table 4.1.	Model results for goal point 2 from Figure 4.1 where $(x, y, z)=(180, 180,0)$ with and without end effector weight and external load. $E = 1.5$ GPa, $\nu = 0.3$, $d_{act} = 16$ mm, $t = 0.088$ mm, $a = 26$ mm, $\mu_{roller} = 0.2$, $\mu_{tendon} = 0.1$	78
Table 4.2.	Coordinates of via-points for the spline path shown in Figure 4.4. .	80
Table 4.3.	Robot control parameters for the goal points as also plotted in Figure 4.11.	88

Table C.1. Actuator tubings tested for prototypes. Vendor information is not given for the tubings fabricated in house. The table also contains information for the off the shelf tubings that have length below 1000 mm. Dimension are in mm. 128

LIST OF SYMBOLS

a	Edge length of triangle formed by equally spaced actuator centers
A_0	Inflated tube cross-section area
d_{act}	Actuator diameter
\vec{d}_i	Radial distance of each actuator from body centerline
\vec{e}_i	Radial distance between the end effector center and the point where tension is applied
E	Modulus of elasticity
f_1	Transfer function between actuator space and configuration space
f_2	Transfer function between configuration space and task space
f_1^{-1}	Inverse transfer function between actuator space and configuration space
f_2^{-1}	Inverse transfer function between configuration space and task space
\vec{F}_{crit}	Critical buckling force
\vec{F}_{ext}	External force applied on the end effector
\vec{F}_{f1}	Friction force of tendon number one
\vec{F}_{f2}	Friction force of tendon number two
\vec{F}_{f3}	Friction force of tendon number three
$F_{lateral}$	Lateral force applied on robot body
F_p	Pressure force
G	Modulus of rigidity
I	Second moment of area of the inflated tubing
J	Polar moment of inertia
K_b	Shaft stiffness
l_1	Length of actuator number one
l_2	Length of actuator number two
l_3	Length of actuator number three

l_b	Length of robot backbone
k	Beam shear coefficient
\vec{M}_1	Bending moment of pressurized tubing number one
\vec{M}_2	Bending moment of pressurized tubing number two
\vec{M}_3	Bending moment of pressurized tubing number three
\vec{n}	Normal vector of end effector direction
P	Actuator pressure
\vec{P}_1	Pressure of actuator number one
\vec{P}_2	Pressure of actuator number two
\vec{P}_3	Pressure of actuator number three
r	Radius of robot backbone
\vec{r}_b	Position vector between point 0 and shaft tip center
\vec{r}_i	Position vector between point 0 and the point where resultant friction and normal forces apply on the robot shaft
R_y	Reaction force in y direction
R_{xz}	Reaction force in xz plane
t	Inflated beam thickness
\vec{T}_{01}	Tendon tension of actuator number one at root
\vec{T}_{02}	Tendon tension of actuator number two at root
\vec{T}_{03}	Tendon tension of actuator number three at root
\vec{T}_1	Tendon tension of actuator number one at end effector
\vec{T}_2	Tendon tension of actuator number two at end effector
\vec{T}_3	Tendon tension of actuator number three at end effector
x	Goal point coordinate in x direction
y	Goal point coordinate in y direction
z	Goal point coordinate in z direction
α	Shaft slope at certain axial location
γ	Shaft rotational deflection
δ	Deflection of cantilevered inflated tubing at tip
Δs	Finite length element of the robot body

θ	Angle between z' and the straight line between origin and goal point
κ	Curvature
μ	Friction coefficient between tendon and robot body
ϕ	Rotation angle with respect to fixed frame axis

LIST OF ACRONYMS/ABBREVIATIONS

1D	One Dimensional
2D	Two Dimensional
3D	Three Dimensional
ACU	Air Control Unit
CC	Constant Curvature
CIR	Caecal Intubation Rate
CRC	Colorectal Cancer
CT	Computer Tomography
DOF	Degree of Freedom
EE	End Effector
ESD	Endoscopic Submucosal Dissection
FBD	Free Body Diagram
FIT	Faecal Immunochemical Test
FPGA	Field Programmable Gate Array
FU	Feed Unit
gFOBT	Guaiac-based
HDPE	High Density Polyethylene
ID	Inner Diameter
LDPE	Low Density Polyethylene
MR	Magnetic Resonance
NRCL	Nurse Reported Comfort Levels
OD	Outer Diameter
PE	Patient Experience
PE-W	Worse Patient Experience
PRA	Pinch Roller Actuator
RMSE	Root Mean Square Error
RTOS	Real Time Operating System
SEPT9	Septin-9

SMA	Shape Memory Alloy
VC	Variable Curvature

1. INTRODUCTION

In this thesis, a novel growing soft robot is developed for a possible colonoscopy application. Colonoscopy is considered the most reliable method for detecting colorectal cancer (CRC) which is one of the most commonly observed cancer types. The growing robot aims to improve colonoscopy application by reducing patient pain and discomfort, and allowing more ergonomic and enhanced control for the colonoscopist during the operation. The system utilizes the benefit of the growing locomotion mechanism that forms the robot body from the tip, reducing the reaction forces between the colon wall and the robot body. The proposed robotic system has a novel actuation system providing higher dexterity for end-effector position control than the similar benchmarks in the literature that provides higher dexterity for end-effector position control.

1.1. Motivation

CRC is the third most common cancer, has second-highest mortality rate among all cancer types in the world [1]. Based on the recent data from the World Health Organization 1,849,518 new cases, and 881,000 deaths were reported in 2018 related to colorectal cancer, considered as a major global health thread [1]. The severity of CRC is distributed such that more than two-thirds of all cases, and approximately 60% of all deaths are observed in countries with high or very high human development index (HDI) as introduced in [2]. American Cancer Society provides an update of CRC occurrence by model-based projection on new cases and mortalities [3]. According to the study, although the incidence rate is showing a decreasing trend over the years, incidence quantity is expected to increase due to increased population. Estimations show that approximately 147,950 individuals will be diagnosed with CRC, which will result in 53,200 mortalities in 2020 only in the USA [3]. Furthermore, the global effect of colorectal cancer is expected to increase to more than 2.2 million new cases and 1.1 million deaths by 2030 [4].

The initial form of CRC is observed as pre-existing benign polyps, that occur due to genetic alterations in normal colonocytes. Further accumulation of genetic abnormalities through a long period time yields some polyps to enlarge, that turn into invasive malignancy [5]. If the polyp is identified in the early asymptomatic stage, it can be removed providing almost 90% 5-year survival when compared to 5% if identified at a later phase [6].

CRC screening play a vital role in early identification of benign polyps leading to high survival rates. Although colonoscopy is considered to be the most reliable method for screening, there are numerous non-invasive screening methods such as assessment of genetic risk, fecal occult blood testing, computer tomography (CT) colonography, and fecal DNA testing. Furthermore, there are also few methods as emerging new screening technologies such as identifying methylation of septin-9 (SEPT9) marker that is under evaluation in the screening setting and capsule endoscopy which is a non-invasive direct visualization method. Types of the non-invasive CRC screening methods are compared in detail, and their shortfalls against conventional colonoscopy are also highlighted in [5]. One of the non-invasive methods that support conventional screening procedure is predictive genetic testing that can be offered to identify the risk for individuals to triage them to appropriate screening such as colonoscopy considered as an effective approach in cancer prevention. Fecal occult blood test is a frequently performed screening method that aims to detect subtle blood loss in the gastrointestinal tract. Two types of fecal occult blood tests performed namely guaiac-based (gFOBT) which is the conventional type, and faecal immunochemical test (FIT) that was developed to improve the sensitivity and expected to replace gFOBT for the future. It is shown in the literature that annual, or biennial gFOBT testing reduces CRC mortality by 16% if performed at least two or three rounds, however, this method has limited sensitivity for cancer and poor performance in detecting adenomas. To test the performance of FIT a comparative study performed on 1256 participants who had both FIT tests and colonoscopy. The study showed that only on 37% of FIT-positive participants had advanced adenomas or cancer, and on 6.5% of FIT-negative participants had advanced adenomas or cancer. Another non-invasive method that is used for CRC

screening is CT colonography due to its $> 90\%$ sensitivity for cancer and polyps > 1 cm, however, it is not approved for CRC screening in the USA because the method is incapable of detecting small or flat polyps. If CT colonography results are found to be positive colonoscopy is required for further investigation. Fecal DNA testing is offered as another non-invasive method that has been underdeveloped aiming to identify specific genetic changes to identify polyps and cancers. Recent comparative testing with FIT showed that fecal DNA test had sensitivity approximately 20% higher than FIT for each category of a lesion with higher false-positive rates. Capsule endoscopy is a preferred method since it allows direct visualization and safe application. A feasibility study for capsule endoscopy is performed compared with conventional colonoscopy. According to the comparative study results, sensitivity for capsule endoscopy was 89% for polyps > 6 mm, and was 88% for polyps > 10 mm. Capsule endoscopy is a safe method for visualization that does not require sedation, intubation, or air insufflation [7]. However, capsule endoscopy has challenges due to poor visualization, and not controllable as the colonoscopy.

Colonoscopy is considered to be the gold standard for the detection of colorectal polyps and other colonic disease, and applied as the final step in all CRC screening pathways regardless of the type of prior non-invasive screenings performed on the patient. The colonoscopy approach allows a direct visualization and therapeutic intervention for removal of polyps, and precancerous lesions. Colonoscopy as a flexible endoscopic approach is performed with an insertion tube carrying a camera on the tip for imaging. The colonoscope tip is positioned by pulling and pushing the flexible tube manually and maneuvered by the bending section of the insertion tube located at the distal end. The bending section is actuated via pull wires and controlled by the knobs on the control section located at the proximal end. The flexible tube also includes a working channel that is used for introducing tools for therapeutic intervention. Sensitivity of colonoscopy is measured as ranging from 75% (95% CI, 63-84%) to 93% (95% CI, 88%-96%) for detecting adenomas > 6 mm [8]. Based on a statistical study, colorectal cancer screening with stool test was 11%, and 61% for colonoscopy for the individuals aged 50 years and older in 2018 in the USA that shows colonoscopy having

a major role in CRC screening. The study also shows that colonoscopy prevalence is increased significantly that is tripled from 20% in 2000 to 61% in 2018 [3]. American Cancer Society recommends sigmoidoscopy every five years and colonoscopy every ten years after the age of 50 for early detection of colorectal cancer [9]. High demand for colonoscopy in the healthcare business is growing, thus attracting researchers to improve the procedure. Colonoscopy is considered a reliable option for CRC screening procedure but has risks at both patient and operator end. The method is prone to development mainly for improving locomotion and maneuverability, imaging, tissue interaction, and reducing pain/discomfort. The introduction of robotics in colonoscopy has been addressing the points of improvement by offering enhanced locomotion, high dexterity tissue manipulation, advanced imaging, and electronic control with haptic feedback.

1.2. Objectives

The objective of this thesis is to develop a soft growing robot that has a potential use in colonoscopy application to overcome the challenges and risks that emerge through the colonoscopy operation. Specific aims of the thesis are given as following.

- Designing and manufacturing in-vivo section of robotic colonoscope
- Developing kinematic and quasi-static models and validating with prototypes
- Performing literature survey and facilitating collaboration with medical authorities through development of the proposed robotic approach for possible medical application

The purpose of developing this robotic approach is to mitigate patient pain and discomfort, reduce complication risks such as colon perforation, and facilitate more ergonomic operation for the colonoscopists. The concept is introduced to the literature by Talas *et al.* [10], Tutcu *et al.* [11], and Baydere *et al.* [12] where the novelty of the system is discussed by comparing to similar solutions presented in the literature. This thesis provides information related to the design and modeling of the proposed

system. Experimental results are assessed for proving the concept and validating the system for a possible colonoscopy application per colonoscopy requirements and future expectations as reported in the literature.

The literature survey is performed in Chapter 2 for both robotic colonoscopes, and the continuum robots that may have the potential to be used in a colonoscopy application. In Chapter 3 design details of the system, prototypes, and validation test setups are presented. Also kinematic and quasi-static model is given in 3 which is used to position the robot end-effector at a given goal point. Results of the model, experimental measurements are given in 4. In discussion, possible use of the proposed system for colonoscopy application is substantiated.

2. LITERATURE REVIEW

The literature review presented in this chapter aims to provide background regarding the comparison of the proposed method with conventional colonoscopy, robotic colonoscopy, and continuum robots in the literature. Furthermore, the need for an improved colonoscopy system is discussed in detail by introducing operational challenges in colonoscopy, and the competencies of a future endoscope.

2.1. The Colon and Conventional Colonoscopy

The large bowel can be divided into several sections for description as sigmoid colon, descending colon, transverse colon, ascending colon, and caecum as shown in Figure 2.1. The length of the large bowel varies in size from an individual to another with an average of 189.5 cm and a standard deviation of 26.3 cm. The length of each colon section is different varying from 34.5 cm (Sigmoid colon) to 75.7 cm (Caecum) with a standard deviation of 7.1 cm and 12.2 cm respectively [13]. The colon wall has a folded structure and connected to the body via elastic ligaments.

Aim of the colonoscopy is to screen the large bowel from the rectum to the caecum and remove any abnormal tissue such as polyps which are the growths on the inner lining of the colon or the rectum. A colonoscope is a flexible shaft carrying a camera for imaging and a working channel, manually guided by the operator inside the colon as shown in Figure 2.2. The Insertion tube is inserted manually from the rectum, and propelled to the Caecum and then retrieved slowly. While colonoscope is propelled and retrieved, the colon wall is monitored, and polyps are removed via a surgical tool which is introduced from the working channel. The colonoscope tip is oriented with the hand-controlled knobs which are connected to the tip via pull wires as shown in Figure 2.2. The colonoscope tip is positioned by pulling and pushing the colonoscope shaft manually.

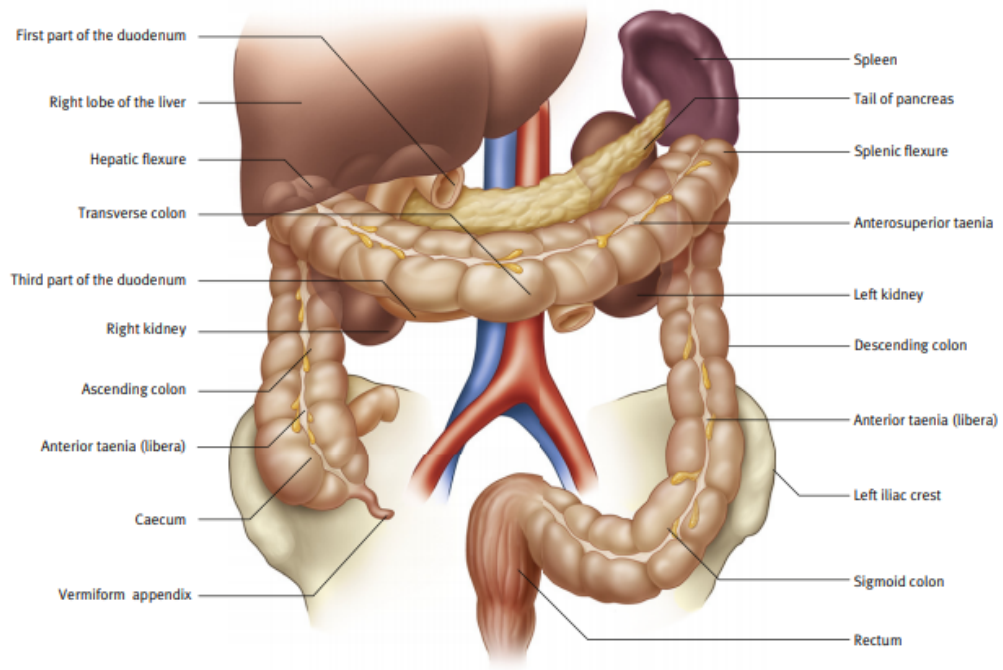


Figure 2.1. The large bowel. The large bowel is divided into sections as sigmoid colon, descending colon, transverse colon, ascending colon, and caecum. Reprinted from [14].

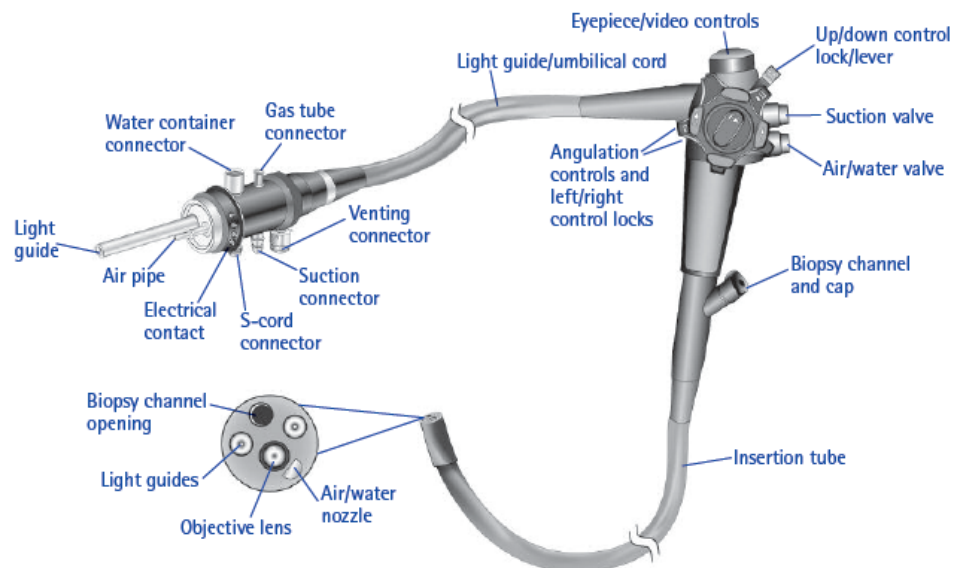


Figure 2.2. Conventional colonoscope. Main components of the conventional colonoscope are insertion tube, control body, light guide/umbilical cord, and connectors. Reprinted from [15].

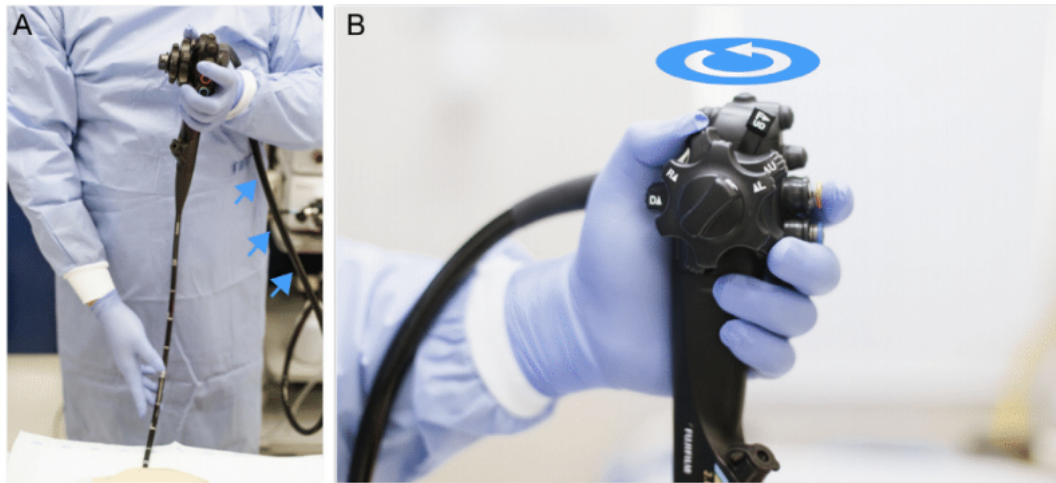


Figure 2.3. Endoscope holding method. (a) Insertion tube is hold by the right hand, and universal chord goes between the torso and the left forearm. (b)Control hub is manipulated by the left hand. Reprinted from [16].

Colonoscopist holds the insertion tube with the right hand, and the universal chord goes between the torso and the left forearm as shown in Figure 2.3. The control body is held by the right hand, and thumbs and fingers are used to manipulate the knobs that maneuver the colonoscope tip, and switches for the controlling suction and air/water valves.

2.2. Improvement Areas for Colonoscopy

Frequent application of colonoscopy for CRC screening merits attention for the improvement opportunities in the method. The risk emerged by the application may be investigated in two main perspectives: (1) complications that occur on the patient such as pain/discomfort or colon perforation, and (2) muscle injuries observed on colonoscopists after long term usage. Besides these risks, there are also challenges causing incomplete colonoscopy due to unidentified polyps and adenomas. Another aspect is the accessibility of colonoscopy related to economic considerations because statistical studies show that low-income populations have lower colonoscopy rate [3].

2.2.1. Complications on Patient and Success of the Operation

Patient discomfort and post colonoscopy complications are often reported in the literature. In the study by Ekkelenkamp *et al.* [17] 17027 colonoscopies performed between 2008 and 2011 are assessed to investigate patient experience. The parameter used to measure pain is NRCL (nurse reported comfort levels) is observed by two nurses attending to the operation such that a score of 5 is given for “Frequent discomfort with significant distress”, and 4 is given for “Significant discomfort experienced several times with some distress”. Other criteria considered in the assessment are the patient experience (PE) which is captured by the recovery nurse before the patient leaves the unit by asking if their experience is better or worse than expected. As the result percentage of patients that experienced significant discomfort during their procedure is ranged from 3.9% to 19.2% (NRCL of 4 or 5). The study also showed that NRCL-45, and PE-W (Worse patient experience) are reducing with increased CIR (Caecal intubation rate) concluding that patient comfort is highly correlated with colonoscopists’ skills [17].

The study by Lee *et al.* [18] compares one-man and two-man methods where for the two-man method colonoscopist controls the direction while the colonoscope is pushed or pulled by the assistant. The patient comfort is measured via scale based on patients’ feedback and a score of 2 is given for “Mild pain; acceptable discomfort; could stand it again”, 3 is given for “Moderate pain; tolerable; but don’t want to do it again”, and 4 is given for “Severe pain, very bad experience; not sure would do again even with more sedation”. Statistical data showed that patients felt less discomfort with the one-man method compared to ones receiving a two-man colonoscopy (2.32 +/- 0.76 vs. 3.17 +/- 0.78). Per the results of this study method followed for the colonoscopy has a significant impact on patient comfort. The two-man method requires coordination of movements thus failure of the on-time synchronization yields more procedure-induced abdominal pain [18]. Although abdominal discomfort is often reported as a complication caused by the operation, in some extreme cases colon perforation is also reported in the literature that emerges a significant procedure-related mortality risk.

Pain and perforation risks emerge due to mechanical forcing applied by the colonoscope causing deformation on the colon defined as ligament stretching, colon stretching, peritoneum stretching in transversal and longitudinal directions. The most challenging areas for scope insertion are the S-shaped sigmoid colon, the U-shaped splenic flexure, the wide U-shaped transverse colon, and the U-shaped hepatic flexure. Among those, the sigmoid colon is the part that covers 77.5% of the instances where the patient experienced pain and discomfort [19]. As the distributed loads causing stretch of the colon and peritoneum, patient discomfort and pain are increased, and more localized forces emerge the risk for colon perforation. The colon is inflated during the procedure for better imaging of surface anomalies that stretches the colon in longitudinal, and transverse directions increasing procedure pain and post-procedure discomfort. Anatomical differences between patients often yield more complex shapes such as looping of the colon. N-loop that occurs on the sigmoid colon is challenging in terms of progressing the colonoscope inside the colon and requires advanced operations to be performed such as straightening of the loop and converting an N-loop to an alfa loop by rotating and pulling the colonoscope. During those operations stretching and pushing the colon causing deformation is also considered to be the source of patient discomfort [20]. According to the survey by Shah *et al.* [19] N-loop is the incident that generates most frequent patient pain as 40% of all incidents, and the second-highest pain source is stretching of the apex of sigmoid with 12%.

According to the studies in literature, patient discomfort is majorly dependent on the colonoscopists' skills and methods followed during the procedure. Practices followed during colonoscopy show large variation between colonoscopists that results in a variation on the colonoscopy quality measures such as CIR, and time required for colonoscopy [21]. It is also reported in the literature that difficulty experienced by the colonoscopist during the procedure is directly related to the pain level as reported by patients [22]. Patient comfort, operation-related complications, and colonoscopy success parameters are significantly impacted by the human performance thus, any improvement to standardize or ease colonoscopist performance will have a positive impact on the colonoscopy quality measures.

Colonoscopy quality indicators are given in Table 2.1 as formed by [23], and summarized in [5]. An incomplete colonoscopy result in failure to meet quality indications, thus, reduces the effectiveness of CRC screening. Reasons for the incomplete procedure are investigated, and the results show that looping of scope and redundant colon have the highest rate as 82.8% among the other reasons such as suspected adhesions, and diverticulosis. As per the literature, colonoscope locomotion and its reaction on the colon wall plays a vital role in the success of colonoscopy, operation quality measures, patient comfort, and mitigation of perforation risk. The robotic approach presented in the study offers improvement for some of the quality measures given in Table 2.1 such as intraprocedure, and post-procedure complications as well as mitigating patient discomfort during the procedure with low mechanical forcing on the colon wall.

Table 2.1. Colonoscopy Quality Indicators [5, 23].

Procedure Phase	Quality Indication
Preprocedure	Appropriate indication Informed Consent Use of recommended surveillance intervals Use of surveillance in UC/CD Bowel preparation
Intraprocedure	Caecal intubation rate Detection of adenomas in asymptomatic individuals Withdrawal times Biopsy specimens in chronic diarrhoea Biopsy samples in UC/BD Endoscopic resection of polys < 2 cm
Post-Procedure	Perforation Bleeding Non-operative management of post-polypectomy bleeding

2.2.2. Long Term Usage Complications on Colonoscopists

The effect of conventional colonoscopy on patient satisfaction has been discussed in many studies, and research focus has been also extended to investigate the impact of the operation on the colonoscopist end. During the operation, the colonoscope is held by three parts: (1) holding or supporting universal cord, (2) holding the control section, (3) holding the insertion tube. When colonoscope held properly, colonoscopists can use all five fingers of the left hand to manipulate the U/D knob, the R/L knob, and press the switches. As the knobs and switches are controlled by the left hand, colonoscopists use their right hand on advancing and withdrawing the colonoscope and maneuvering the inserted tools. Colonoscope holding techniques and the layout in the colonoscopy suite requires colonoscopist to stand near the patient throughout the operation and have a 15-25° below the horizontal line of sight with the monitor [16]. Considering the frequent application of endoscopy with advanced therapeutics, endoscopy related musculoskeletal injuries are often reported in the literature. Suspected risk factors that may yield injuries are mainly due to repetitive hand motion, high hand forces, and wrist, shoulder, and neck postures that are not ergonomic. Adjusting tip angulation controls with the left hand to maneuver the endoscope, torquing with the right hand, and standing for long periods are the major reasons that yield musculoskeletal pain and injury. Static loading occurs on the left hand as the control section is held for prolonged times and fatigued with repetitive pinch/grip forces to manipulate knobs and control the valves. The right hand is used to apply force and torque as the endoscope advances in the lumen [24].

In the literature, it is reported that colonoscopists may apply forces up to 3 kg [25]. According to a statistical survey performed on 684 colonoscopists, 52.9% have experienced an injury related to endoscopy, and 68.5% of the injured colonoscopists required treatment [26]. This shows the significance of the thread of conventional endoscopy on operator health. Neck/upper back pain and thumb pain have the highest percentage among the other types of injuries by 29.3% and 27.6% respectively. The most effective method to mitigate the musculoskeletal injury risk is to approach the problem by intro-

ducing novel solutions that reduce the gravitational load, or novel control mechanisms that can be actuated via lower muscle activity compared to conventional endoscopy.

2.3. Future Expectation from Colonoscopy

Due to its significant role in CRC screening, researchers and medical device manufacturers have been performing studies to improve colonoscopy application for reducing its adverse effect on patients and colonoscopists. Novel devices developed in the literature not only address patient and colonoscopist safety but also aims to improve the performance of the operation according to the colonoscopy quality measures given in Table 2.1, and competencies for alternative new technology as shown in Table 2.2. Considering the prevalent use of conventional colonoscopy a successful alternative solution has to achieve one or more of the following competencies also summarized in [6] while preserving or improving current operational quality.

Currently, research on improved colonoscopy is mainly focusing on overcoming the limitations of the conventional method such as low surgical tool dexterity, limited maneuverability, and locomotion capabilities, lack of haptic feedback from tools, two-dimensional imaging, and poor ergonomics. For therapeutic colonoscopy, tools are inserted from the working channel that allows only one option for the angle of approach to the target tissue. Also, manipulation is done only by bending the tip of the endoscope. Thus, high dexterity surgical tooling is required to ease tissue manipulation and perform complex therapeutic operations. The colonoscope is advanced in the colon by pushing from the proximal end that results in loss of haptic feedback between colonoscope tip and colon as the inserted length increases. Since the colonoscope is maneuvered only by bending the tip, required control over the flexible tube locomotion is not achieved, emerging the risk of tissue damage and excessive forcing together with loss in haptic feedback. A two-dimensional view may also lead colonoscopist to lose the sense of depth, and lead to colon perforation with the absence of haptic feedback.

Table 2.2. Competencies for alternative technology against conventional colonoscopy.

Competency Criteria	Rationale
Eliminating patient pain/discomfort	Patient pain/discomfort is reported mainly due to colon stretching. The operation becomes more challenging due to looping of sigmoid colon that results in more painful colonoscopy. Reducing pain/discomfort is one of the significant parameters that improve patient adherence to CRC screening.
Complication risk mitigation	Although not frequently reported, colon perforation and bleeding may emerge as the operation related complications that has a significant impact on the success of the method when considering the high volume of colonoscopies. A novel approach to the method that reduces mechanical forcing applied to the colon may reduce the complication risk.
Tissue interaction and manipulation	Development of advanced techniques such as endoscopic submucosal dissection (ESD) require advanced systems that have higher dexterity tooling. Robotic approach on tooling may allow better control on tissue manipulation and dissection that reduces complications and reduce operation duration
Colonoscopist musculoskeletal pain and injury mitigation	Long term usage of colonoscopy is yielding occupational complications among colonoscopists emerging as musculoskeletal pain and injury. Complications are the result of high forces that impact upper extremities, and frequent thumb motions for angular adjustment of knobs to control the colonoscope
Improved Imaging	Conventional colonoscopy using white light for imaging that results in miss of some adenomas. Enhanced visualization techniques such as chromoendoscopy, narrow-band imaging, HD GI endoscopy, autofluorescence imaging, and confocal laser endomicroscopy are being developed to improve diagnosis performance. To decrease the possibility of missing any abnormal indications wide-angle lens systems is also introduced that allows colonoscopist to scan a larger surface.
Not requiring bowel preparation	Bowel preparation that is not adequate enough to perform colonoscopy is one of the main reasons for the incomplete colonoscopy. A possible technology that addresses the problem would present an advantage over conventional colonoscopy.

A competitive future application should have enhanced actuation mechanism and maneuver controls with haptic feedback to improve contact forcing between the device and colon [27]. Considering the high frequency of reported complications observed on colonoscopists, there is a demand for a technology that will provide more ergonomic solutions and prevent musculoskeletal injuries.

A novel approach that is targeting to replace conventional colonoscopy is expected to address one or more of the competencies given in Table 2.2 while complying with the economic concerns for success. Statistical studies show that adherence to colonoscopy screening programs is majorly impacted by the income level of the population, and healthcare budget allocated per capita by the government. Any offered novel technology has to be cost feasible to meet the high operation volume. The scalability of the technology is also an advantage such that the same approach could be utilized for different sections of the GI tract, and for patients of different sizes such as pediatrics [6]. Colonoscopists that have been performing operation through many years with the conventional colonoscopy have been developing robust skills called unconscious competence that emerges a challenge to adapt to new technology easily [24]. A technology that can easily be adapted to practice is an advantage that will allow the technology to be penetrated into the market in a shorter time.

2.4. Robotic Colonoscopy

Robotic systems have been introduced for colonoscopy application with the recent advancements in mechatronics and data processing capabilities. Advances in the robotics mitigates operation related risk for both patient and colonoscopist while enabling an ergonomic mapping of surgeon movements to remotely controlled slave arms, and actuators. Such robotic approaches are mainly aiming to improve precision and tooling dexterity, enhance mobility and maneuverability, and utilize haptic feedback from tools to overcome the limitations of conventional technology. Current research is mainly focused on electromechanics control of colonoscope, autonomous locomotion, and robotic driven instrumentation [28].

Development of advanced therapeutic techniques such as endoscopic submucosal dissection (ESD) emerged a demand for high dexterity surgical tooling and advanced control systems. ESD is technically challenging due to incapability of conventional systems such as lack of tissue retraction, triangulation, and coupled movement between camera and tools [27]. A robotic arm system is introduced named “MASTER [29]” that has a hook and a clamp attached to the double channel colonoscope controlled by a master console system via tendons. Animal trials showed that the system is able to perform ESD [29]. A scorpion shaped endoscopic surgical robot is developed by Suzuki *et al.* [30] that is able to adapt NOTES (Natural Orifice Transluminal Endoscopic Surgery), and SPS (Single port surgery). Two miniature robotic arms are located at the tip of the endoscope and driven by the wires. Those miniature forceps are able to provide haptic feedback to the user while interacting with the soft tissue. Another study performed with a surgical platform namely Anubiscope [31] which is equipped with two working channels to introduce surgical instruments. The instruments offer an articulated tip and allow for four degrees of freedom that allows surgical triangulation. A device similar to [31] developed by Swanstorm *et al.* [32] for transgastric surgery that can be used through the gastrointestinal track for visualization and surgical interventions. The tip of the endoscope has three lumens with high dexterity. One lumen is for 4mm flexible optic and the other two lumens are independent movable arms to allow triangulation and complex actions. This device also has a Shapelock technology that allows to fix the position of endoscopy during the surgical operation which provides an advantage on the systems developed by Suzuki *et al.* [30], and Diana *et al.* [31]. Animal experiments performed on pig and results showed that the device is capable of performing transgastric surgery for 100% of the trials. EndoSAMURAI device is developed by Spaun *et al.* that has two independent end effectors with five DOF. In-vitro experiments performed on the tissue models and time required for operation is significantly reduced with EndoSAMURAI compared to the conventional endoscopic method.

Robotic systems offering advanced mobility and maneuverability that mitigates the challenges impacting CIR, and patient comfort and safety while allowing colono-

scopist to operate in more ergonomic positions. The ColonoSight system uses an inflated balloon attached over the colonoscope shaft as the actuator as shown in Figure 2.4 [33]. The balloon so-called sleeve is compressed at the tip of the colonoscope shaft and unfolded as the balloon is inflated. The orientation of the tip is facilitated by the pull wires which also steers the shaft as it proceeds in the colon. The inflated balloon sleeve propels the colonoscope shaft easily with a small amount of colon wall reactions. Once the shaft proceeds, the balloon is released and cannot be compressed and folded back if the shaft needed to be retracted backward, so after reaching the caecum, the shaft is pulled back manually.

Aer-O-scope is one of the diagnostic endoscopes that has a flexible shaft which is equipped with a front-facing camera and a 360 degrees panoramic camera for viewing the sidewalls of the colon [34]. As the system is inserted into the colon, the balloon around the camera is inflated to form an airtight seal with the colon wall. The device is propelled by the air pressure that is supplied into the colon with the pressure gradient generated between the distal and proximal colon as shown in Figure 2.5. The tip orientation is controlled via a joystick. This system does not require the operator to push the colonoscope shaft from the proximal end. Rather the tip is pushed by the pressure created in the colon. The balloon at the proximal end seals the anus, and a pressurized volume is created between the spherical balloons at the distal end. This

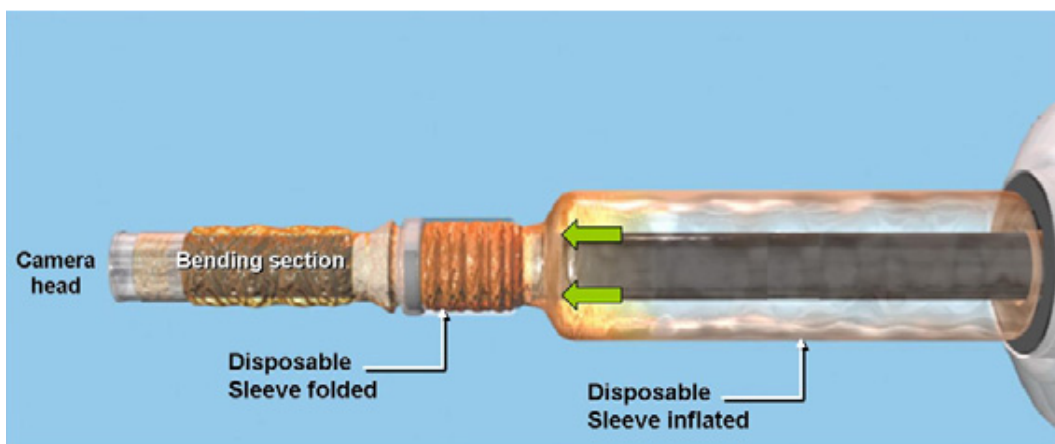


Figure 2.4. Colonosight system working principle. Reprinted from [33].

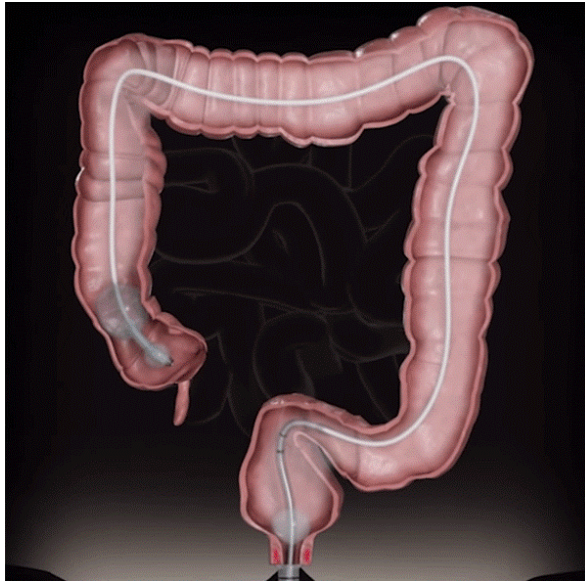


Figure 2.5. AeroScope working principle. Reprinted from [34].

pressure pushes the colonoscope tip that results in reduced reaction forces and reduces the risk of perforation. The study showed that 98.2% CIR is achieved but the polyp detection rate is 87.5% when compared with the conventional colonoscopy [34].

A robotic system named Neoguide (see Figure 2.6) has a colonoscope shaft built by 16 independent components connected in series which are electromechanically actuated [35]. After the colonoscope is inserted manually, the position and orientation of the colonoscope tip are recorded. As the colonoscope is advanced, the computer directs each independent section of the shaft to follow the path traveled by the tip. This design reduces the reaction forces between the colonoscope shaft and the colon wall, improves patient comfort, and decreases the possibility of looping, thus, the operation duration is shortened. However the device is pushed from the proximal end similar to the conventional colonoscopy, so, the advantage emerging from tip actuated systems, stable propulsion, is not considered for NeoGuide.



Figure 2.6. Neo Guide robotic colonoscopy system. Reprinted from [35].

A computer-assisted colonoscope named as Invendoscope shown in Figure 2.7 is based on inverted sleeve technology. The colonoscope shaft is surrounded by an inverted sleeve and actuated by rotary driving units. As the shaft propels, a disposable inverted sleeve covers the outer shaft that maintains the sterilization. The endoscope is pushed from the proximal end similar to the conventional colonoscopy. The tip of the colonoscope is oriented via an electrohydraulic deflection that steers the colonoscope

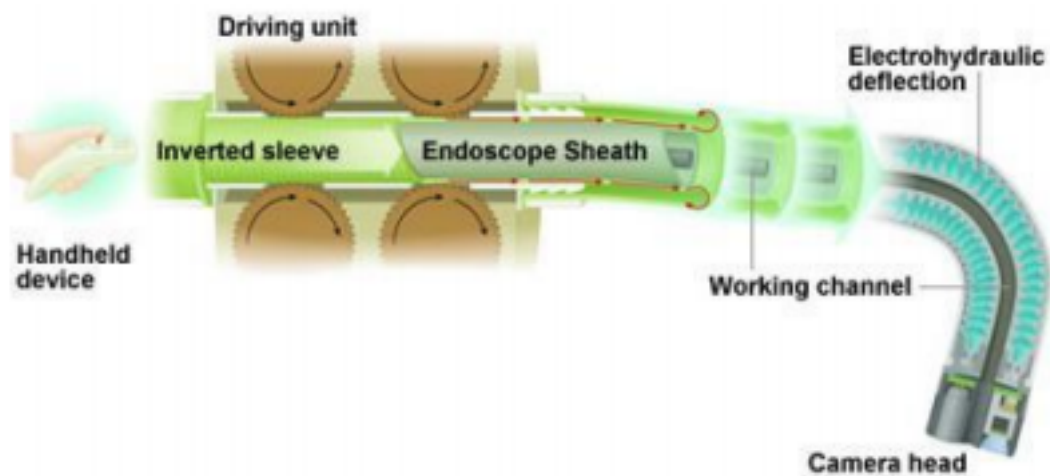


Figure 2.7. Invendoscope working principle. Reprinted from [36].

shaft as it advances in the colon [36]. The system is controlled by a joystick interface. A clinical study performed on 61 patients showed a CIR of 98.4%. [37].

Medrobotics Flex Robotic System has an over tube composed of a ball and cups vertebral segments as shown in Figure 2.8. Articulation is achieved by motorized pull wire systems. An inner spine is used for stiffening the colonoscope shaft, and maintains the shape of the path traveled [38,39]. The flex system does not have a tool channel, and the tools are attached to both sides (see Figure 2.9) of the endoscope tip if needed [40].

i-Snake is one of the active flexible robotic tools having 6 independent segments linked by movable joints. Micromotors embedded within the segments for actuation and provide 7 degrees of freedom by using miniature gears and pulleys. The i-Snake system has a short flexible shaft (20 cm) and a large size of motor segments hinders the minimum radius of curvature that it can achieve, thus limits the dexterity [41]. In the literature, there are also several studies that focused on the active tip concepts such that the tip of the conventional colonoscope is oriented via short flexible shafts that



Figure 2.8. Medrobotics flex robotic system. Reprinted from [38].



Figure 2.9. Flex Robotic System Tools. Reprinted from [39].

improves the steering of the colonoscope such as ColoBot which is a silicon rubber-based robotic tip [42]. Another type of study presents a design that is activated by SMA [43].

The Endotics endoscope presents an inchworm locomotive motion principle. Two anchoring points at distal and proximal ends used alternately for actuation where a vacuum suction behaves as a fixed point for the endoscope body during the motion as shown in Figure 2.10. Clinical trials were performed for this device and showed that Endotics system has a diagnostic accuracy equivalent to the one achievable with the standard colonoscopy. Considering the patient acceptance issue, the Endotics colonoscope showed strongly better results than conventional colonoscopes such that in a scale between 0 to 10 for pain and discomfort, Endotics system ranked between 0.9 and 1.1 while conventional colonoscopes rank 6.8-6.9 [44]. Also, it is stated that the clamping mechanism does not create either lesions in the bowel wall, nor mucosal lacerations. This device can only be used for screening purposes since there is no working channel, and when compared to other systems such as Invendoscope locomotion of the Endotics system is slower [45].

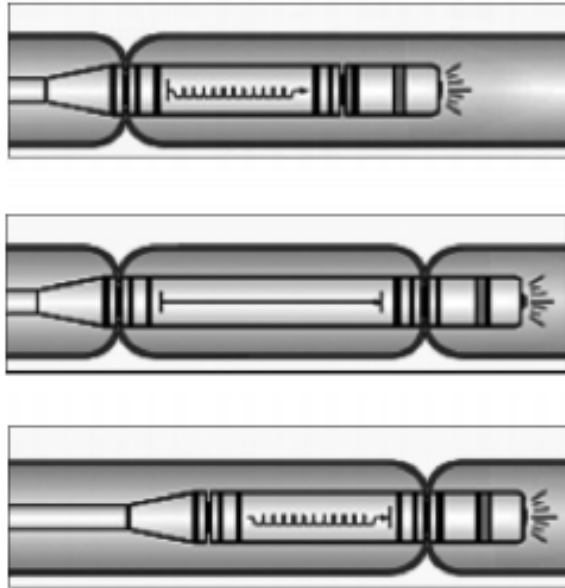


Figure 2.10. Endotics principle of locomotion. Reprinted from [44].

Colonoscopic devices similar to Endotics that are propelled via inchworm locomotion principle are also presented in the literature. A worm-inspired multi-segment robotic endoscope is developed by Bernth *et al.* [46]. This design has higher dexterity compared to the Endotics system since the segments can bend and control the orientation of the camera. Similar to the majority of the inchworm type robots high speeds cannot be reached such that the maximum attainable speed is 1.21 mm/s. In the study by Ortega *et al.* [47] a soft three-modular section robot is developed for colonoscopy application. The robotic colonoscope uses nine independently controlled Shape Memory Alloy springs as its actuators and reaches up to 4 mm/s as the maximum speed. An electrically-actuated worm-like robotic endoscope is introduced by Wang *et al.* [48] composed of three independent segments, and each segment is composed of a linear locomotor with micromotor, turbine-worm, and wire wrapping-sliding mechanism. The robot was tested in-vivo in a porcine model that demonstrated good locomotion capability reaching up to 2.20 mm/s speed. A sliding-inchworm motion mechanism introduced by Yamamoto *et al.* [49] that has a roller mechanism sliding over the rubber tube. The sliding roller mechanism allows the robot to reach higher speeds up to 125 mm/s. This robot is used for inspection purposes only and not designed for colonoscopy ap-

plication, however, the mechanism has potential use for colonoscopy. Caterpillar type robotic colonoscopes propelled by micropillar threads that are actuated by electric motors are presented in the literature [50, 51] demonstrates forward/reverse locomotion up to 40mm/s on the colon mucosa.

A magnetic capsule endoscope is presented by Norton *et al.* [52] which is driven by magnetic field. The capsule is maneuvered by changing the orientation of the the magnetic field with the help of a serial robot positioned outside the body. The serial robot end effector is positioned and oriented based on user input. Since the capsule is pulled from the tip which offers a more stable drive compared to conventional colonoscopy. However, the device does not tool channel, thus, can only be used for imaging. The capsule tip has limited dexterity since it is progressing by contacting and sliding to the colon wall.

One of the emerging technologies in colonoscopy is the capsule endoscopy technique (see Figure 2.12). This method is first introduced in the literature by Iddan *et al.* [53] as an alternative to conventional colonoscopy by reducing discomfort and limitations for advancing enteroscopy. Capsule endoscopy is a tiny device that has a camera, and transmitter. The edoscope screens the inner cavity as it progresses in the digestive system and transmits the image to an outside recorder. The first capsule

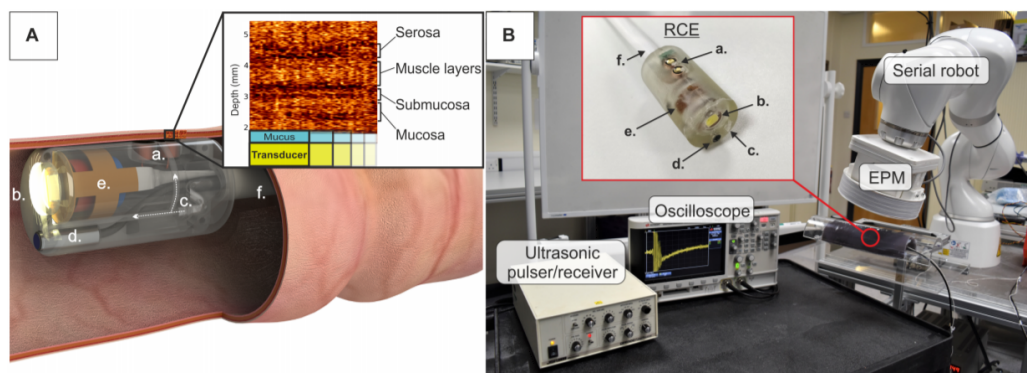


Figure 2.11. A conceptual image of robotic capsule endoscope (RCE) on the left, and the serial robot that controls the motion on the right. Reprinted from [52].

model was approved by the Food and Drug Administration in 2001. The essential indication captured with the initial models was the gastrointestinal bleeding. Further improvement on the system yield superior image resolution and longer battery life that expanded its use to other parts of the GI tract such as the colon [54]. PillCam colon capsule endoscopy is compared with colonoscopy by Schoofs *et al.* [55]. The study shows that colon capsule endoscopy identified 77% of the significant lesions detected by colonoscopy. Similarly in the study by Delvaux *et al.* [56], 82% of the polyps detected by colonoscopy are also detected by the colon capsule endoscopy. This system does not have a maneuver control and is not capable of performing surgical operations such as polyp removal. So, it can only be used for screening purposes with limited success of screening abnormalities [57]. Thus, the future work for this technology is focusing on capsules with therapeutic capabilities, active operator control, and capsules with air inflation ability. [54]. Some examples of these features are already applied such as [58] *et al.* uses the capsule endoscopy for precise drug delivery, a magnetic field controlled capsule is described by [59] and a capsule that release carbondioxide for the colon inflation presented by [60].



Figure 2.12. Phill Cam capsule endoscopy. Reprinted from [57].

Those advanced systems are not only providing enhanced locomotion but also allowing automatization of the procedure such that a future application may progress the colonoscope to the caecum without colonoscopist's control via dark region centralization [61].

2.5. Continuum Robots for Potential Colonoscopy Application

In this section, a literature survey on continuum robots presented due to their possible application on colonoscopy. Soft-continuum robots as invertebrate robots have been an expanding research topic owing to the advantages of invertebrate robots over vertebrate robots in navigating convoluted environments and adapting to their surroundings. Such continuum robots that are inspired by the biology of snakes, tentacles, elephant trunks, and climbing plants have been used in a variety of fields such as urban search and rescue, repair and inspection, and minimally invasive medical procedures [62]. For instance, a continuum robot developed by [63] for minimally invasive inspection in space is suitable for maneuvering in obstructed environments such as cavities under thermal blankets that are largely inaccessible by conventional means. Similarly, [64] developed a flexible tendril continuum robot for on-wing inspection of gas turbines that allows for easy navigation through the narrow gaps between blades and vanes. A mobile hyper-redundant mechanism was presented by [65] that was developed for urban search and rescue missions in areas such as small cracks and pipes. Soft continuum robots are widely used for medical operations such as minimally invasive surgery [66–70], and endoscopic applications [35, 41, 42] due to their compliance to body tissues and the ability to follow curved paths easily.

Unlike conventional articulated robots, soft-continuum robots may provide whole-arm grasping capabilities to manipulate objects of various shapes and sizes [71]. Researchers have successfully developed continuum robots with high navigation capabilities, nevertheless, constant-length configurations lack the ability to comply with the environment as much as growing and extensible continuum robots. Growing robots [72] advance the robot body by adding material whereas extensible robots utilize elastic

deformation or folded structures for extension [73–77]. The disadvantage of constant length of continuum robots is that they introduce a new body into the environment without changing size. Pneumatic growing and extensible continuum robots, on the other hand, offer the ability to extend and contract inside the environment, providing higher dexterity with more stable actuation owing to the forward drive of the robot body. These pneumatic robots have been investigated under two categories, growing and extensible, where the difference is the methodology of body locomotion.

An extensible robot has a variable length, thus, the body is formed inside the working space with compliance to constraints. An example of the extensible soft robot is the trunk-like continuum robot which is actuated by the combination of pneumatic and wire tendons as shown in Figure 2.13 [78]. The trunk has a pressurized central chamber that provides the structural rigidity necessary to make the manipulator useful. Three-wire tendons are placed at equal circumferential spacing and the combination of the displacement of those wires allows the manipulator to bend in any direction.

This concept is considered as advantageous for a colonoscopy application due to its actuation system. Sections of the trunk are actuated via air pressure that pushes the end effector and pulls the rest which reduces the possibility of looping and makes the robot body to comply with the environment. Sections of the trunks may be connected in series to achieve better dexterity such as the continuum robot with a similar approach in [74] as shown in Figure 2.14. This design has a concept very similar to [78] which is actuated by pneumatics and the trunk is oriented via tendons.

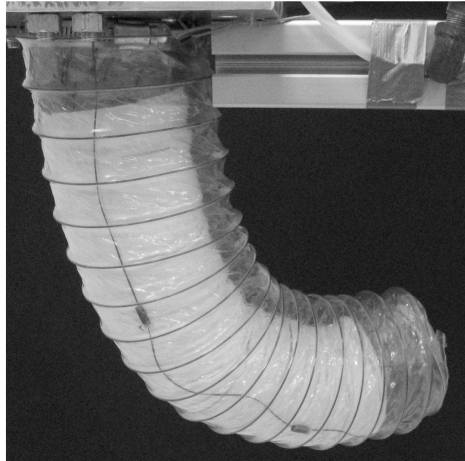


Figure 2.13. Trunk-like continuum robot. Reprinted from [78].

Growing robots differ from the extensible robots, as growing robots build the body from the tip with the material supplied from the proximal end of the robot. While extensible robots are able to extend to a limited length per extension ratio and initial length, for growing robots the limit is the amount of material stocked to build the robot body. An example of growing soft robot is a vine-like robot presented by Hawkes *et al.* [72] as shown in Figure 2.15. The continuum robot is propelled via air pressure inside the hollow sheet, and orientation is controlled by inflating a side of the tubing which turns tip to the opposite side. This concept has the advantage to mitigate looping since the body of the continuum robot is pulled from the proximal side by the air pressure that generates a more stable system for orientation and position control. A soft pneumatic eversion robot that has a working principle similar to [72] is presented by Putzu *et al.* [79].

A pneumatic robot developed in [73] has three pneumatic actuators spaced equally on the circumference as shown in Figure 2.16. The end effector is propelled with the air pressure and the difference between the tube pressures defines the momentum at a certain direction. In this system, the end effector velocities and tube stiffness are coupled, and both controlled by the tube pressures by feeding tubes from the proximal end.

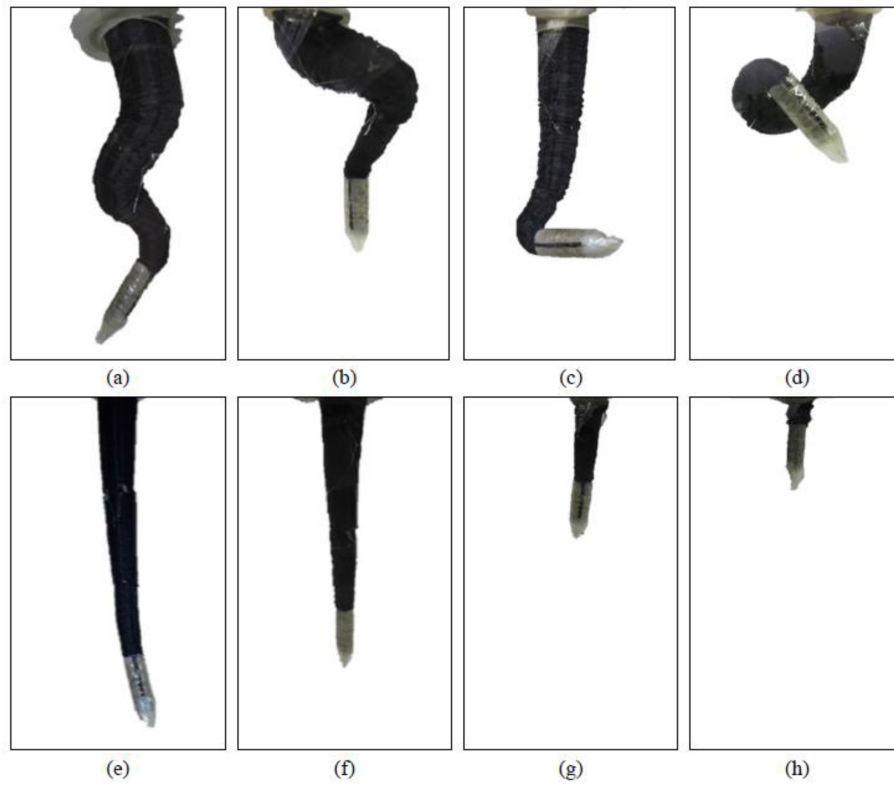


Figure 2.14. Different configurations of octopus arm-like manipulator. Reprinted from [74].

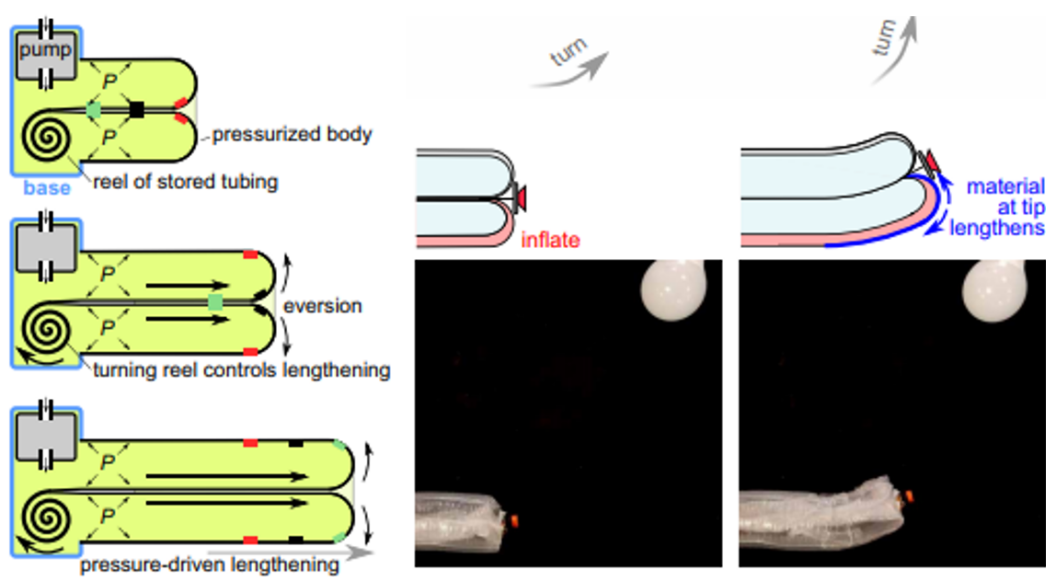


Figure 2.15. Wine-like growing robot working principle. Reprinted from [72].

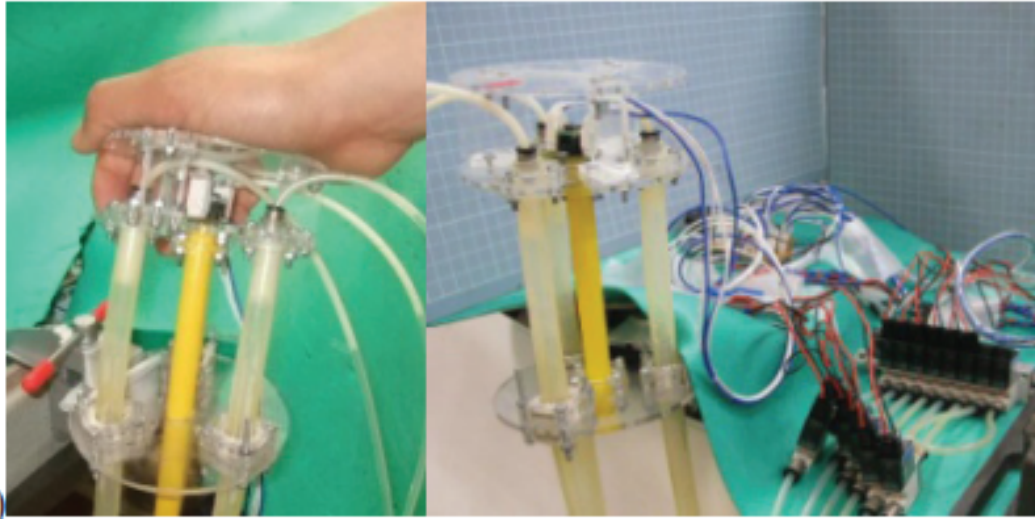


Figure 2.16. Pneumatic flexible robot arm. Reprinted from [73].

A pneumatic actuated soft robot is developed by [76] as a general-purpose continuum robot, which is propelled by the inflation and axial extension of elastic balloons controlled by the pressure. The end effector is propelled via three balloon actuators and end effector orientation is controlled by the length differences of the actuator balloons. This solution is not suitable for colonoscopy application since balloons also expand radially that requires a large robotic shaft diameter. Secondly, latex balloon actuators have a 6:1 strain ratio that creates a 0.33 m unused length for a 2 m shaft. A robotic device similar to [76] is developed by Dehghani *et al.* [80] that is propelled by an inflated latex balloon Figure 2.17. This robot is actuated by single inflated balloon. Thus, end effector orientation control is not possible while the robot presented by Yarbasi *et al.* [76] has orientation control in three DOF. The deflated balloons are stored at the robot tip and expanded as it is inflated, and there is no feature to retrieve back the balloon once it is deployed, so there is no reverse motion. Similar to [76] the robot presented by Dehghani *et al.* [80] has large OD (38 mm) that presented challenges for a colonoscopy application.

Another type of continuum robot is concentric-tube robots. The end effector of the concentric-tube robot is positioned and oriented by rotating and extending pre-

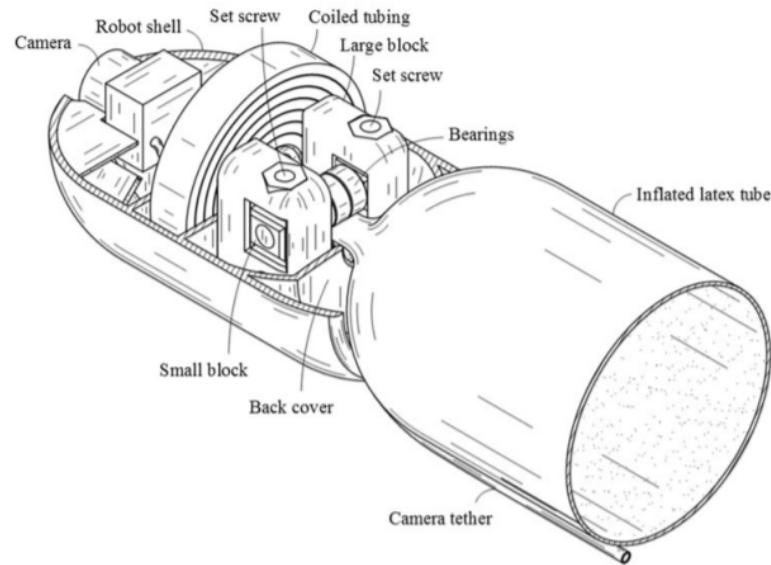


Figure 2.17. Soft, pneumatically actuated continuum robot. Reprinted from [80].

curved elastic tubes. In this approach, the flexible tube comprises of both the links and joints of the robot [67] as shown in Figure 2.20. The end effector is positioned by pushing the concentric tubes from the proximal end that makes the design sensitive as much as the conventional colonoscopes. Similar to the concentric tube robot elephant trunk robot presented by Hannan *et al.* [81] is also pushed from the proximal end to progress end-effector inside the working environment. The elephant trunk robot has constant shaft length and the end effector is oriented via motorized pull wires. The total degree of freedoms is 32 and the manipulator is divided into 4 main sections per the diameters. Various continuum concepts are presented in the literature that is propelled by the push force applied from the proximal end such as tendrill robot [63], tendon-based continuum robot with incompressible flexible rod [82], and the Sensei robot from Hansen Medical [83]. Continuum robots presented in the literature with the STIFF-FLOP [84–86], and layer or particle jamming approach [87, 88] have compliant soft structure however they are not extensible thus, advanced by applying push force applied from the proximal end. Those concepts do not have any advantage regarding looping compared to conventional colonoscopes due to the propulsion method.

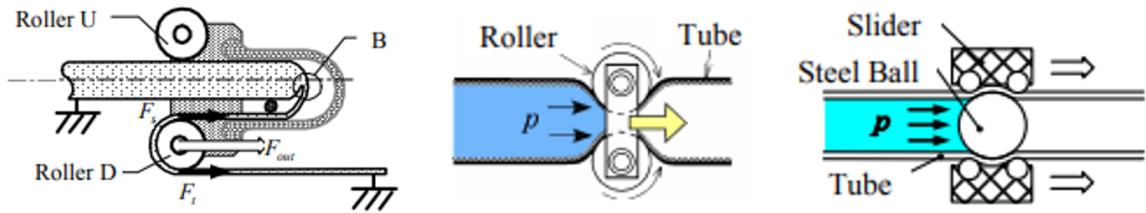


Figure 2.18. Wedge type, roller and slider ball type flexible rod actuators. Reprinted from [89].

A literature survey on pinch roller drive (PRD) is also provided in the thesis since a type of PRD is used on the proposed system. Actuator architectures such as wedge type, roller, and slider ball type flexible rod actuators introduced in [89] as shown in Figure 2.18. The roller actuator mechanism is preferred for the system proposed in this thesis due to its simplicity and low friction. The disadvantage of the roller actuator mechanism against the slider ball actuator mechanism is that better sealing may be achieved with the slider ball concept, however the system is more complex. An example of the roller actuator application is presented in [90]. The actuation system as presented in the study cannot be used for the colonoscopy since the actuator moves on a pre-defined path, however, the actuation mechanism can be used as an example for the proposed colonoscopy robot.

The pneumatic reel actuator presented by Hammond *et al.* [91] is shown in Figure 2.19. The system is actuated via a pressurized flexible tube that is clamped between the roller where the deflated tube is wrapped and backplate. In this system pressure is the only controlling parameter for position speed, and since the deflated tube is wrapped on the pulley it requires a radial space, thus is not applicable for the robotic colonoscope presented in this thesis.

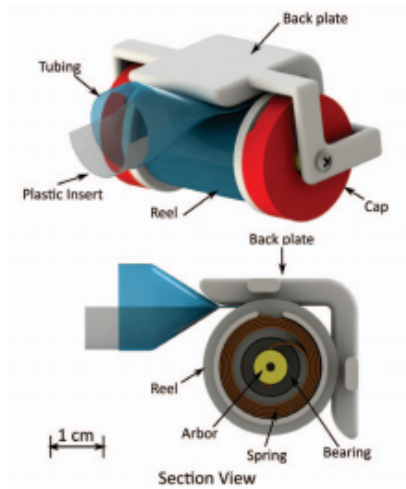


Figure 2.19. Pneumatic reel actuator. Reprinted from [91].

2.6. Continuum Robot Modeling

Although there have been numerous prototypes developed in the literature, modeling of soft-continuum robots has been challenging owing to nonlinear kinematics and dynamics, and large deformations of soft structures. A widely used methodology in kinematic modeling is the constant curvature (CC) approach [75, 92–99]. Studies on the CC approach have shown that the method is an accurate approximation of the continuum robot backbone shape in the absence of out-of-plane external loading [100]. On the other hand, variable curvature (VC) models have been developed as well. They have more complex analytics compared with CC models such as the Cosserat-rod-based models that are frequently referenced in the literature [100–102]. Another approach for VC kinematics was presented by [103] which describes deformation with a finite number of serially connected circular arcs.

A quasi-static mechanical model is developed for concentric tube type robot as shown in Figure 2.20 [104]. Concentric tube robot is modeled by generating the stiffness matrix of each tube and assembling them together. The model considers the effect of external loading and thus the deformed geometry for the robot kinematics since it is a soft robot with flexible shaft.

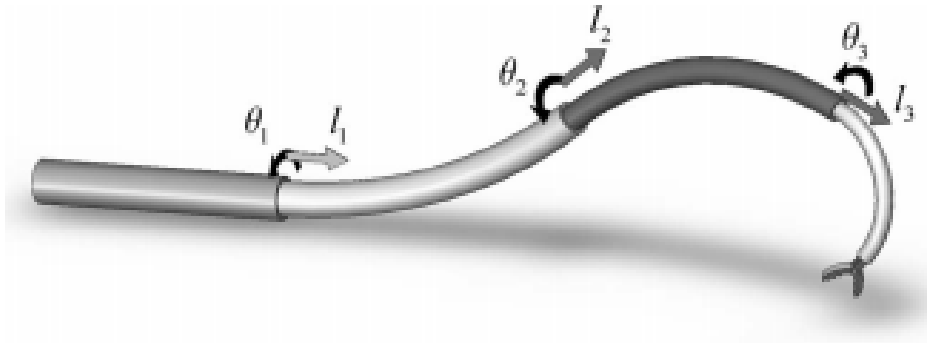


Figure 2.20. Concentric-tube robot. Reprinted from [67].

Similar quasi-static and dynamic continuum robot models have also been introduced in the literature such as the dynamic model of a hyper-flexible robot [105], the quasi-static model of a planar continuum robot [106], statics and dynamics of a continuum robot actuated by tendons [100], and a mechanical model for tendon-driven continuum robots [101]. Although the aforementioned models present solutions on deflections of flexible continuum structures under external or tendon loading, the effect of internal pneumatic pressure on robot body stiffness is not considered.

A dynamic model for Festo's Bionic Handling Assistant was presented by [107]. The bionic hand has three pneumatic actuators placed equally at the circumference that actuates three bellows connected in series. The length of the robot varies, however, limited to a certain length unlike the growing robot presented in this thesis. The dynamic model is developed using the Lagrangian methodology and calculations for the dynamic model are performed after the kinematic transformations. The free-body diagram of the below section of Bionic Handling Assistant is shown in Figure 2.21. The model of the Bionic Handling Assistant incorporates robot section bending stiffness owing to internal pneumatic pressure. Bending stiffness is included in the model via experimental system characterization of the Bionic Handling Assistant sections, which is not applicable for a growing-type robot or any other system with different characteristics. Festo's Bionic arm allows changes in section lengths during bending

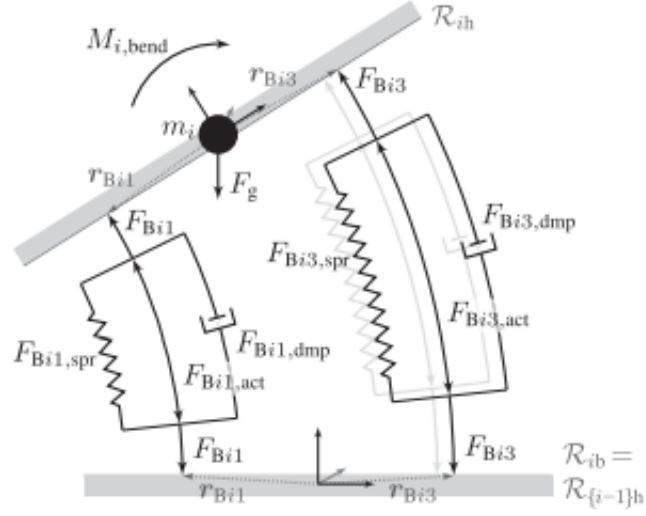


Figure 2.21. Free-body diagram of a bowel section. Reprinted from [107].

but not able to modify within a large range similar to the robot concept presented in this thesis.

Mechanical models presented for OctArm V [102] and soft catheters [108] utilize inflated beam stiffness models that are applicable to other types of pneumatic robot topologies too [109]. Although the effect of internal pressure on robot body stiffness is considered for OctArm V, the model is not applicable to growing-type robots because the actuator length of OctArm V is constant. On the other hand, the soft catheter is a growing-type continuum structure, however, the model presented by [108] is not coupled with a kinematic model.

2.7. Novelty of proposed robotic system

The proposed novel growing robot is providing an enhanced locomotion mechanism by pneumatic actuation from the tip to reduce reaction forces between the end effector and colon. Especially for conventional colonoscopy as the colonoscope shaft gets longer tip becomes insensitive to the push force applied from the proximal end due to high friction and reaction forces applied on the colonoscope body. Such behavior of

conventional system has been emerging difficulties to push the colonoscope inside the colon increasing with the presence of looping even more. The proposed solution push the end effector from the tip and prevent loss in propulsion force at the tip that results in a lower mechanical forcing on the colon. An electromechanical user interface is used to control the robot which allows colonoscopists to operate in a more ergonomic position such as sitting in front of the screens instead of standing while holding the colonoscope. Since the actuation is performed pneumatically and controlled via electromechanical interface there is no need for colonoscopists to apply high forces for pushing/pulling to progress and maneuver the colonoscope. Thus, the proposed system does not require muscle force that results in musculoskeletal injury in conventional colonoscopy. The robotic system targeting to reduce patient pain/discomfort, operation related complication risks as well as a safe and more ergonomic operation for the colonoscopist which are considered as future colonoscopy competencies per Table 2.2.

Although robotic colonoscopy solutions given in literature such as NeoGuide [35], Invendioscope [36] or Flex Robotic System [38] have special features to reduce reaction force on the colon, they are progressed in the colon by the push force applied from the proximal end. Colonosight system [33] propels the colonoscope body by an inflated sleeve that applies the force on the tip similar to the robotic system proposed in this study. The inflated sleeve installed on Colonosight is only used for propelling the body in single DOF and maneuvering is achieved by bending the tip similar to the conventional method. The robotic system proposed in this study has three pressurized tubings that have independent control of length, and stiffness in 3 DOF that allows the whole robot body to bend and fit into the colon geometry. Aer-O-Scope is another robotic colonoscopy system that is propelled by applying the push force from the distal end [34]. Push force on the tip is generated by inflating the colon between two spherical balloons located at the proximal end of the colon and colonoscope tip. Colon inflation that causes strain in hoop direction is considered to be a source of discomfort and pain [20].

Table 2.3. Comparison of ROBOCOL with the robotic systems presented in literature.

Robotic Colonoscopy System	Advantages vs. ROBOCOL	Similarities with ROBOCOL	Disadvantages vs. ROBOCOL
Colonosight	Simpler actuation mechanism	Air pressure pulls colonoscope shaft from tip, stable system	Maneuvered by bending the tip similar to conventional colonoscope. Controlled with single DOF pneumatic actuator. ROBOCOL has higher maneuver dexterity.
AeroScope	Simpler actuation mechanism	Air pressure pulls colonoscope shaft from tip, stable system	Need to pressurize large bowel completely to move the tip. No working channel so performing therapeutic interventions not possible, used only for screening purposes.
NeoGuide	Colonoscope body follows the tip to mitigate looping. More DOFs on the colonoscope body	Robotic application aiming to reduce pain and complications	System is pushed from proximal end that is not stable as tip actuated solutions.
Flex	Inner tube provides stiffness that allows maintaining shaft geometry when needed	Robotic endoscopic application	Short endoscope body (17cm), not suitable for colonoscopy. Tools are attached to two sides of the body since there are no working channels, ROBOCOL is more compact.
i-Snake		Higher maneuvering dexterity compared to conventional colonoscopy	Has 7 DOF rigid links that causes large radius of curvatures
Endotics and Caterpillar type		Architecture is not impacted by looping since propulsion is at proximity of the tip	Slow motion compared to pneumatic actuated applications. There is no working channel thus, can only be used for screening purposes
Phill Cam	No reactions to colon wall		Navigation is not controlled not allowing therapeutic interventions

Inflation pressure of Aer-O-Scope is controlled to maintain safety and the colon reaction force of the system is lower compared to conventional colonoscopy clinical trials are not providing results related to patient comfort during the procedure. This system is only used for screening purposes since the system is designed such that there is no working channel, and tools for therapeutic operations are not available thus, not able to replace standard colonoscopy. Comparison of the robotic colonoscopy systems in the literature to the proposed design in this thesis, namely “ROBOCOL” is summarized in Table 2.3.

The robot presented in this study is an example of growing-type continuum robots with an improved actuation mechanism. Similar to the robot developed by [72], it has the ability to reach very high extension ratios but can also provide active steering through independent control of actuator pressures and tendon tensions separately in three degrees of freedom (DOFs). The robotic system developed in this thesis (ROBOCOL) is compared to continuum robots in the literature since those solutions can also be used for a colonoscopy application.

ROBOCOL architecture is compared with the Trunk-like continuum robot as shown in Figure 2.13 [78]. The difference between Trunk-like continuum robot and ROBOCOL is the proposed concept has three independent pneumatic actuators, unlike the Trunk-like continuum robot which allows independent pressure thus stiffness control in three DOF. Such advantage of the proposed design provides the benefit to control actuator stiffness independent of each other so non-linear robot body shape can also be achieved if needed. The Trunk-like continuum robot is an extensible type robot and the maximum length is limited by the extension ratio. On the other hand, ROBOCOL is a growing type robot and can reach high extension lengths.

The vine-like growing robot [72] has similarities with the trunk presented by Jones *et al.* [78] such as the actuation method; however, the steering is made by inflating tubes rather than pull wires. This concept is also lacking the ability to control pressure and stiffness in multiple DOF which can be achieved by the design proposed in this thesis.

Secondly, the vine-like growing robot has the capability to only bend the tip of the robot, while the robotic system developed in this thesis is able to bend and adjust the geometry of the whole robot body.

Table 2.4. Comparison of ROBOCOL with continuum robots presented in literature.

Robotic System	Advantages vs. ROBOCOL	Similarities with ROBOCOL	Disadvantages vs. ROBOCOL
Trunk, Octopus arm, Vine robot	Simpler actuation mechanism. Larger force can be generated with the same diameter shaft diameter	Air pressure pulls robot shaft from tip, stable system	Motion and stiffness control is coupled and performed only in single DOF.
Pneumatic flexible robot arm	Simpler actuation mechanism.	Air pressure pulls robot shaft from tip, stable system	Velocities and tube stiffness are coupled and both controlled by the tube pressures. Pressure control is less precise than controlling actuator length directly
Concentric tube robot, Elephant trunk manipulator		Soft continuum robot with higher dexterity compared to conventional colonoscope	Pushed from proximal end, same looping risk, and instable propulsion as conventional colonoscopes

The pneumatic driven robot developed by Aliff *et al.* [73] is driven by the tubing pressures in 3DOF. Tubing pressures control both robot shaft stiffness and end effector speed however ROBOCOL offers an advantage by decoupling stiffness and speed control. The robotic concept developed in this thesis presents advantages compared to the continuum robots in the literature due to its unique architecture. Summary of the comparison of ROBOCOL to the continuum robots in the literature is given in Table 2.4.

In this thesis, a quasi-static model tailored for a novel soft-continuum robot that is introduced in Chapter 3 (see Figure 3.1) is presented. The proposed kinematic model is CC type corrected with loading deformations through an iterative process that takes into account the simple analytics of CC while enhancing its accuracy with deformation correction. This study contributes to the literature by proposing a model that can be applied to growing or extensible robots actuated by both pneumatic systems and tendons for which inflated actuator stiffness is a model parameter.

3. MATERIALS & METHODS

This thesis presents the development of a novel growing soft-continuum robot, and a quasi-static model coupled with kinematics. This chapter includes details regarding the features of the proposed robotic system, method for modelling, and validation tests.

3.1. The novel growing soft robot

The proposed robotic system is a growing type of soft robot. The robot body is actuated via pressurized thin-walled tubes using an actuation mechanism called the pinch roller actuator. This actuator consists of an inflatable thin-walled tube pinched between two rollers with embedded bearings as shown in Figure 3.1a. The deflated section of the tube (tendon), which is in tension, travels back through the shaft and is connected to a motor located at the shaft hub. By controlling the motor position, the deflated tube is released or retracted to adjust the length of the pressurized tube. An essential feature of the actuator is that tube pressure does not affect extension. Pressure can be changed to adjust tip force, which in turn affects the smoothness of motion and stiffness of the robot shaft. The underlying mechanism and working principle of the pinch roller actuator is discussed in more detail by [12].

Three actuators are attached at the EE with equal radial spacing around the shaft axis as shown in Figure 3.1a. Inflated tubes are clamped between the rollers to seal airflow, and propulsion force is generated owing to the pressure difference. Roller tightness of each pinch roller mechanism can be adjusted using a tightening screw. Each actuator can be controlled individually to change the length or extension speed of its respective tube and, as such, the position of the robot EE can be controlled by adjusting the lengths of the three tubes. The EE is located at the distal tip of the robot shaft and carries the rollers and hardware required for an intended application such as endoscopy as presented by [110]. Component details are shown in Figure 3.1b where the parts are color coded as follows: red components are moving by growth,

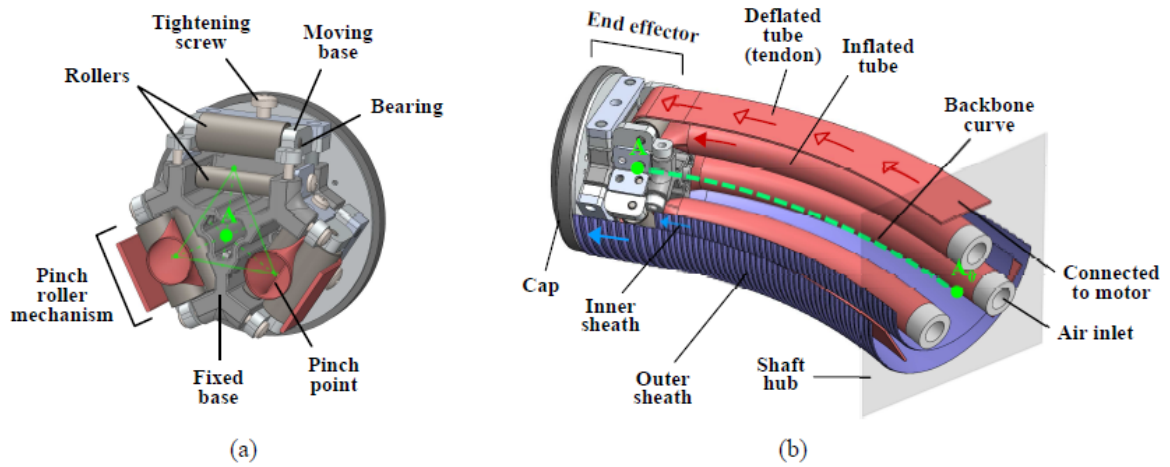


Figure 3.1. Novel growing soft robot (a) Detailed view of the EE with the pinch roller mechanism. (b) Section view of the robot including the EE and the shaft. The inner and outer sheath are cut at mid-plane to show interior components.

blue components are moving by extension, and white components are stationary. Solid arrows represent the direction of growth/extension whereas hollow red arrows show the direction of motion of the tendons as the robot shaft grows. Dashed green line represents the backbone curve, A_0 is the fixed starting point of the curve at the center of the shaft hub, A is the end point located at the centroid of the triangle formed by the three pinch points. For simplicity, point A is taken as the EE tip in the kinematic model because it corresponds to the distal tip of the flexible shaft.

The shaft is the growing section of the robot and includes the inflated and deflated sections of the tubes along with the outer and inner sheaths Figure 3.1b. The inner sheath is placed around the inflated tubes and restricts the movement of the tubes inside the shaft to keep the radial distance between actuator centres relatively constant. The outer sheath covers the whole shaft and is used to keep the tension lines along the deflated tubes in alignment with the backbone. Both sheaths are highly extensible and can extend or retract with the tubes. The imaginary backbone curve that goes through the center of the shaft is shown as a dashed line in Figure 3.1b.

Although the tendon and the inflated tube may be mistaken as separate entities owing to them applying different loads on the robot, they are essentially two sections of a single thin-walled tube. When pressurized from the air inlet, the tube section that stays inside the inner sheath is inflated and is referred to as the inflated tube as shown in Figure 3.1b. The inflated tube applies a propulsion force at the tip. Conversely, the slack section that is located between the inner and outer sheaths remains deflated and is referred to as the tendon because it stays in tension. When combined, each inflated tube/tendon pair constitutes a single actuator.

Growing robot concept has recently emerged in the literature ,and a general definition of the concept is given by [111] as follows: “Growing robots evolve their bodies through the addition of material and locomotion is performed by growing the body, not by external components”. Thus, soft continuum robot presented in this study is considered as growing type since robot grows by adding material from the tip similar to [72, 112, 113].

Independent control of tube pressures and deflated tube (tendon) tensions in three DOFs, and the ability to increase growing range by changing tube length are the main advantages of the novel system compared to similar growing and extensible pneumatic continuum robots proposed in the literature.

3.1.1. System Design

The robotic colonoscopy system is separated into two modules as in-vivo section named as the robot body that is inserted into the colon including end effector and colonoscope shaft, and an in-vitro section named as the control hub including servo motors, spools, and valves as shown in Figure 3.2. Control hub has the sub-modules of the feed unit and air control unit. Deflated tubings as also shown in Figure 3.1 are wrapped around the spools in the feed unit and actuated by the servo motors. Valves and pressure sensors are controlling the inlet pressure of the actuator tubes.

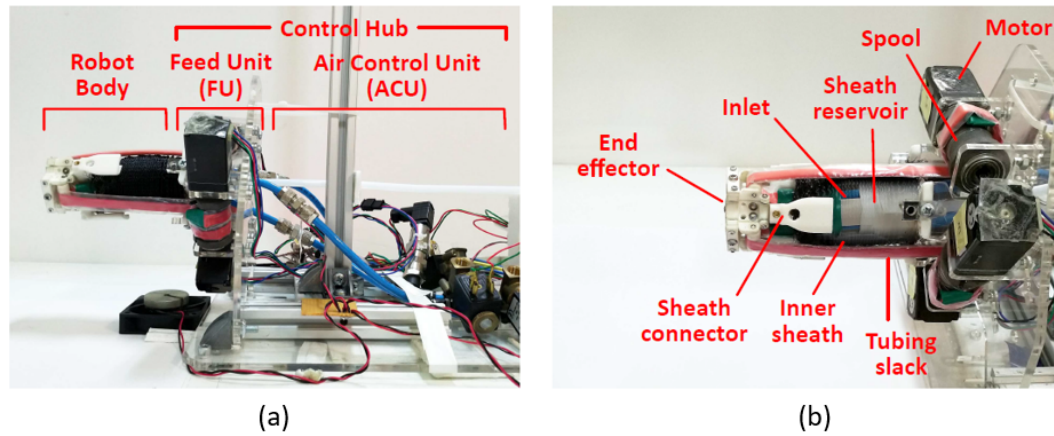


Figure 3.2. ROBOCOL overall system features. Outer sheath is not installed in the pictures. (a) Modules of the robot. Servo motors and control valves are located in the control hub placed in-vitro. (b) Features of the robot body and feed unit.

Conceptual design of the actuation mechanism is shown in Figure 3.3. Balloon actuator is clamped between two rollers, and airflow is sealed at the edge of contact. The balloon is pressurized, and the pressure difference propels the structure which is connected to rollers. Balloon slack section is wrapped to the pulley controlled by the electric motor. Electric motor controls the position and velocity of the actuation system.

Two types of end effectors designed that varies in size but have the same features. A large scale end effector as introduced in [12] is used for validation test. An end effector that has the target dimensions similar to conventional colonoscopy is designed as shown in Figure 3.4 where features of the assembly are introduced. The end effector is composed of three PRA mechanisms and a working channel in the middle. Rollers assembled to the actuator base and moving base with miniature ball bearings. Moving base is constraint with guide pins that can be slid to adjust the gap between two rollers. The tubing passes between the rollers and tightening screw clamps the tubing to generate air seal between inflated and deflated sections of the tube. Plates named as "bearing cover" are assembled to both sides of the actuator base to constraint bearing in the actuator base.

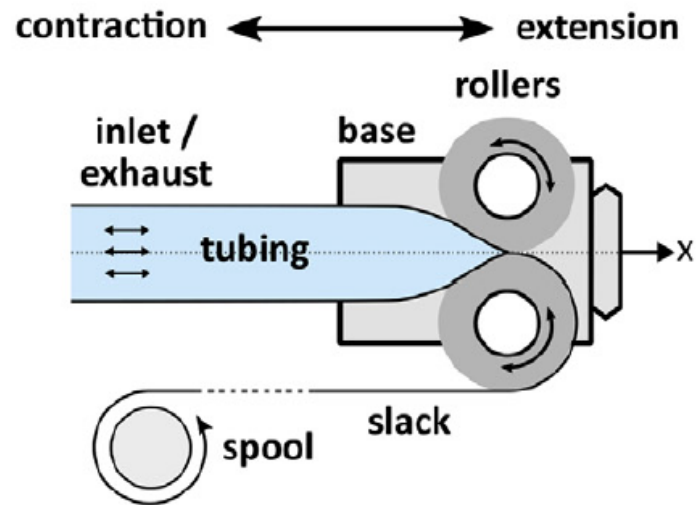


Figure 3.3. Pinch roller actuator working principle. Reprinted from [12].

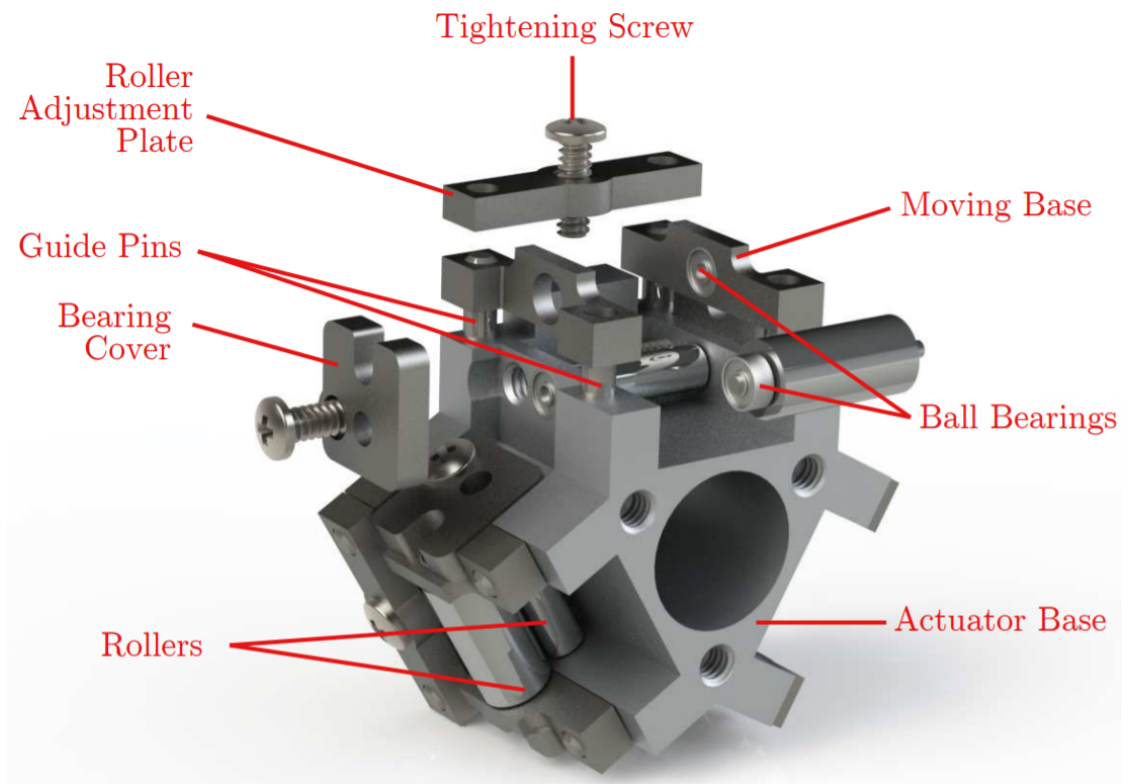


Figure 3.4. End effector of target size robot body.



Figure 3.5. Force dimension Omega 6 haptic device.

The system is controlled via field-programmable gate array (FPGA) integrated hardware NI Compact RIO (National Instruments, Inc.) on the real-time operating system (RTOS). The robot is controlled over LabVIEW (National Instruments, Inc.) by integrating Omega 6 (Force Dimension) haptic device as shown in Figure 3.5 or directly from PC over LabView control panel [10]. Further information regarding control algorithm and control parameters mapping of omega 6 on the robot workspace are given in Appendix D.

3.2. Modeling of Growing Soft Robot

Model of the growing soft continuum robot is developed to reduce positioning error. User input is given to control the position of the end effecto, which is converted to actuator space variables. To calculate actuator space variables, a kinematic model only is not sufficient for accurate positioning since the soft robot is highly prone to deformation under loading. Thus, the kinematic model has to be coupled with stiffness and quasi-static models to calculate and correct position errors caused by robot body deformation. For a colonoscopy application robot is controlled via open-loop control

and the error caused by shaft deformation is corrected by the user input with feedback received from the camera. However, due to changes in robot parameters such as body length control dynamics will significantly change that will hinder effective user control. The quasi-static model developed in this thesis estimates positioning error generated due to shaft deflection and provides input to the kinematic model for correcting actuator space variables and positioning end effector to given goal point coordinate.

3.2.1. Kinematic Model

A kinematic model is developed via the CC approach that relates task space variables to actuator space variables in a way similar to the referenced literature [75, 93, 97–99]. Based on this concept, the model is separated into two sections, as shown in Figure 3.6. For the inverse kinematics, first f_2^{-1} is mapped to compute robot body shape variables from the desired goal point coordinates, and then f_1^{-1} is mapped to calculate actuator lengths from the computed robot geometry. In Figure 3.6 actuator space variables are the actuator lengths (l_1, l_2, l_3) , configuration space variables are the rotation angle with respect to the fixed frame y axis (ϕ), curvature (κ), angle between z' and the straight line between origin and goal point (θ), and task space variables are the goal point coordinates (x, y, z) . Goal point is defined as the required EE position given with user input. One can obtain forward kinematics of the robot by reversing the mapping process, however, forward kinematics will not be discussed further in this thesis.

Configuration space variables shown in Figure 3.7 are computed according to the goal point coordinates with the geometric approach as

$$\phi = \begin{cases} l r \tan^{-1} \left(\frac{x}{z} \right) & z \geq 0 \\ \pi - \tan^{-1} \left(\frac{x}{z} \right) & z < 0, \end{cases} \quad (3.1)$$

$$\theta = \tan^{-1} \left(\frac{y \sin \phi}{x} \right). \quad (3.2)$$

Substituting Equation 3.2 into Equation 3.3, radius calculated as where $r = 1/\kappa$,

$$r = \frac{y}{\sin(\pi - 2\theta)}. \quad (3.3)$$

As the second step of kinematic modelling, configuration space is mapped to actuator space to compute backbone and actuator lengths (l_b, l_1, l_2, l_3). As shown in Figure 3.7, three pneumatic actuators are placed with equal circumferential spacing through the robot shaft, where a is the distance between the actuator centers as

$$l_b = \frac{1}{\kappa}(\pi - 2\theta), \quad (3.4)$$

$$l_1 = \left(\frac{1}{\kappa} - \sin \phi \left(\frac{a\sqrt{3}}{3} \right) \right) (\pi - 2\theta), \quad (3.5)$$

$$l_2 = \left(\frac{1}{\kappa} - \sin(\phi - 4\pi/3) \left(\frac{a\sqrt{3}}{3} \right) \right) (\pi - 2\theta), \quad (3.6)$$

$$l_3 = \left(\frac{1}{\kappa} - \sin(\phi - 2\pi/3) \left(\frac{a\sqrt{3}}{3} \right) \right) (\pi - 2\theta). \quad (3.7)$$

Although in the CC approach, kinematics is a simple application, the accuracy of the model is questioned and found to be inapplicable as is for the conditions where external loading is non-negligible [100, 114]. Thus a deformation correction is applied

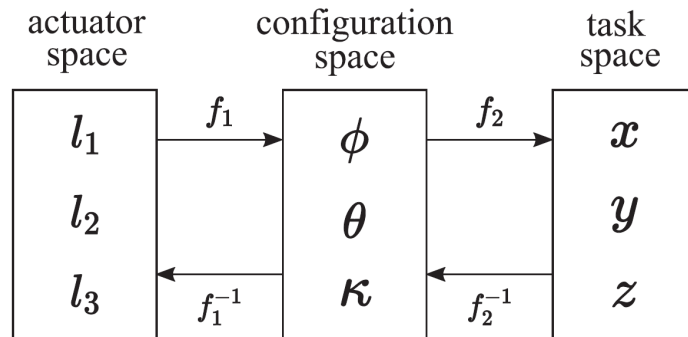


Figure 3.6. Forward and inverse kinematics functions of the soft continuum robot.

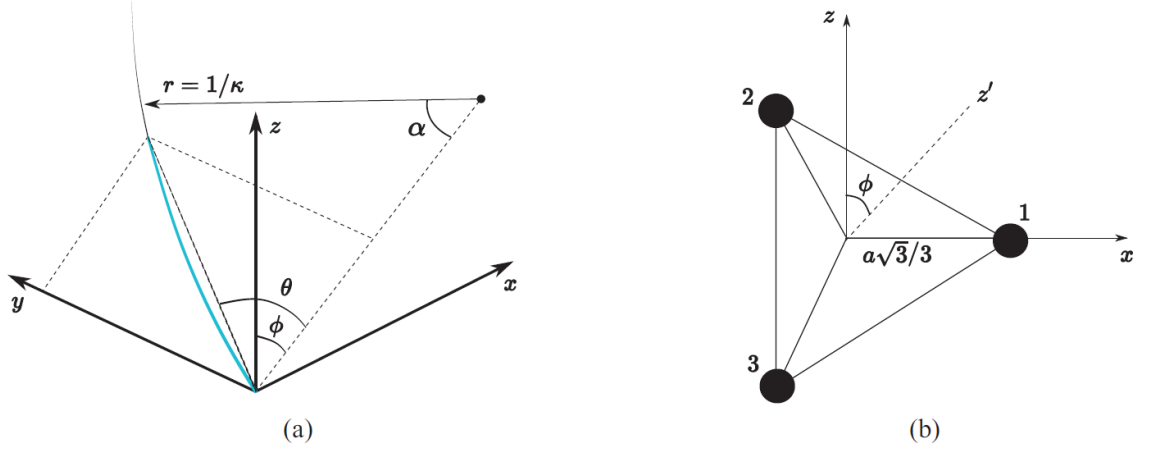


Figure 3.7. Configuration space variables and model coordinate system. (a) The solid cyan line indicates the backbone curve of the soft continuum robot. (b) Actuator positions at the robot shaft hub. Actuators are numbered from 1 to 3.

by revising goal point coordinates in an iterative process. Tip deflection and the corresponding continuum robot shaft deformation are discussed in detail under the quasi-static model section.

3.2.2. Quasi-static Model

Soft-continuum robot geometry is calculated via a kinematic model for a specific EE position in the task space. However, a kinematic model in itself is not sufficient for estimating the EE position owing to loads applied at the tip that lead to deformation of the robot shaft. To accurately control the EE position, loading on the EE is calculated using the quasi-static model. Considering the actuation type and structure of the growing soft-continuum robot addressed in this study, the quasi-static model should incorporate inflated beam bending stiffness, loading of both pneumatic actuators and tendons, internal friction, and be applicable for a growing-type shaft structure.

Loading on the soft-continuum robot should be considered to compute control variables namely, actuator lengths (l_1, l_2, l_3) , pressures $(\vec{P}_1, \vec{P}_2, \vec{P}_3)$, and tendon tensions

($\vec{T}_{01}, \vec{T}_{02}, \vec{T}_{03}$). The quasi-static model analyzes a single time point and computes shaft geometry for the given goal point coordinates. Forces and moments acting on the EE, and robot shaft are determined as a function of shaft geometry once the curvature and orientation angles ϕ , and θ are calculated via the kinematic model. The quasi-static model focuses on static equilibrium at the EE for maintaining the EE at a certain goal position, and computing EE displacement owing to robot shaft deformation caused by external loading. Shaft deformation is defined as a change in the CC shape of the flexible shaft induced by the loads applied on the EE. The friction force between the deflated tubes (tendons) and the robot shaft is also assessed in the model because the tendons slide between the inner and the outer sheath, and internal friction has a significant effect on tendon tensions.

After calculating the actuator lengths using the kinematic model, the quasi-static solution is obtained by calculating the following variables sequentially:

- bending moments ($\vec{M}_1 + \vec{M}_2 + \vec{M}_3 = \vec{M}_b$) generated owing to CC bending of inflated actuators;
- tension force vectors ($\vec{T}_1, \vec{T}_2, \vec{T}_3$) applied on the EE that balance EE forces and moments to zero in six DOFs;
- friction forces ($\vec{F}_{f1}, \vec{F}_{f2}, \vec{F}_{f3}$) between the tendons and the robot shaft as a function of tension forces;
- tendon tension forces ($\vec{T}_{01}, \vec{T}_{02}, \vec{T}_{03}$) at the robot shaft root which are greater than tension forces applied on the EE owing to friction force.

As shown on the free-body diagram (FBD) in Figure 3.8, tension forces (\vec{T}_i) balance propulsion forces (\vec{P}_i), and the bending moment (\vec{M}_b) generated due to bent inflated actuators. Together with the weight (\vec{w}) and lateral external loading (\vec{F}_{ext}), robot shaft deflects further from the CC shape.

After computing the loads on the EE, tip deflection caused by weight and external loading is calculated. As the final stage of the solution sequence, the goal point

coordinate is updated with the error vector within an iterative process. The error vector is the difference between the goal point coordinate and the EE position with the deformed shape. The objective of the solver is to minimize the error vector magnitude such that the corresponding control variables maintain the EE at the required position after deformation of the robot shaft.

3.2.2.1. Shaft stiffness. The robot shaft bent with a CC generates reaction as a pure moment (\vec{M}_b) at the EE. Bending stiffness of each actuator is calculated by modelling it as an inflated beam. Equilibrium equations presented by [115] are solved as shown in Appendix A with pure bending moment boundary conditions to obtain a relationship between tip deflection (d) and reaction moment as given in

$$M_i = \frac{2\delta \left(E + \frac{F_p}{A_0} I \right)}{l_i^2}, \quad (3.8)$$

where A_0 is the actuator section area air pressure is acting on, E is the modulus of elasticity, $I = \pi \left(\frac{d_{act}}{2} \right)^3 t$ for thinwalled tubes, d_{act} is the diameter, and t is the wall thickness of the inflated actuator.

Bending moment is the function of actuator pressure F_p/A_0 and actuator length l_i where i is the actuator number, shown as

$$\vec{F}_{lateral} = \vec{w} + \vec{F}_{ext}. \quad (3.9)$$

Deflection of the robot shaft tip owing to lateral forces is computed using the relation given in [115] as

$$\delta_{lateral} = \frac{V_i}{\left(E + \frac{F_p}{A_0} \right) I} \frac{l_i^3}{3} + \frac{V_i l_i}{F_p + kGA_0}. \quad (3.10)$$

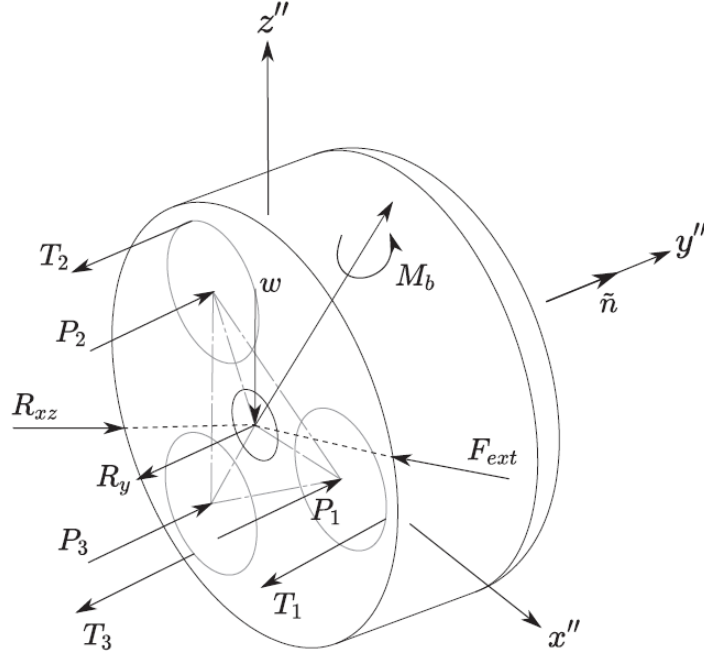


Figure 3.8. FBD of the EE. Coordinate system x'', y'', z'' is attached to the EE body.

Normal vector \tilde{n} is always collinear with the y'' direction.

Where k is the correction shear coefficient selected as 0.5 for thin-walled cylindrical beams [116]. Inflated beam stiffnesses are different owing to unequal actuator lengths because stiffness heavily depends on beam length. Therefore, $F_{lateral}$ is not shared equally by each inflated actuator for a certain tip displacement. Distribution of the lateral force and the tip displacement is computed numerically by increasing the displacement at each load step until $\vec{V}_1 + \vec{V}_2 + \vec{V}_3 = \vec{F}_{lateral}$, where \vec{V}_1, \vec{V}_2 , and \vec{V}_3 give the distribution of $\vec{F}_{lateral}$ on the three inflated actuators.

For any θ angle other than $\pi/2$, the lateral force induces torsion around the y axis that causes torsional deflection of the robot shaft. The torsional deflection is calculated via integrating deflections of finite elements over the robot shaft length from the equation

$$\gamma = \sum_{s=0}^{l_b} \|\vec{L} \times \vec{F}_{lateral}\| \cos\alpha \Delta s / GJ, \quad (3.11)$$

where \tilde{L} is the position vector between end effector and origin, $J = 2\pi t \left(\frac{d_{act}}{2}\right)^3 + (A_t r^2)$ is the polar second moment of area of the inflated actuators, such that A_t is the inflated actuator area that covers the wall thickness, and G is the modulus of rigidity.

Buckling characteristics of the soft robot are modelled with the model proposed by [115], given as

$$F^2 \frac{\Omega^2 I}{A_0} + \Omega^2 I (E + F_p/A_0) (F_p + kGA_0) - F [\Omega^2 I (E + F_p/A_0) \dots + (P + kGA_0) (1 + \Omega^2 I/A_0)] = 0. \quad (3.12)$$

The quadratic equation is solved, and the smaller root is taken to calculate the critical buckling force ($F_{crit} = F$) as shown in Equation 3.12.

Due to the nature of buckling phenomena, large and uncontrolled shaft deflection can occur that is beyond the capabilities of calculating robot control parameters with the proposed model. However, axial loading limits are computed from Equation 3.12, and Equation 3.13 for buckling to check the validity of model results given as

$$\Omega = \frac{\pi}{2l_b}. \quad (3.13)$$

3.2.2.2. Static equilibrium. As discussed earlier, the quasistatic model aims to solve for static equilibrium of both the EE and the robot shaft (See Equation 3.14, Equation 3.15, Equation 3.16, and Equation 3.17), similar to the study of [83].

\vec{d}_i is the radial distance between each actuator and the EE center, \vec{e}_i is the radial distance between the EE center and the point where tension is applied, \vec{r}_i is the position vector between point O and the point where resultant friction and normal forces applied on the robot shaft, and \vec{r}_b is the position vector between point O and shaft tip center for the robot body shown in Figure 3.9. In the figure pressurized actuators are shown in

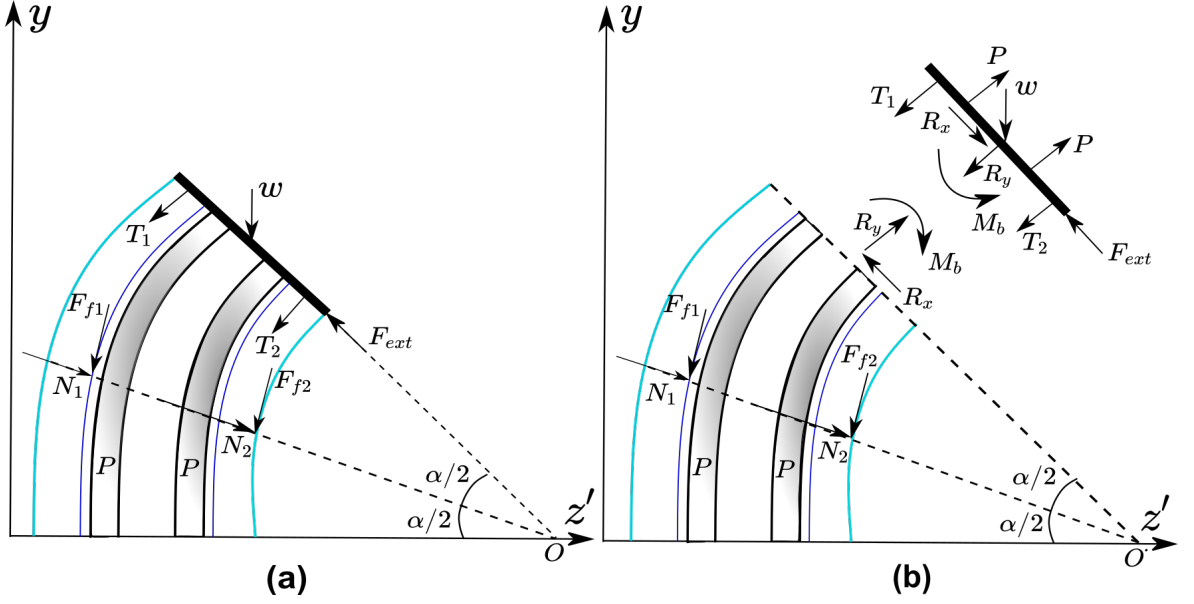


Figure 3.9. FBD of the robot in two dimensions. (a) The EE and the shaft are joined together. (b) The EE is separated from the shaft to show reaction forces.

gray, the inner sheath is shown in blue and the outer sheath in cyan. Here R_x , and R_y are reaction forces, M_b is the bending moment, and F_{fi} is the friction force between the tendon and the robot shaft where $\alpha = \pi - 2\theta$, and i is the actuator number. Equations for quasi-static solution are given as

$$\sum_{i=1}^3 \vec{P}_i + \vec{T}_i + \vec{w} + \vec{F}_{ext} + \vec{R}_y + \vec{R}_{xz} = \vec{0}, \quad (3.14)$$

$$\sum_{i=1}^3 \vec{M}_i + \vec{d}_i \times \vec{P}_i + \vec{e}_i \times \vec{T}_i = \vec{0}, \quad (3.15)$$

$$\sum_{i=1}^3 \vec{F}_{fi} + \vec{N}_i + \vec{R}_y + \vec{R}_{xz} = \vec{0}, \quad (3.16)$$

$$\sum_{i=1}^3 \vec{M}_i + \vec{r}_i \times \vec{F}_{fi} + \vec{r}_b \times \vec{R}_y + \vec{r}_b \times \vec{R}_{xz} = \vec{0}. \quad (3.17)$$

Here \vec{R}_y and \vec{R}_{xz} shown in Figure 3.8 are the reaction forces between the EE and robot shaft as depicted in the two-dimensional representation of the FBD in Figure 3.9 as vectors R_y and R_z , respectively. Forces generated by the pneumatic actuators (\vec{P}_i) are determined using the pinch roller actuator model given by [12] which are applied in the direction of \vec{n} that is computed via two consecutive coordinate transformations given as

$$\tilde{n} = \begin{bmatrix} \cos\phi & -\sin\phi\sin\alpha & \sin\phi\cos\alpha \\ 0 & \cos\alpha & -\sin\alpha \\ -\sin\phi & \sin\alpha\cos\phi & \cos\phi\cos\alpha \end{bmatrix} \begin{bmatrix} 0 \\ 1 \\ 0 \end{bmatrix}. \quad (3.18)$$

where ϕ is shown in Figure 3.7 and α is shown in both Figure 3.7 and Figure 3.9. Body-fixed coordinate system x'', y'', z'' as represented in Figure 3.8 is found by performing body fixed rotations in x , and z' with θ_2 and θ_1 degrees, respectively, where $\theta_2 = \sin^{-1}(\cos\phi\sin-\alpha)$, and $\theta_1 = \sin^{-1}(-\sin\phi\sin-\alpha/\cos\theta_2)$. Body fixed rotations are performed in x , and z' because rotation about y'' is not allowed owing to the architecture of the robot shaft and, thus, the rotation matrix is given in Equation (18) does not apply to x'', y'', z'' frame because it results in rotation about y'' . Nevertheless, \tilde{n} direction calculated in Equation (18) is taken as reference to determine θ_2 and θ_1 . Coordinates of the tendon attachment points on the EE are calculated using the transformation matrix with respect to body fixed frame.

The differential equation that describes the friction as a function of shaft length is given in which is obtained from the model given in [117]. Differential equation is derived from the equilibrium of forces as given in Appendix B shown as,

$$df_u = \mu T_i \kappa ds. \quad (3.19)$$

When the EE pulls the tendons, the tendon tension at the other end (i.e., shaft root) will be higher than the tension at the tip owing to friction along the shaft. Taking this into account, tendon tension distribution as a function of shaft length is given as

$$dT_i = -\mu T_i \kappa ds. \quad (3.20)$$

Solving the differential equation with the boundary condition $\vec{T}_i = \vec{T}_{0i}$ at $s = 0$, the relation between tension force at the EE (T_i) and shaft root (T_{0i}) is obtained from

$$T_{0i} = \frac{T_i}{e^{-\mu\kappa l_b}}. \quad (3.21)$$

Where friction force is the difference between tensions at the root and the tip ($\vec{F}_{fi} = \vec{T}_{0i} - \vec{T}_i$), and i is the tendon number associated with the actuator number.

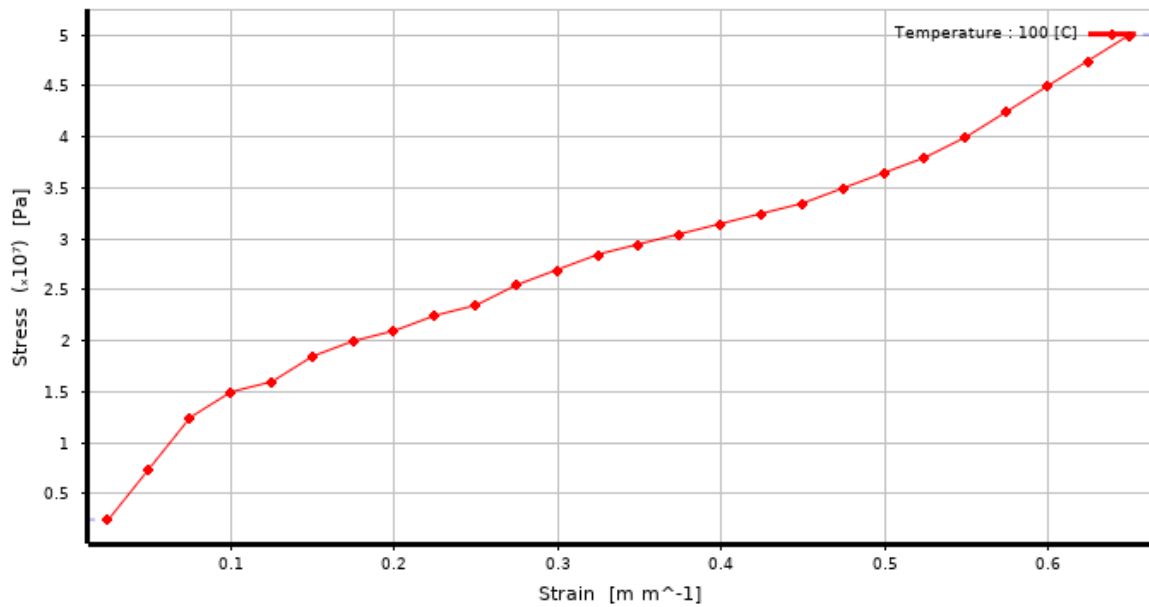


Figure 3.10. HDPE uniaxial test data [118]. Material behavior is more suitable for Yeoh hyper-elastic model due to the shape of the function.

3.2.3. Stiffness FEA Model

FEM model solved to validate the stiffness model for a single inflated actuator. The analytical stiffness model is validated for the whole robot shaft as well, where three inflated actuators placed equally on the circumference. To model the soft robot shaft Yeoh 3rd order hyper-elastic material model is used. A uniaxial test data of HDPE is used to calculate Yeoh hyper-elastic model parameters, as shown in Figure 3.10 [118]. Yeoh material model coefficients are calculated by third order polynomial curve fitting to the uniaxial tensile data.

Inflated actuators and end effector geometry that is simplified for this analysis are meshed using tetrahedral elements, as shown in Figure 3.11. Pressure applied inside the tubes, loading applied on the tip in x-direction, and tubes are fixed from the root at all DOF.

The analytical deflection Equation 3.8, and Equation 3.10 are generated from non-linear equilibrium equations by linearizing about the reference configuration, which is the pre-stressed state that is assuming small magnitudes of displacements and rotation. A non-linear structural FEM analysis performed with a large deflection setting is on. Deflections calculated with non-linear FEM analysis are compared to the linearized analytical solution, which shows the level of accuracy of using linearized stiffness equations in the analytical model.

3.3. Prototypes

Prototypes developed in this study are tested as a proof of concept for the proposed robotic system. Through the development process, the first prototypes had simple features for proving the actuation concept, and the complexity of the design is increased by adding more features to meet application requirements. A 1D prototype is manufactured that is used to prove pinch roller drive concept and test various actuator tubings. As the second step, two 2D prototypes are developed to control the

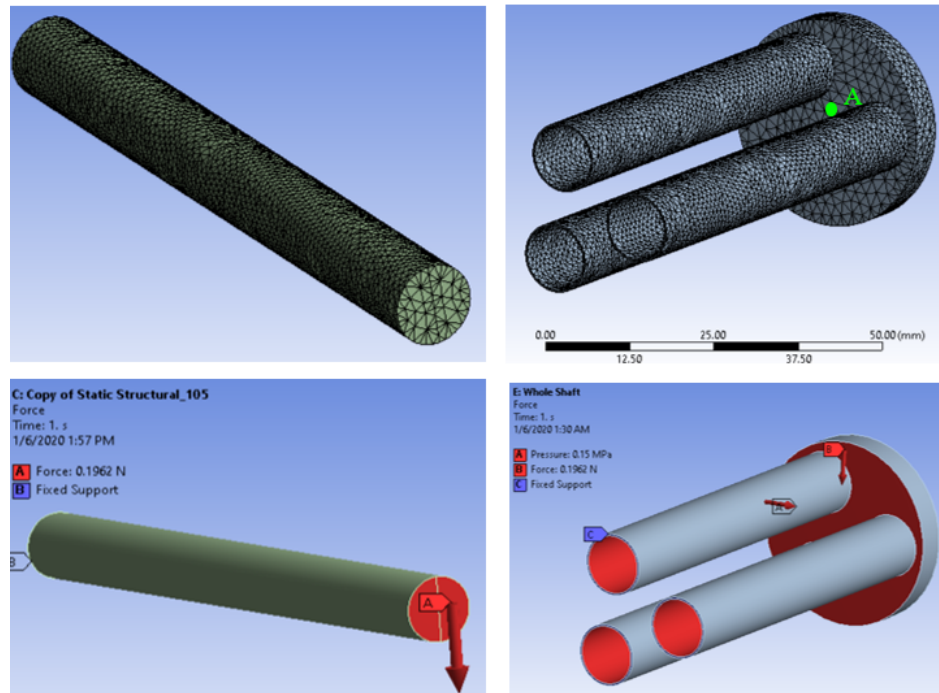


Figure 3.11. Single tubing and robot shaft FEA models, mesh and BCs.

system for performing basic maneuvers. After improving the actuation and control systems on the 2D prototype, 3D prototypes are developed for validation tests that aim to prove the concept for potential colonoscopy application.

3.3.1. Actuation Mechanism and Robot Body

The 1D prototype is shown in Figure 3.12 is developed to prove the concept of pinch roller drive mechanism. The pinch roller drive mechanism is connected to a car located on the linear guide. Actuator tubing is clamped between two rollers and inflated by the air compressor. The mechanism is propelled with the inflated tubing, and the force generated by the actuation system is measured. The prototype is used to measure the force generated by actuator tubings of various material and dimensions and identify design improvements for the actuator mechanism. Although the prototype proved the pinch roller drive concept, significant problems are identified on the mechanism that is addressed and improved on later prototypes. One of the

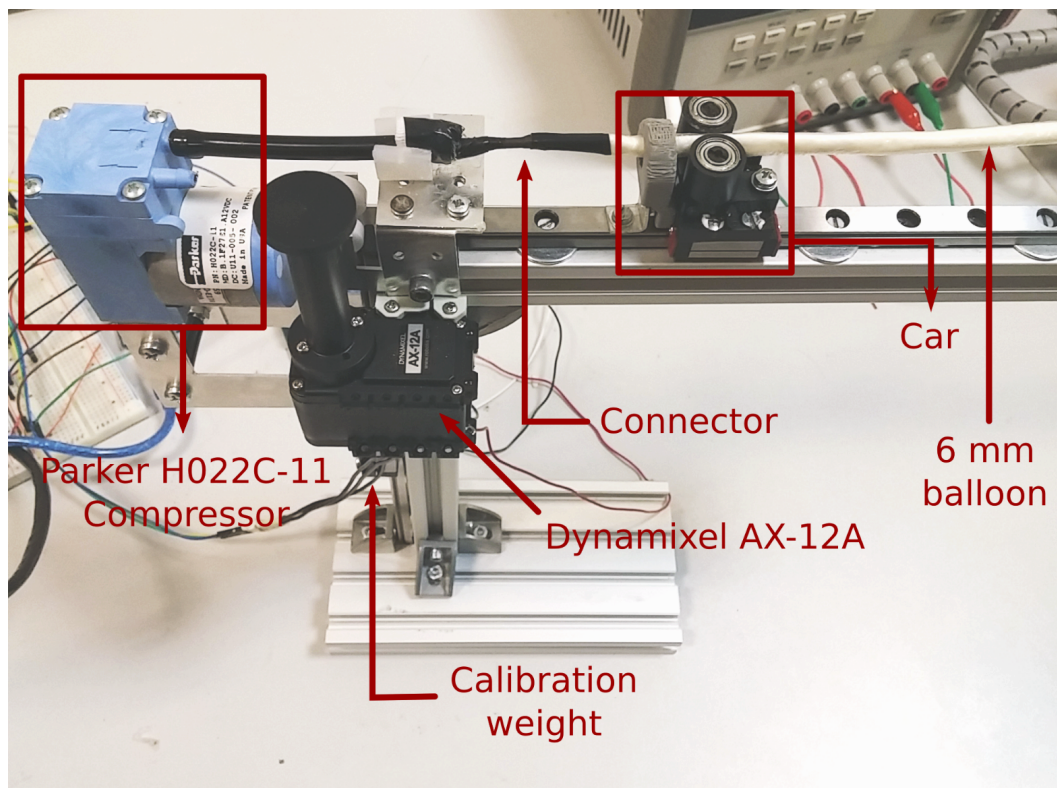


Figure 3.12. Single DOF prototype. Pinch roller drive mechanism is attached on a linear guide. The actuator tube is connected to pressure compressor. The test setup is used to prove pinch roller drive concept and test various actuator tubings.

major problems was the weak air seal between inflated and deflated sections of the actuator tubing. The leakage causes loss in actuation force and locks the mechanism at higher leakage rates since the tubing section that is supposed to be deflated is inflated. The reason for the leakage is due to micro gaps occur the edge of contact of rollers. The first prototype is manufactured from Polyamide that has low stiffness and poor manufacturing tolerances. An improved version of the first prototype is manufactured from steel that provided better sealing capability due to tighter parallelism tolerance of rollers and higher stiffness.

The concept is proved on planar space with a 2D prototype. This prototype has two pinch roller drive mechanisms attached to the body ,as shown in Figure 3.13 and driven by two inflated actuators. Rollers in the middle of the chassis can slide over the

linear guides that are located horizontally. The adjustment screw between the sliding rollers clamps the roller couples to maintain sealing on the actuator tube [119].

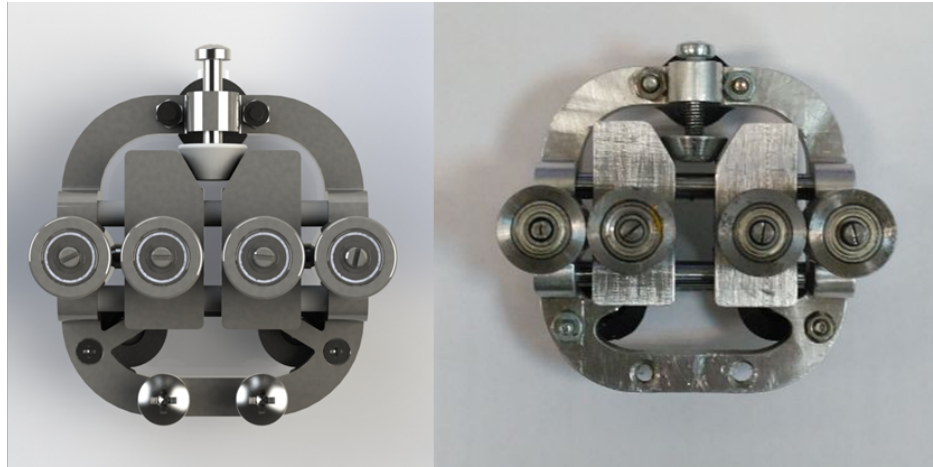


Figure 3.13. 2D Prototype. CAD model on the left and manufactured assembly on the right. The assembly body is actuated by two pinch roller drive mechanisms that allow prototype to perform translation and rotation.

The 2D prototype is shown in Figure 3.13 aims to prove the concept by demonstrating basic maneuvers on planar space. The difference between inflated actuator lengths controls the motion of the mechanism. Linear motion is achieved by feeding both inflated actuators at the same rate. Rotation and lean maneuvers are performed by setting different lengths to the inflated actuators. Basic maneuvers such as linear motion, rotation, and lean are depicted in Figure 3.14 with a 2D sketch of the target configuration.

Significant problems experienced with the 2D prototype are the dislocation of inflated actuator by moving upwards, and buckling of the inflated actuators for longer robot bodies. Although leakage performance of the pinch roller drive mechanism is improved compared to 1D prototype failure related to leakage still observed on the 2D prototype.

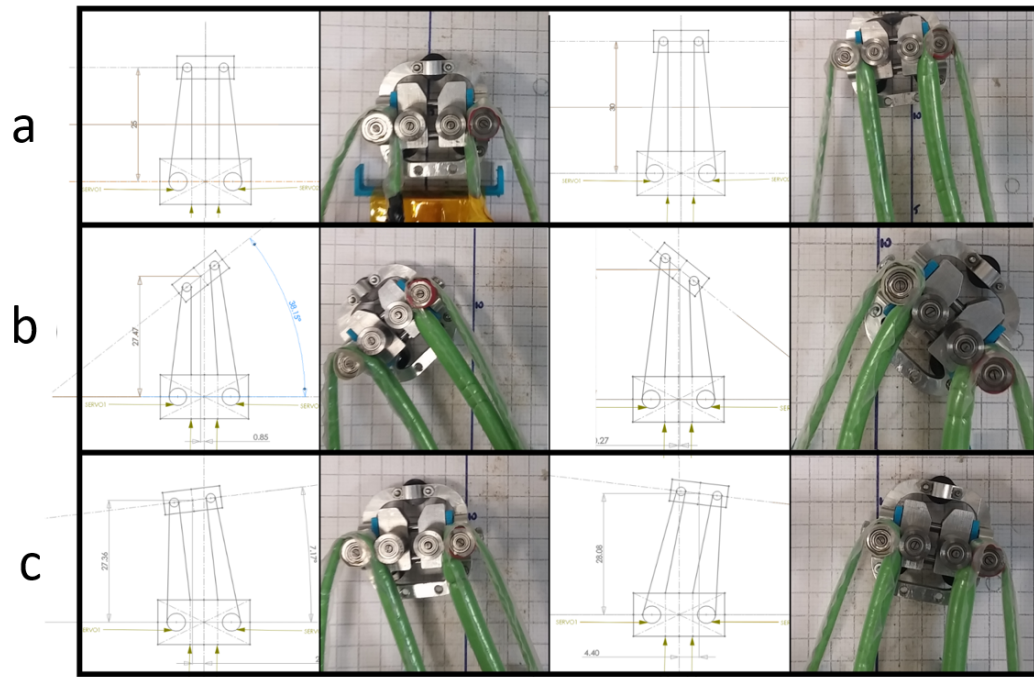


Figure 3.14. Basic maneuvers of 2D prototype.

An improved version of the 2D prototype is developed and manufactured via 3D prototyping, as shown in Figure 3.15 [119]. The improved 2D prototype is manufactured via 3D prototyping. The robot has two PRD mechanisms that are clamping the inflated tubings using the tightening screws located at each side of the end effector. The slack section of the tubing is connected to the stepper motor. Inflated tubing is restrained in vertical direction by the fixed and moving base parts that solves the problem of dislocation as experienced in the previous 2D prototype version. For the improved version, clamping of separate PRD mechanisms is adjusted by separate tightening screws different than the previous 2D prototype version that provided better air seal characteristics for the improved prototype. The improved prototype is utilized to perform navigation, actuation speed, and actuator force generation tests.

After addressing the major design problems experienced with 2D prototype tests, 3D prototypes are developed to meet application requirements. As the first step, 3D prototypes with a large dimensional scale are developed. Those large scale prototypes

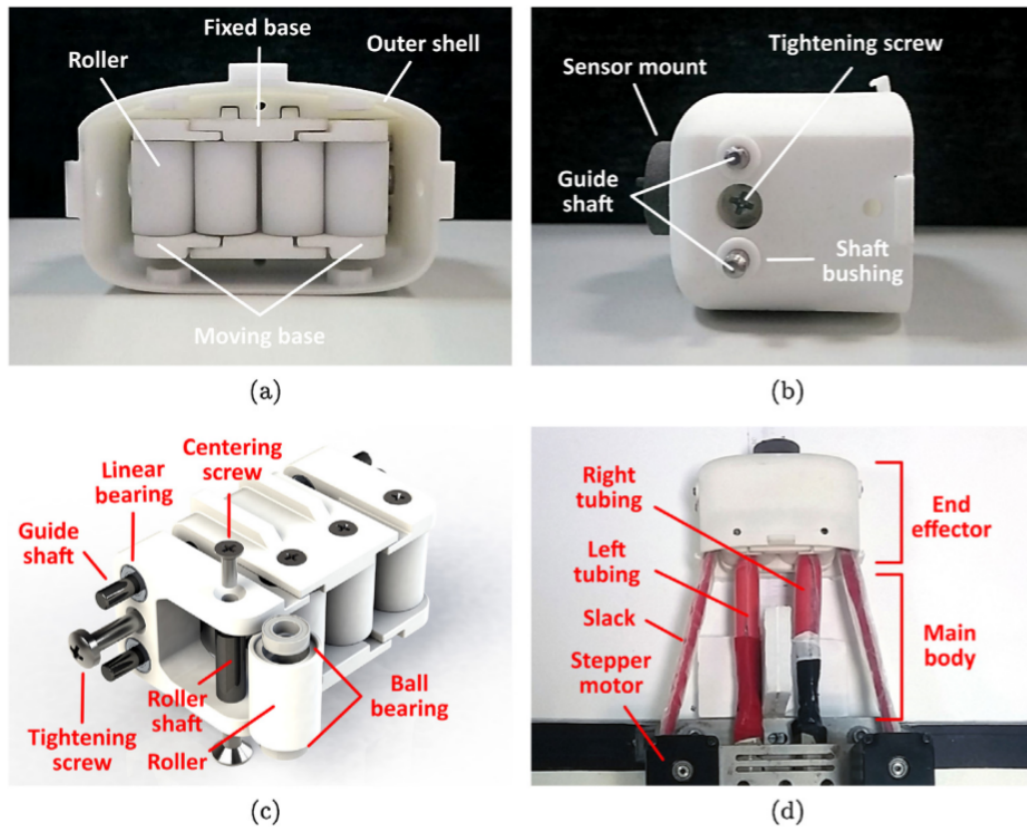


Figure 3.15. Improved version of 2D prototype. (a) Aft looking forward view (b) Side view (c) Solid model of exploded view (d) Top view of the prototype assembled to in-vitro section [119].

have the same features as the final scale design, however larger by size compared to target dimensions [119] [120]. The purpose of developing and manufacturing large scale prototypes first is to ease the identification and resolution of conceptual design problems. Another reason to prioritize large scale prototype development is due to the availability of actuator tubing for the larger size. A small scale 3D prototype with target dimensions is also developed and manufactured as the final step of prototype development. Two versions of large scale 3D prototypes are developed that have different dimensions named PV1 and PV2 for brevity, as shown in Table 3.1.

The first version of the 3D large scale prototype (PV1) has similar features as the 2D prototype [120]. The end effector is manufactured via 3D prototyping from

Table 3.1. Large scale 3D prototype dimensions.

Prototype	Robot body dimensions
PV1	OD: 50mm, L: 310mm
PV2	OD: 40mm, L: 1000mm

PA 12 material, as shown in Figure 3.16. The inflated actuator is clamped between the rollers, and clamp force is applied by the three tightening screws located on the roller adjustment plate and two tightening screws located on the moving base. The main features of the 3D end effector are shown in Figure 3.4. For this prototype, roller diameters of the pinch roller drive mechanism are selected as unequal to reduce the total radius of the end effector.

Deflated tubings are connected to the pulleys on feed unit driven by the servo motors, and the robot body is fixed at the base plate. The air control unit shown in Figure 3.17 has the valves, and pressure sensors to control the pressure of the inflated tubings. Detailed description for components of PV1 is also given in Figure 3.2. A system flowchart of the robot control and feed units are given in Figure 3.18. Both air control unit and feed unit are controlled by the National Instruments CompactRIO real-time controller. The air control unit is composed of air compressor, pressure vessel, valves, and pressure sensors. Pressurized air is stored in the pressure vessel, and the air compressor is automatically operated to keep the pressure at a certain level.

Inlet valves are connected to pressure vessel and controlled by the transistors via an electrical signal received from real-time controller. To move the end effector forward, inlet valves are opened, and actuator tubings are pressurized to a constant value adjusted by the pressure regulator located at the exit of the pressure vessel. The inflation pressure is measured by the pressure sensors and shown on the user interface as feedback. When it is required to retrieve the end effector back, exhaust valves are activated, and pressurized air inside the inflated actuators is evacuated. Feed unit is composed of a motor driver and stepper motors that drive the spools to release or

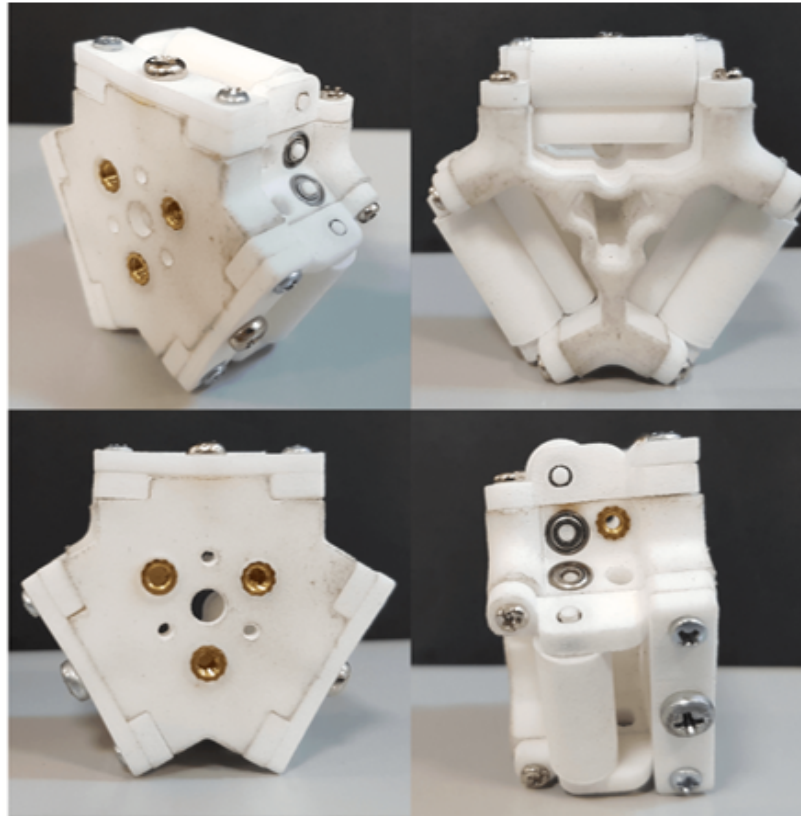


Figure 3.16. End effector of first 3D large scale prototype (PV1). Components are manufactured via 3D manufacturing from PA 12 material [119].

retrieve deflated tubings. The real-time controller sends control signal to the driver board to adjust each stepper motor's speed per planned end effector route. Stepper motors release the deflated tubing with the calculated rate to achieve the desired robot body shape at the end of the motion. Main control algorithm for 'idle', 'move forward', 'move backward', and 'stop' system states is given in Appendix D [120].

During the 2D prototype tests buckling of inflated actuators for longer robot shaft is identified as one of the significant problems. To increase the critical buckling force limit of the robot body, an outer sheath made of meshed polyester is added to the design, as shown in Figure 3.17. The meshed polyester cover has a variable diameter per extension length. This prototype is used for navigation and tip position control tests, and force and speed measurement experiments.

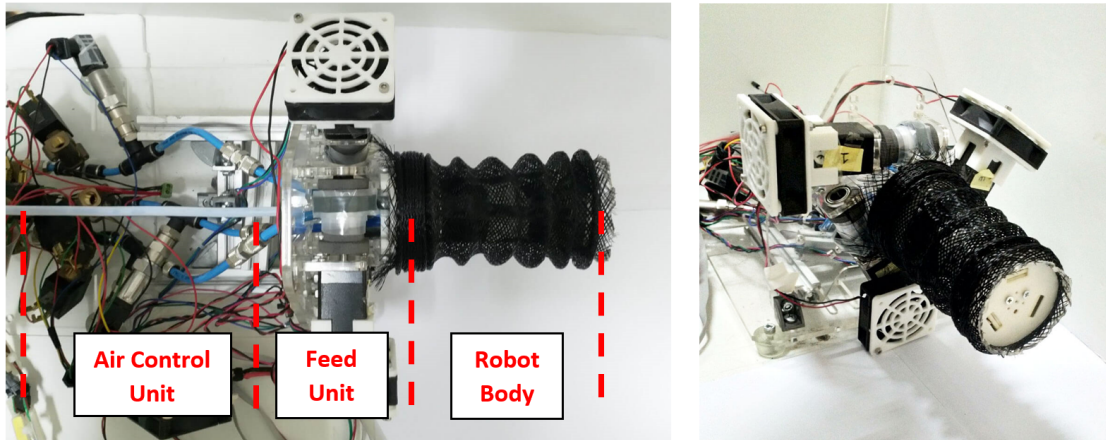


Figure 3.17. Assembly of the PV1. Robot is composed of three modules as air control unit, feed unit, and robot body.

The second version of a large scale 3D prototype is developed named PV2. For this prototype, radial layout is re-optimized to reduce the diameter of the end effector. As the result end effector diameter is reduced from 50 mm to 40 mm. Secondly, features added to the end effector to improve the alignment of inflated tubing with the roller clamping edge. The manufactured PV2 end effector is shown in Figure 3.19

The robot body of PV2 is composed of actuator tubings, inner and outer sheath, and LED camera chord. The body diameter is 40mm in nominal and can be reduced to 24 mm when compressed from outside. Unlike PV1, a constant diameter PE thin film tube is used for outer and inner sheath on PV2. With the new iteration (PV2) robot, body length is extended from 310 mm to 1000 mm, which is closer to the application requirements. Longer robot shaft on PV2 allows the concept to be tested in longer paths similar to the human colon. Thus, PV2 is used to prove the system's concept and controllability in longer maze and measure the reaction force applied by the robot on the maze wall.

A small scale prototype that has a robot body diameter of 16 mm is developed and manufactured that meets the requirements of colonoscopy application. The end effector static base is manufactured via CNC machining from AISI 302 steel. Moving

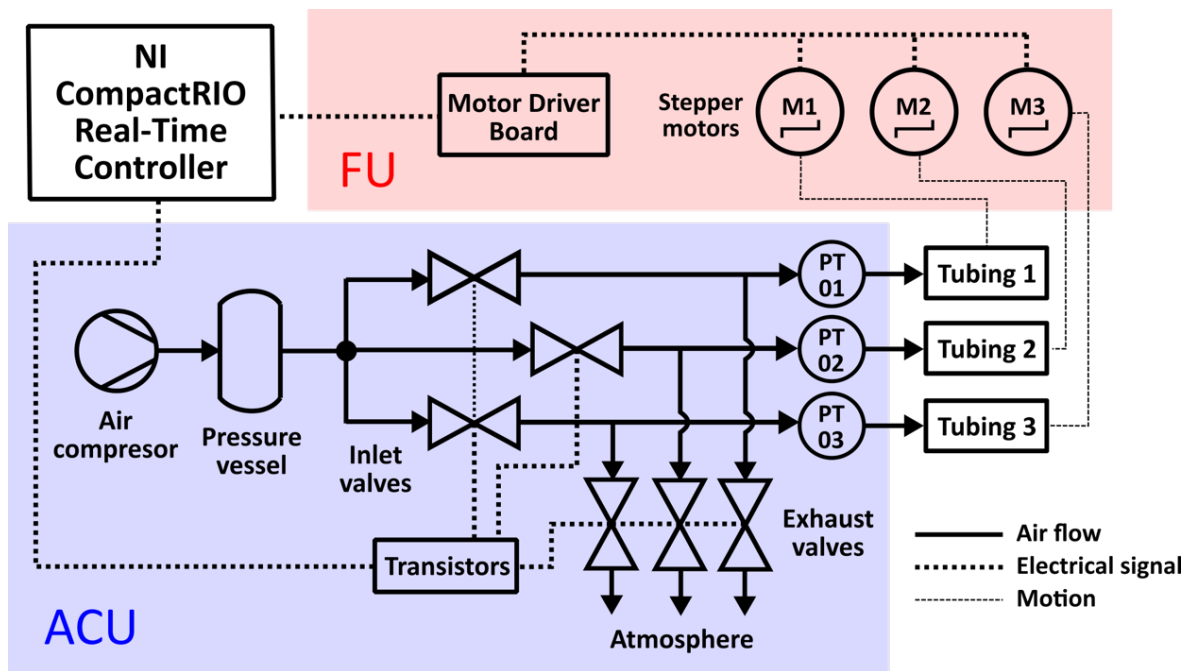


Figure 3.18. Schematic of air control unit, and feed unit [120].

base, roller adjustment plate, and bearing covers are manufactured from sheet metal by laser cutting. Rollers are connected to static base, and moving base via ball bearings that have 1 mm outer diameter, and 0.5 mm inner diameter. The manufactured small scale end effector is shown in Figure 3.21, and feature naming is given in Figure 3.4. Technical drawings of the small scale end effector are given in Appendix E.

The functionality of the small scale 3D prototype is tested and observed limited motion capability. Tubings used in this prototype are double layer extruded tubes, and the stiffness is highly dependent on the extrusion thickness. Since tubings are clamped and bent over the rollers, they should be soft enough to sustain smooth motion. Due to the limitations on manufacturing capabilities, tubing stiffness that is compliant to the small scale prototype cannot be achieved; thus, validation testing cannot be completed on this prototype. Detailed information regarding the tubing selection and design is given in the following section.

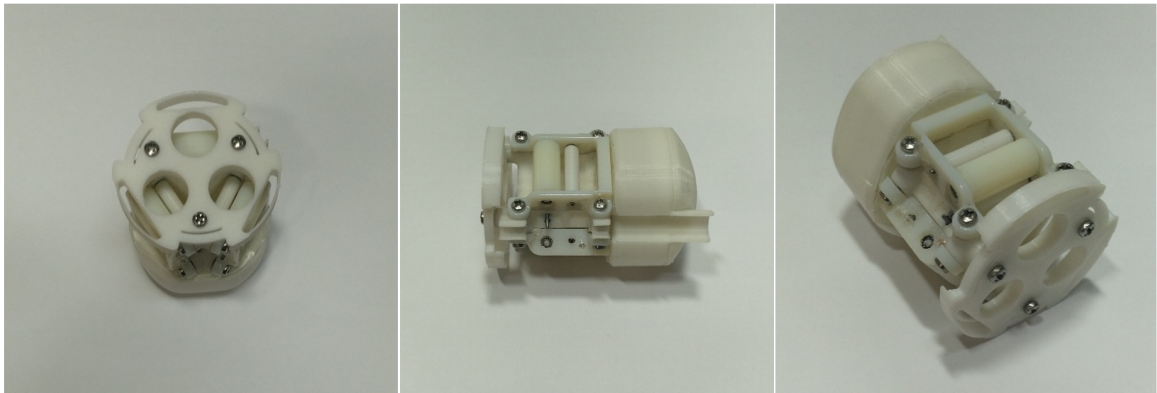


Figure 3.19. End effector of PV2. Layout of the features in radial direction is optimized to reduce total diameter of the end effector. Alignment between inflated tubing center and roller clamp edge is improved by implementing additional features.

3.3.2. Actuator Tubings

The actuator tubings are used to generate propulsion force for the PRD. As the requirement of PRD mechanism application, soft and flexible tubes should be inflated and routed back over the rollers. Medical balloons manufactured by Simeks

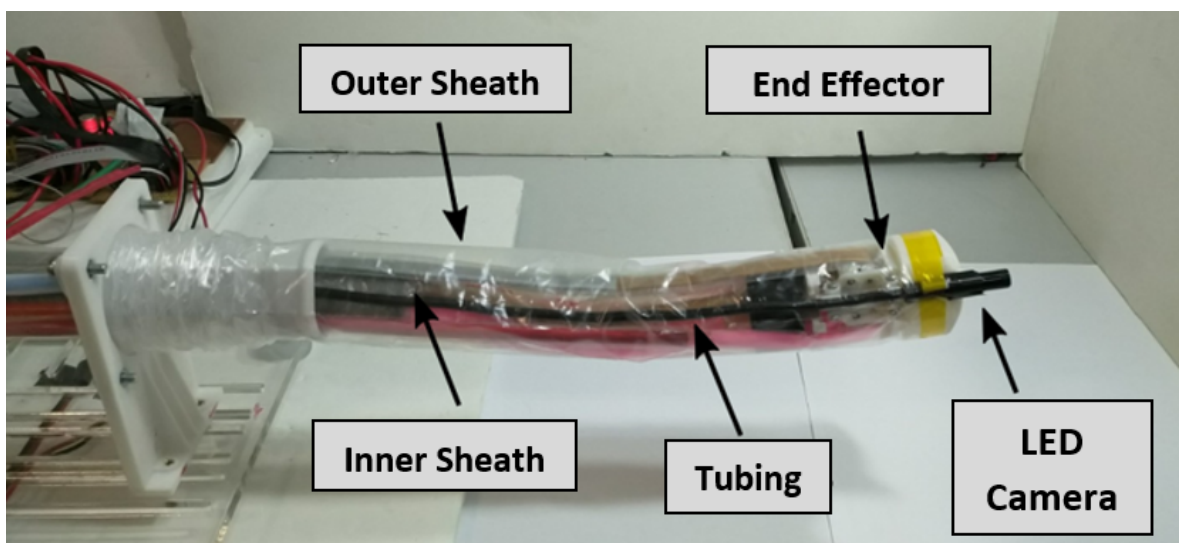


Figure 3.20. Prototype (PV2) features.

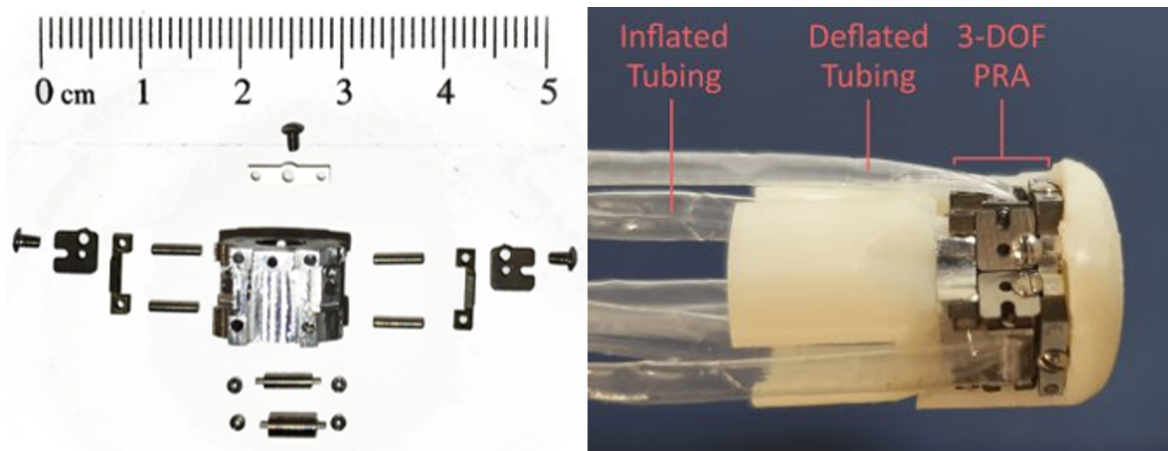


Figure 3.21. . Components of the end effector shown on left and small scale end effector assembly is shown on right.

medical company are considered as the solution that meets the requirements of the actuators. Those balloons are manufactured from PA 12 by blow molding with high burst pressure capability as 20 bars. The PA 12 medical balloons have 0.025 mm wall thickness and can be manufactured within 3 to 10 mm outer diameter range that meets the dimensional requirement of developed prototypes. However, due to the limitations on manufacturing capabilities, the longest balloon that can be manufactured is 250 mm that does not meet the requirements of colonoscopy application of 1800 mm. To address the length limitation, multiple balloons are connected from the tips via various methods such as (1) laser welding of conical features at the tip of the balloons (2) ultrasonic welding of conical features (3) optimizing conical feature dimensions and welding laser method. In Figure 3.22 medical balloons welded using method three is shown. The experiments performed on the extended PA 12 balloons showed that PRD mechanism is failing to pass through the weld edge smoothly due to thicker wall thickness at the weld edge. As the result none of the welding methods were found to be suitable. A second major problem identified for the PA12 balloons regarding lack of air-seal capability between PRD rollers. Although thin balloon wall thickness provides required flexibility, it cannot fill the micro gaps that occur at the roller edge of contact as it is clamped. Thus, tests with PA12 balloons showed poor air seal characteristics.

To achieve longer shaft length off the shelf, medical tubing options are considered that have up to 2 m length. The disadvantage of medical tubings is they have thicker wall; thus, have higher stiffness compared to medical balloons. In this case, modulus of elasticity of the tubing, material has to be selected to have required flexibility. Off the shelf tubings that have the potential to be used in prototypes and have a length above 1000 mm are listed in Table 3.2. The tubings shown in the table are procured from medical tubing manufacturers Vention medical and Zeus tubing.



Figure 3.22. Medical PA12 balloon welded using method 3 as explained above. On the connection area conical features can be observed. As also seen in the figure melted material accumulated and generating additional thickness at the weld edge.

Table 3.2. Tested off-the-shelf medical tubings. Only tubings that showed potential to be used in prototypes, and have length above 1000mm are listed in this table.

ID	Material	OD(mm)	t(mm)	L(mm)	Hardness
Vention 148-0089	Pebax	3.099	0.127	1397	72D
Vention 148-0063	Pebax	3.099	0.127	1397	55D
Vention 148-0104	Pebax	5.613	0.127	1397	72D
Vention 148-0130	Pebax	5.613	0.127	1397	55D
Zeus StrmLiner VT	PTFE	3.048	0.025	1802	60D
Zeus PTFE Liner	PTFE	5.613	0.127	1802	60D
Zeus Pebax Jacket	Pebax	5.613	0.127	1802	55D

The tubing tests performed on the 1D prototype depicted in Figure 3.12 showed that Vention medical tubings, Zeus PTFE Liner, and Zeus Pebax Jacket are not flexible enough to bend over the rollers to maintain continuous motion. Among those tubings, only Zeus StreamLiner VT showed expected flexibility similar to PA12 medical balloons could be explained by the thin wall thickness, which is 0.025 mm. Although Zeus StreamLiner VT is meeting the flexibility requirement, the burst pressure is low, and thus, fails under operating pressures even if a small scratch occurs on the tubing surface through the motion. As the result none of the off the shelf medical tubings are found to be suitable for the application. To continue prototype testing actuator tubings are fabricated in Boğaziçi University Haptics and Robotics Laboratory considering the application requirements. As observed during the actuation mechanism tests, micro gaps formed at the roller edge of contact due to manufacturing tolerances affecting parallelism of roller centerlines. Those micro gaps caused weak air seal between inflated and deflated sections that prevented the locomotion of the actuation mechanism. To address the leakage problem, actuator tubings are made as double-layer tubes with a soft LATEX layer inside and LDPE as the outer layer. The soft inner layer is used, which fills the micro gaps at the edge of contact and facilitates the air seal between inflated and deflated sections. Although the soft inner layer is improving the sealing capability, it is prone to unstable expansion in the radial direction and has low burst strength against pressure so, LDPE outer layer utilized as a radial constraint to prevent burst and radial expansion. In technical perspective, double layer tubing has proved to be operating per expectations however, it is challenging to obtain such tailored part off the shelf.

The tubings are fabricated in the laboratory with a limitation on outer diameter (OD) as a minimum 10 mm. This actuator tubing is used on both 2D and 3D large scale prototypes. The first samples of the fabricated tubing were limited to 250 mm length. In the experimental work performed using a 2D prototype and PV1 250 mm length actuators are used; thus, the concept is proved for a short robot body. With further development in custom tubing manufacturing, a method is applied to connect multiple LATEX tubes and obtain a longer tube. LATEX tubes are connected by combining

each tube from their tips using liquid LATEX as the adhesive. The liquid latex applied to the connection area is deployed to be as thin as possible to prevent excessive material accumulation similar to the problem occurred by welding, as shown in Figure 3.22. However, the adhesive liquid LATEX layer should also be thick enough to provide the required burst pressure limit. Due to the challenges of standardizing fabrication, 50% of manufactured tubings either had low burst pressure or thick connection areas that failed the robot's smooth motion. Long tubings that met the required standard are used on PV2 successfully on navigation and wall reaction tests. Comparison of fabricated tubings and off the shelf tubings are given in Appendix C.

A custom co-extruded tubing is developed with Zeus to be used in a small scale 3D prototype. This tubing has a double layer with soft Pebax as the inner layer and Nylon 12 on the outer layer. Similar to the fabricated LATEX-LDPE double layer tubing, softer Pebax maintains the air seal and Nylon 12 generates a radial constraint to prevent radial expansion. Dimensions of the co-extruded tubing are outer diameter 3.048 ± 0.127 mm, outer layer (Nylon 12) thickness is 0.0381 mm nominal and 0.0127 mm minimum, inner layer (Pebax) thickness is 0.0635 mm nominal, and 0.0381 mm minimum. The co-extruded tubing is tested showed that the tubing is stiffer than expected; thus, cannot maintain smooth motion of the small scale end effector. The root cause of the problem is identified as the Nylon 12 layer is not thin enough to provide the required flexibility.

3.4. Validation Testing

The RPD mechanism is one of the critical features for the concept of the robot presented in this thesis. The 1D prototype validates PRD mechanism, and possible design improvements are identified. The 1D test setup is also used to test actuator tubings. The PRD mechanism's performance is quantified by measuring the force generated by the actuator, and observing the motion. The 1D test setup is shown in Figure 3.23. Measured actuation force for various tubings is given in Appendix C, and more detailed results are provided in [119].

Force generation measurement is also performed on a 2D prototype using the test setup shown in Figure 3.24 [12]. The force is measured from the load cell located at the tip of the end effector. The generated force is measured for various end effector rotation angles between -30° and 30° . The test setup is also used to measure the speed of the end effector by measuring the time difference of push switch activation located at the hub and barrier. The 2D prototype as described in Figure 3.15 and Figure 3.24 is also subjected to navigation tests. The navigation testing is performed on various maze types such as navigation through an open cavity, and closed path maze, as shown in Figure 4.12, and Figure 4.13 [119].

The large scale 3D prototype (PV1) is also used for the validation tests such as bending, force generation tests, and end effector speed tests [10]. The schematic for test setups for the aforementioned validations mentioned above is shown in Figure 3.25, and the results are given in [119]. PV1 is used on 3D navigation tests with a comprehensive test procedure in terms of the coverage of maneuver types and variety of maze structures. A 3D closed maze navigation test was performed on PV1 which is

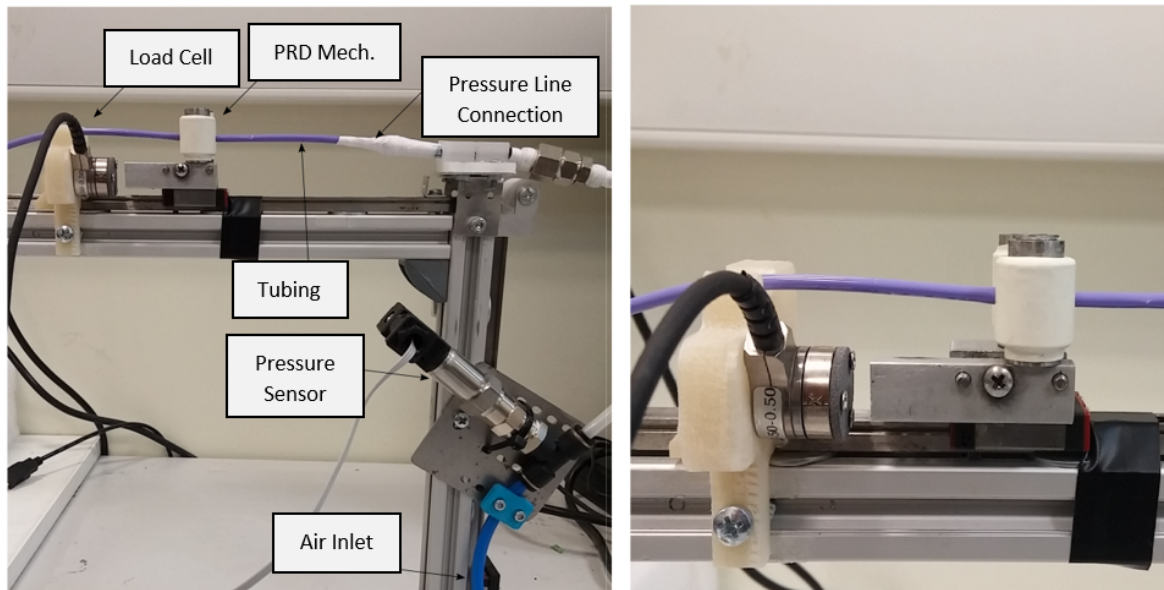


Figure 3.23. 1D test setup. Generated force is measured via ATI Nano-17E load cell, and inflation pressure is measured via pressure sensor.

considered one of the significant navigation tests due to its similarity to human colon. Results of the PV1 navigation tests are shown in Figure 4.15.

Due to the unavailability of tubing for small scale 3D prototype, testing on 3D could only be performed on PV1 and PV2. Those prototypes are used to prove the concept of novel growing type mechanism and validate the controllability of the system in 3D. For achieving similarity between robot and working environment, test setups are also geometrically scaled-up to comply with the ratio between the human colon and conventional colonoscope diameters. Diameter ratios of maze and robot body are compared with the diameter ratios of the sigmoid colon and colonoscope insertion tube to show the dimensional similarity between colonoscopy and test setup. For calculating the ratio for human colon and colonoscope diameters, sigmoid colon diameter is considered since it has the smallest diameter among all colon segments, and a large size commercially available conventional colonoscope is selected. As shown in Table 3.3, the ratio of maze ID to robot body OD is smaller than the ratio of the Sigmoid colon

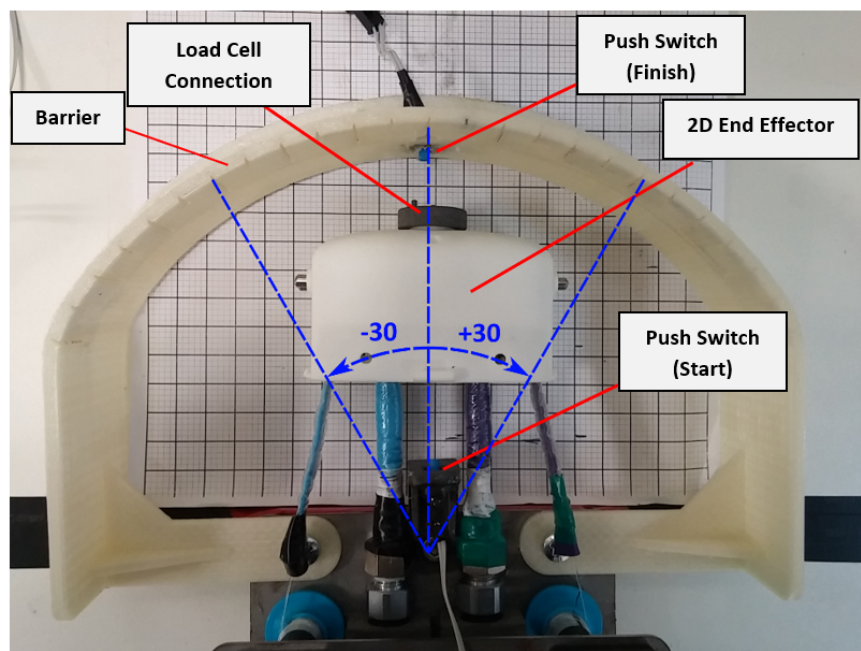


Figure 3.24. 2D test setup. The test setup is used to measure generated force by the 2D end effector and speed of the system for a 60° span [119].

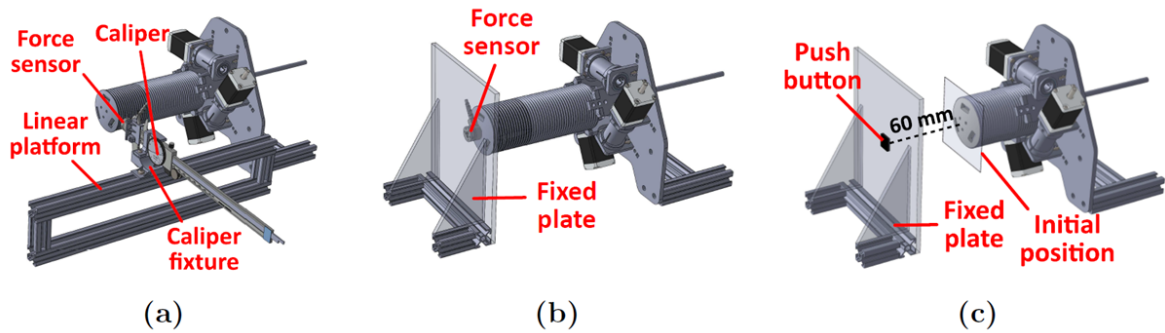


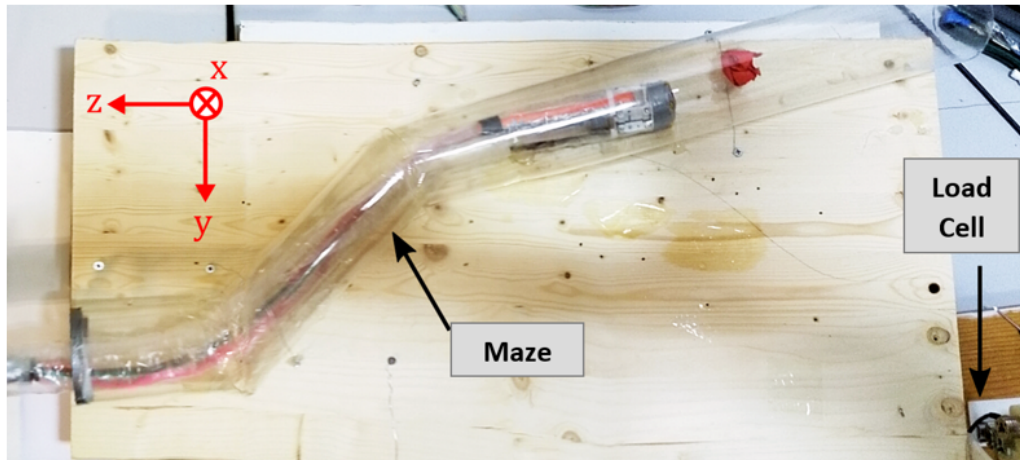
Figure 3.25. Schematic for validation tests performed with PV1. (a) Bending test, (b) force generation test, (c) speed test [119].

ID to conventional colonoscope OD showing that robot is operating in a more narrow cavity compared to conventional colonoscope operating in the colon. Thus, prototype validation is performed on more conservative condition in terms of size which majorly affects the friction and reaction forces between maze and robot body.

Table 3.3. Prototype size comparison.

Prototype	Robot body dimensions	$\frac{d_{ID,MAZE}}{d_{OD,ROBOT}}$	$\frac{d_{ID,COLON}}{d_{OD,COLONOSCOPE}}$
PV1	OD: 50mm, L: 310mm	1.4	2.51
PV2	OD: 40mm, L: 1000mm	1.75	2.51

The reaction force between the robot body and maze wall is measured on the test setup shown in Figure 3.26. The maze is attached to a platform that is allowed to slide in y , and z directions via marble spheres placed under the platform. A load cell (ATI Nano 17 force/torque sensor) capable of measuring forces and moments in 6 degrees of freedom is attached to the platform's right edge. As the robot progressed through the maze reaction forces in three directions is measured, and the resultant reaction force is calculated.



(a)



(b)

Figure 3.26. Test setup for wall reaction measurement. (a) Top view of the test setup. Measurement coordinate system is depicted on up right corner. (b) Side view shows the marble spheres under the platform that allows frictionless planar motion.

4. RESULTS

In this section, simulation results of the kinematic and quasi-static model are presented, analytic stiffness models are compared with FEM results, and experimental measurements are assessed with model estimations. In addition to model validation, navigation experiment results, and wall reaction measurements are presented and further discussed in Chapter 5 by comparing the results with conventional colonoscopy and other robotic colonoscopy systems given in the literature.

4.1. Kinematic Model

The kinematic model is demonstrated for four different goal points by computing the robot shaft shape using Equations 3.1-3.7, as shown in Figure 4.1. Inflated tube curves are colored black, red, and green for actuator numbers 1, 2, and 3, respectively. Backbone curve is colored blue and the triangles at proximal and distal ends of the robot body represent the triangle shown in Figure 3.7. The configuration space variables are also shown where ϕ is between 0 and $\pi/2$ for positive z values and between $\pi/2$ and π for negative z values as defined in Figure 3.7. θ value is calculated as $\pi/4$ for the goal point (180, 180, 0) from Equation 3.2 since $\phi = \pi/2$. Lengths of the actuators and the backbone are plotted for each goal point in Figure 4.2a. Bending moments, tendon tension forces at the root of the robot shaft, and friction forces are also plotted for each goal point. The bars shown in Figure 4.2a are color coded using the same convention followed in Figure 6: black, red, and green for actuator numbers 1, 2, and 3, respectively, and blue for the backbone. Actuator numbering and circumferential positions are defined in Figure 3.7. The calculation is performed by setting parameters as Here $P_{gage} = 0.1MPa, E = 1.5GPa, v = 0.3, d_{act} = 16mm, t = 0.088mm, a = 26mm, m_{roller} = 0.2, \mu_{tendon} = 0.1$.

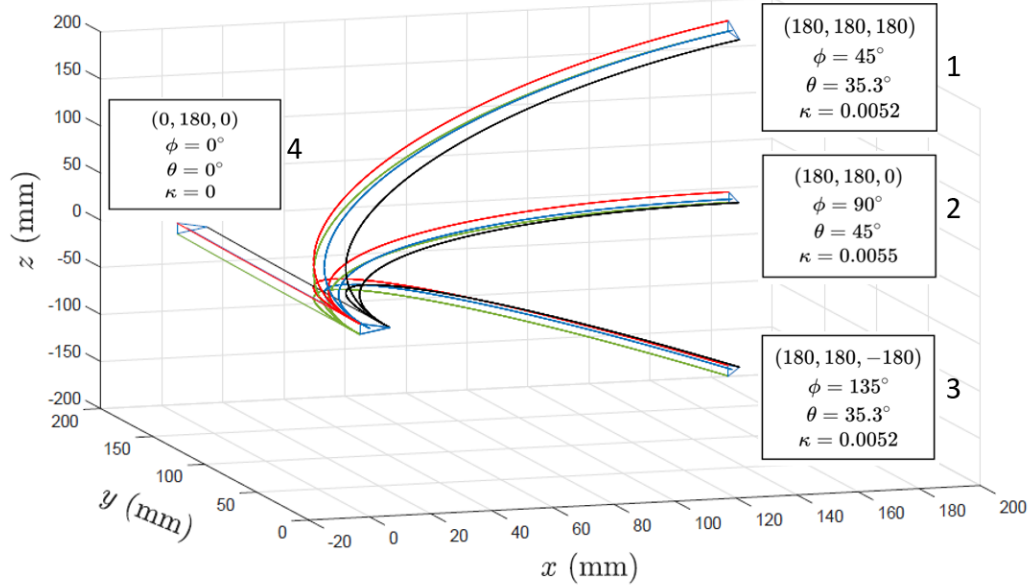


Figure 4.1. Shape of the soft continuum robot for four different goal points numbered as shown (length in millimeters). Curvature κ is given in mm^{-1} .

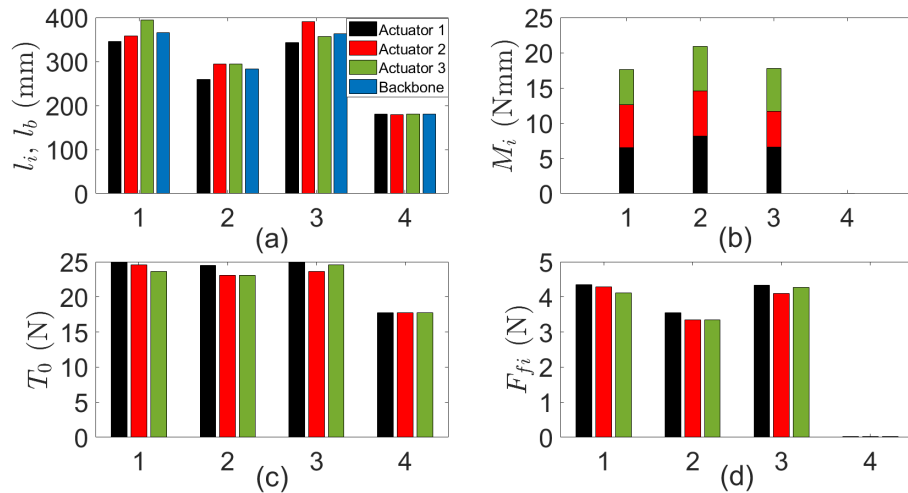


Figure 4.2. Model parameters for the four goal points given in Figure 4.1. (a) Actuator and backbone lengths. (b) Actuator bending moments. (c) Tendon tension forces at the root of robot shaft. (d) Friction forces applied by tendons on robot body.

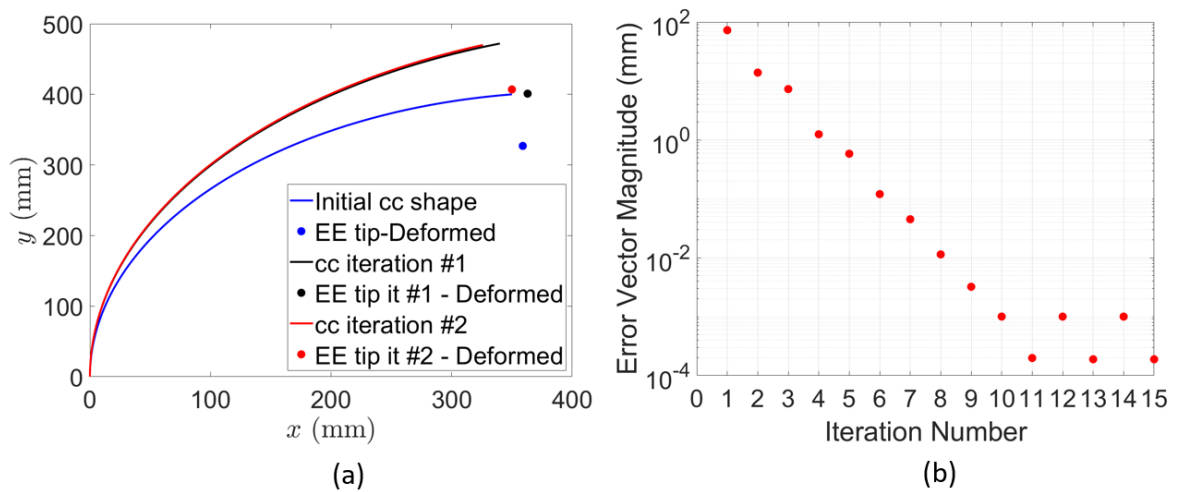


Figure 4.3. Iterative deformation correction shown with an exaggerated demonstration in 2D plane (a) Body shape and goal points plotted for each iteration (b) Magnitude of the error vector plotted on a logarithmic scale.

4.2. Quasi-static Model

The kinematic model is updated in an iterative process using the robot shaft tip deflections owing to loading on the EE as explained in Section 3.2. Figure 4.3a demonstrates the iterative process with a planar example. The blue curve represents the initial prediction to reach the goal point with CC shape. However, in actuality, the EE tip is deflected owing to tip loads. The deflected tip position is depicted as the blue dot. Error is calculated as the vector between the goal point and the blue dot, EE location is modified with the error vector, and the black curve is obtained as the first iteration. The deflected EE location given as a black dot is closer to the goal point, which indicates that the error vector magnitude is reduced when compared with the previous iteration. The magnitude of the error vector decreases after each iteration and converges to zero in a couple of iterations depending on the magnitude of the initial shaft deformation as a function of backbone length, tip loading, and actuator pressures.

A sample solution for the quasi-static model is given in Table 4.1 for three conditions where the goal point coordinate is $(180, 180, 0)$ for each condition. The first condition is for zero EE weight. The kinematic model positions the EE precisely at the goal point $(180, 180, 0)$ because the error vector magnitude between goal point and actual tip position is zero without any loading. Second, EE weight is set to 0.3 kg, where the model aims to position the EE at $(180.1, 180.0, 13.2)$. To correct deformation caused by the weight, a point that is 13 mm higher in the z-direction is aimed for the second case even though in both cases, the EE is positioned at $(180, 180, 0)$ after deformation. For the second case, the z component of \tilde{P} and x component of \tilde{M}_b become non-zero because the robot shaft is no longer on the xy plane. The third case applies a 10 N force on the EE in x'' direction that deflects the tip in the xy plane. The model aims for an updated EE position of $(180, 203.3, 0)$ such that the EE reaches the goal point $(180, 180, 0)$ after tip deflection.

Table 4.1. Model results for goal point 2 from Figure 4.1 where $(x, y, z)=(180, 180, 0)$ with and without end effector weight and external load. $E = 1.5$ GPa, $\nu = 0.3$, $d_{act} = 16$ mm, $t = 0.088$ mm, $a = 26$ mm, $\mu_{roller} = 0.2$, $\mu_{tendon} = 0.1$.

Conditions	$w = F_{ext} = 0$	$w = 0.3$ kg, $F_{ext} = 0$	$w = 0$ kg, $F_{ext} = 10$ N (x'' dir.)
l_b (mm)	282.7	282.9	295.0
l_1 (mm)	259.2	259.7	273.9
l_2 (mm)	294.5	291.0	305.6
l_3 (mm)	294.5	298.0	305.6
Deflection (mm)	[0 0 0]	[2.5 0 -30.9]	[4.3 -26.6 0]
M_b (Nmm)	[0 0 -20.6]	[3.5 0 -20.4]	[0 0 -18.5]
P (N)	[8.8 0 0]	[8.7 0 1.52]	[8.7 1.4 0]
T_{01}, T_{02}, T_{03} (N)	12.7, 11.3, 11.3	12.7, 11.4, 11.2	12.3, 11.1, 11.1
F_{f1}, F_{f2}, F_{f3} (N)	1.84, 1.64, 1.64	1.84, 1.66, 1.63	1.62, 1.45, 1.45

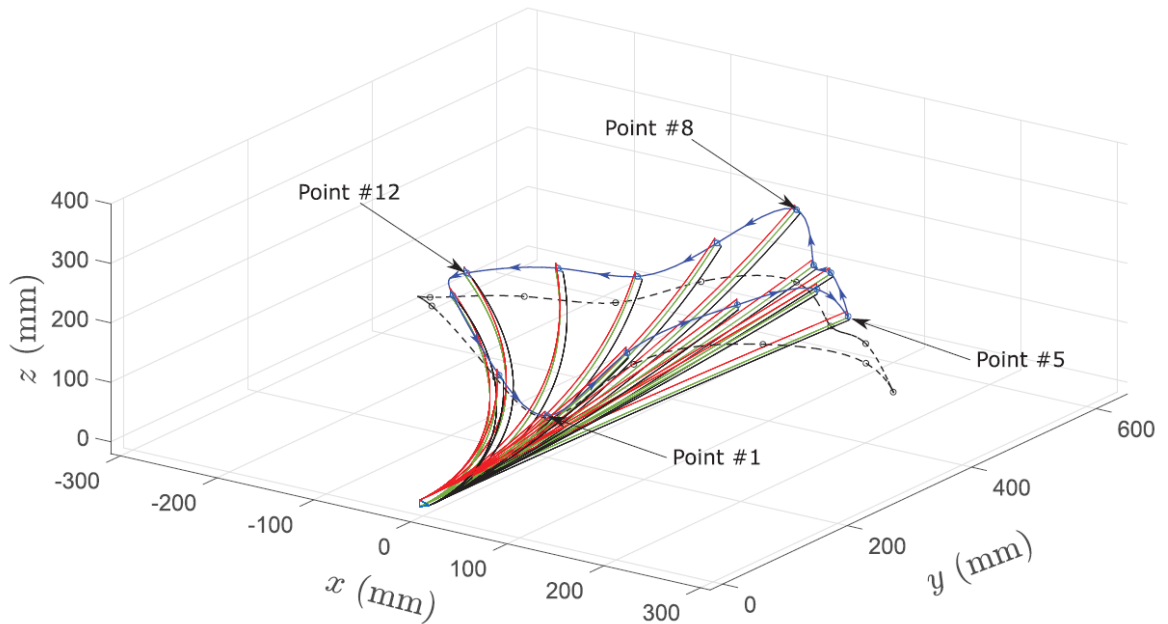


Figure 4.4. The EE follows the blue solid spline path in the direction shown with arrows from point 1 to point 14. Black dashed curve shows the path that the EE follows if the shaft deflection correction is not applied.

4.3. Path-following simulation

A path is generated via a spline curve, as shown in Figure 4.4 for simulating the proposed quasi-static model. The control parameters used in the simulation are provided in Figure 4.5 for certain via-points throughout the path (Table 4.2). Primary control parameters are the pneumatic actuator lengths that increase between via-points 1 and 8 owing to increasing distance between the shaft hub and goal point, and decrease between 8 and 14.

Tension forces \vec{T}_{01} , \vec{T}_{02} , \vec{T}_{03} are also controlled. The tension forces, which are directly related to \vec{M}_b , vary along the path as shown in Figure 4.5b.

Inflated actuator bending moments and, thus, tendon tension forces are heavily modulated by the EE angle because tension forces are dependent on the robot shaft

Table 4.2. Coordinates of via-points for the spline path shown in Figure 4.4.

Point #	x (mm)	y (mm)	z (mm)
1	0	200	50
2	50	250	150
3	100	350	200
4	150	400	220
5	150	450	150
6	100	500	180
7	50	550	150
8	0	600	200
9	-50	550	150
10	-100	500	100
11	-150	450	120
12	-180	350	150
13	-130	250	180
14	-50	200	100

geometry. Bending moment \vec{M}_b shown in Figure 4.6b is driven by the CC radius (r) that affects δ in Equation 3.8, and the backbone length l_b in Equation 3.4.

As shown in Figure 4.6b M_b decreases with the increasing backbone length (l_b), and the curvature radius (r) has a more significant effect on the moment for shorter backbone lengths. The friction force applied on the robot body by each tendon is plotted in Figure 4.6c. Friction forces have the same trend as tendon tensions (\vec{T}_{0i}) because they are directly related, as shown in Equation 3.21. Critical buckling force (\vec{F}_{crit}), which is inversely proportional to the square of backbone length, is calculated from Equation 3.12 and plotted in Figure 4.6d for each via-point.

Another simulation is performed for a massless EE traveling on the blue straight line on the xy plane, as shown in Figure 4.7a to demonstrate the effect of shaft bending

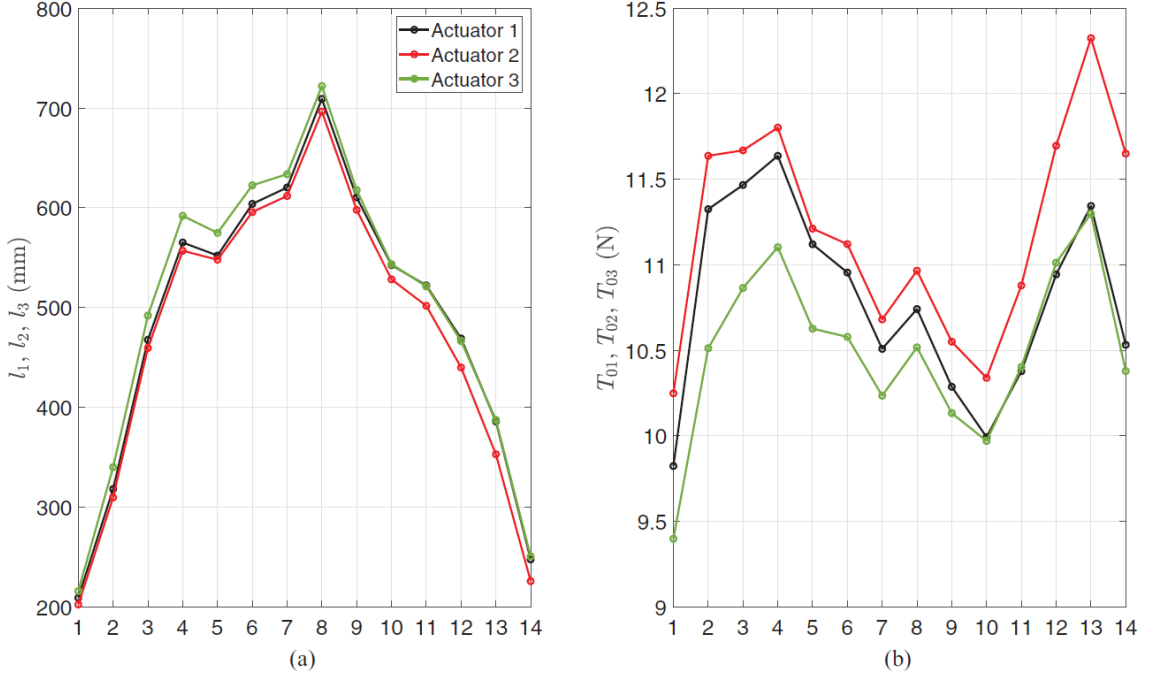


Figure 4.5. Robot control parameters at the 14 via-points given in Table 4.2 and plotted in Figure 4.4. Here $E = 1.5GPa, v = 0.3, d_{act} = 16mm, t = 0.088mm, a = 26mm, m_{roller} = 0.2, m_{tendon} = 0.1$.

stiffness on tendon tension forces. Figure 4.7b shows tendon tension forces and bending stiffness of the robot shaft for each viapoint on the path. The via-points at which backbone shapes are shown in Figure 4.7a are marked with solid circles. Tension of the second and third tendons are exactly the same because the robot is traveling on the xy plane. Tensions of second and third tendons ($\vec{T}_{02}, \vec{T}_{03}$) are the same because the robot is moving on the xy plane. As the shaft stiffness (K_b) decreases, difference between tendon tensions decrease (δT_0) to 10% at point 6 and 2% at point 12. Whereas tendon features and tension control is required for better position control of a stiff body, tendons lose their significance as stiffness decreases. Analysis performed by setting paramters to Here $E = 1.5GPa, v = 0.3, d_{act} = 16mm, t = 0.088mm, a = 26mm, m_{roller} = 0.2, m_{tendon} = 0.1$.

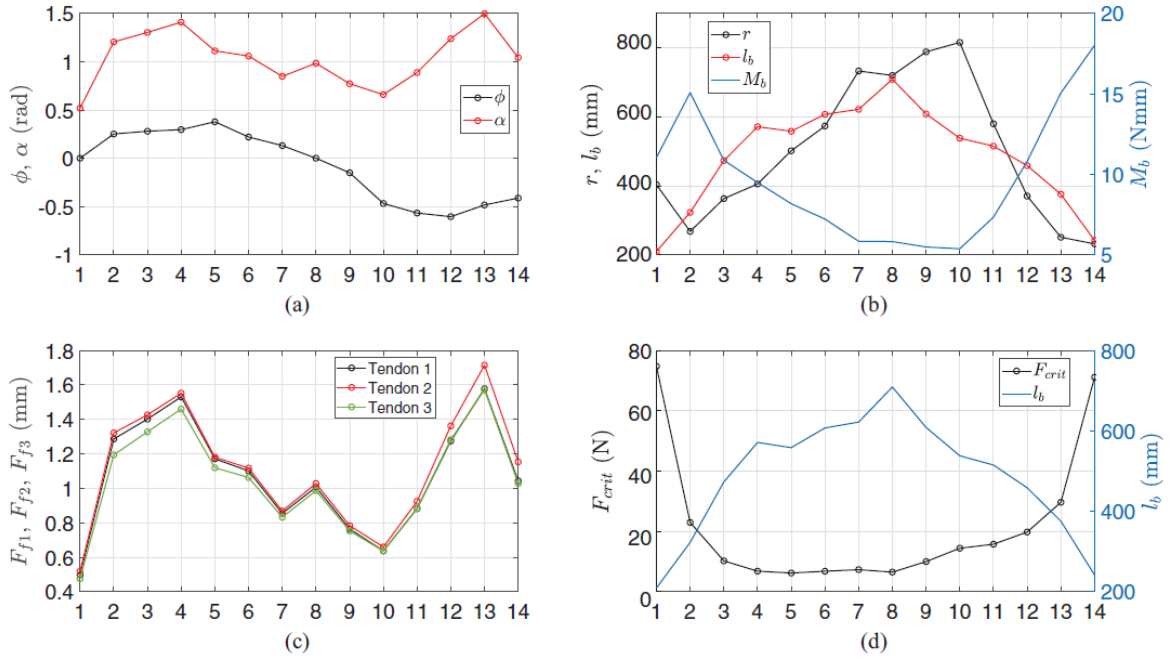


Figure 4.6. Model parameters at the 14 via-points given in Table 2 and plotted in Figure 9 where $r=1=k$. Here $E = 1.5GPa$, $\nu = 0.3$, $d_{act} = 16mm$, $t = 0.088mm$, $a = 26mm$, $m_{roller} = 0.2$, $m_{tendon} = 0.1$.

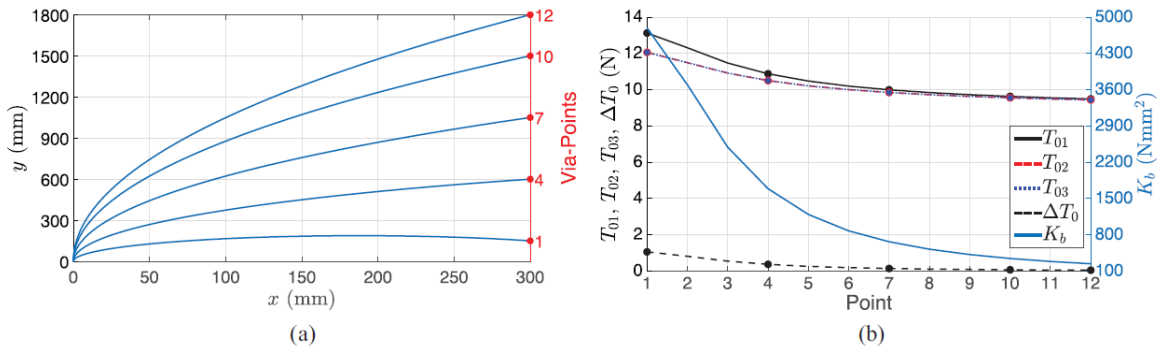


Figure 4.7. (a) Massless EE following a linear path with 12 via-points on the xy plane. (b) Change in tendon tension forces and bending stiffness of the robot shaft for each via-point on the path.

4.4. FEA Results Comparison with Analytic Stiffness Model

The deflection of a single actuator is calculated by the FEM model and compared with the results obtained from Equation 3.10. Tip deflection is calculated for different actuator lengths and weight applied at the tip to show the inflated beam's stiffness behavior. Results of the FEM and analytical model are plotted in Figure 4.8, which shows that the nonlinear hyper-elastic FEM model has a similar behavior as calculated by the analytical approach. As expected for higher deflections difference between FEM and analytical models is increased since analytical model is linearized relative to reference state and non-linear material model solves FEM with non-linear analysis settings. The difference between deflections calculated from two models is 4% for the state where actuator length is 165 mm, and the tip loading is 70 gr, and it is expected to increase as the length or tip loading increases.

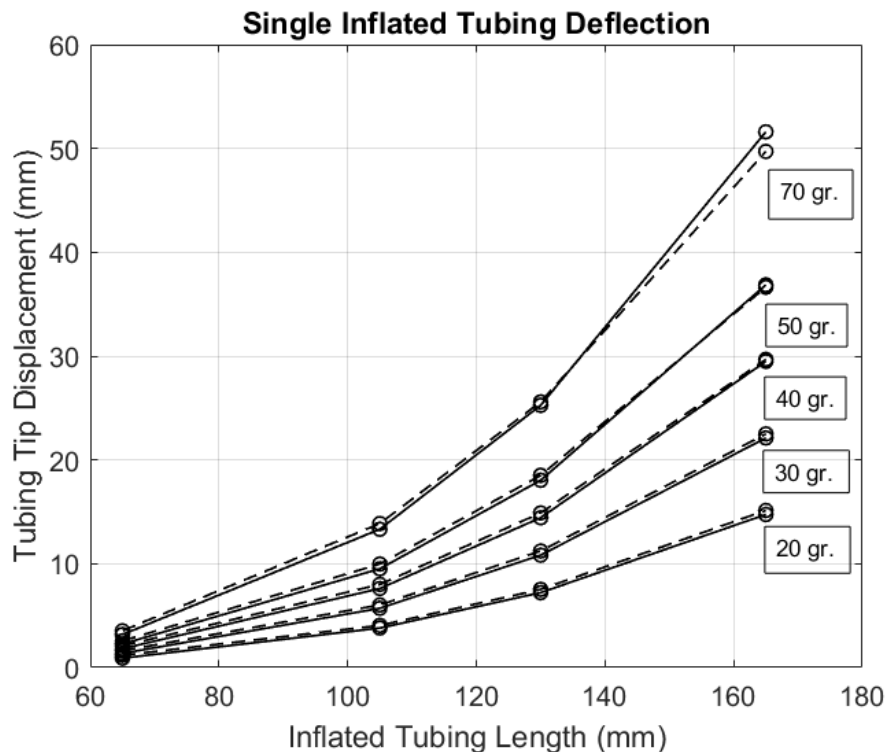


Figure 4.8. Comparison of FEM results to analytical calculation for single tubing. Solid curve represents analytic calculation and dashed curve represents FEM result.

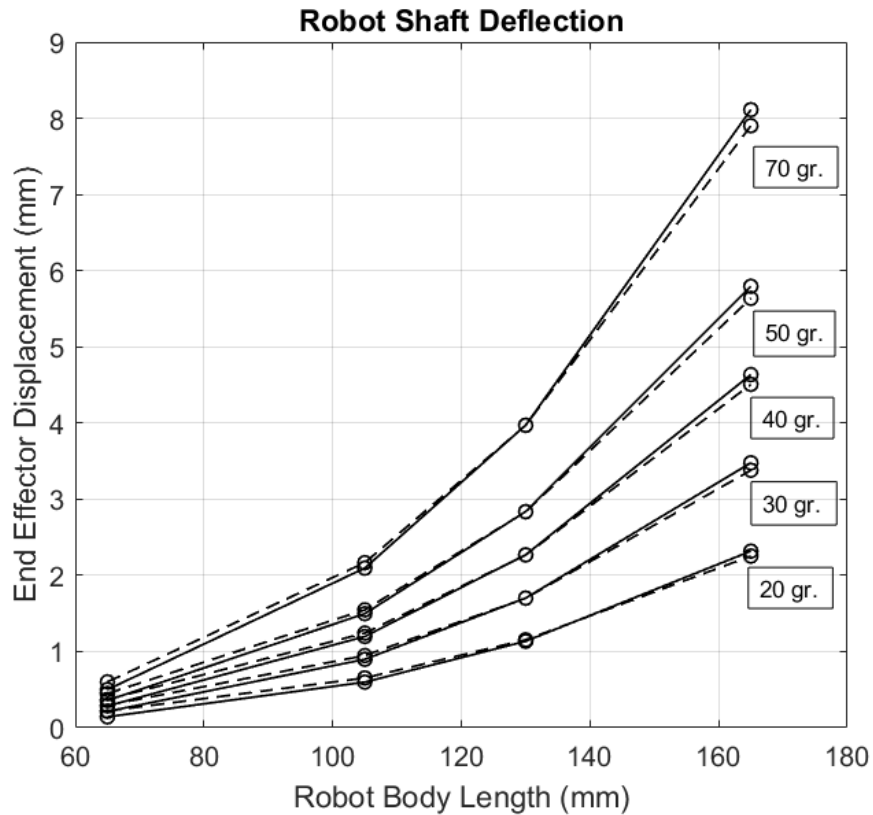


Figure 4.9. Comparison of FEM results to analytical calculation for whole robot body. Solid line represents analytic calculation and dashed line represents FEM result.

Stiffness model of the whole shaft that includes three inflated actuators is also validated via FEM, as shown in Figure 3.11 . The boundary condition of the inflated actuator that is assembled between base plane (fixed) and end effector is different from that of a single actuator loaded from the tip. In the robot body, three inflated actuators are connected to each other at the proximal end by the end effector. Based on the FEM results due to the connection type of inflated actuators to the end effector, the stiffer structure is formed, for example, when compared to the hypothetical case where each inflated actuator is loaded by one-third of the tip loading but deflecting independently of each other. The robot body stiffness is higher at the proximity of the end effector and base plate while the high stiffness effect attenuates for the middle region. For shorter robot shaft length, a mismatch observed between analytical and FEM model results, as shown in Figure 4.9. For the shaft length between 105 mm and 165 mm

analytical model has a close correlation with FEM; however, the difference increases for shaft length longer than 165 mm since the analytical model is linearized, and FEM is showing the non-linear solution.

4.5. Robot Body Stiffness and Positioning Experiments

Stiffness experiments performed on robot prototype (PV1) by applying load from the end effector and measuring the robot tip displacement as presented in [10]. Force-tip displacement measurements are compared with the stiffness model developed in [11] as shown in Figure 4.10a where solid lines are measured force-displacement curves with sigma (σ) shown as a shaded area and dashed lines represent the stiffness model estimation. Since the stiffness of the shaft is calculated via the linearized deflection model, force-deflection relation is linear; thus, the error between measurement and model increases with increasing robot body length and tip loading. For the 210 mm long shaft, the error between measurement and model estimation are calculated as 28.1% at 0.6 N tip loading, which will increase with increasing shaft length and tip loading. In colonoscopy, application robot can grow until the caecum that may require robot shaft to have length up to 1.5 m. However, due to the tortuous structure of the colon robot body is constrained and the body anchors at certain axial stations; thus, the free end of the shaft remains shorter than the whole inserted robot body. As an example, in one of the navigation tests robot body is extended by 650 mm, as shown in Figure 4.17, and the maximum length of the robot section from the anchor point is measured as 180 mm where the linearized model has a lower error. For higher length and loading, a non-linear deflection model should be used for a better estimation which is more challenging in computation.

Robot body deflection estimation is utilized for more accurate position control of the end effector. During the stiffness experiments robot end effector is aimed to be positioned at $[0,130,0]$, $[0,170,0]$, and $[0,210,0]$ coordinates with various tip loading and the deviation from the goal point is measured as the tip deflection in transverse direction as shown in Figure 4.10a. Applying the deflection correction algorithm on the

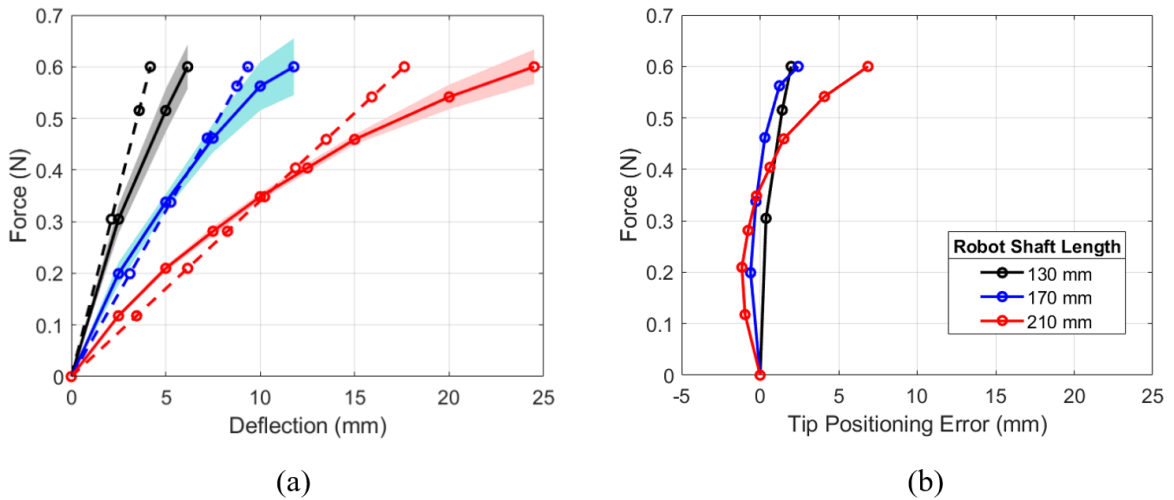


Figure 4.10. (a) Measured force-deflection relationship (solid lines) compared to model estimation (dashed lines). Shaded area is the standard deviation. (b) Positioning error after deflection correction.

kinematic model based on the goal point coordinates and tip loading as presented in [11] deviation of end effector coordinate from goal point is reduced. Figure 4.10b shows the error between end effector coordinate and goal point coordinate for different shaft lengths and tip loadings after applying deflection correction that shows considerable improvement when compared to deviations shown in Figure 4.10a. Even after deflection correction is applied, deviation of end effector from goal point is not zero, and increasing as the robot body length increases since linearized stiffness model cannot follow non-linear deflection behavior of the system.

Positioning experiments performed on multiple points in 3D space in [10]. Figure 4.11 shows the error between the measured end effector tip position and model estimation for each goal point coordinate. The highest error measured for the goal points at $y = 125\text{mm}$ is 13.6 mm while for $y = 200\text{mm}$ it is measured as 22.3 mm which is higher as expected due to longer robot body. For longer robot shaft, confidence of the model is reduced since the stiffness equations are linearized. Another parameter that may cause difference between model and reality is the geometric changes that emerged during locomotion such as tubing buckling, tubing relocations in circumferen-

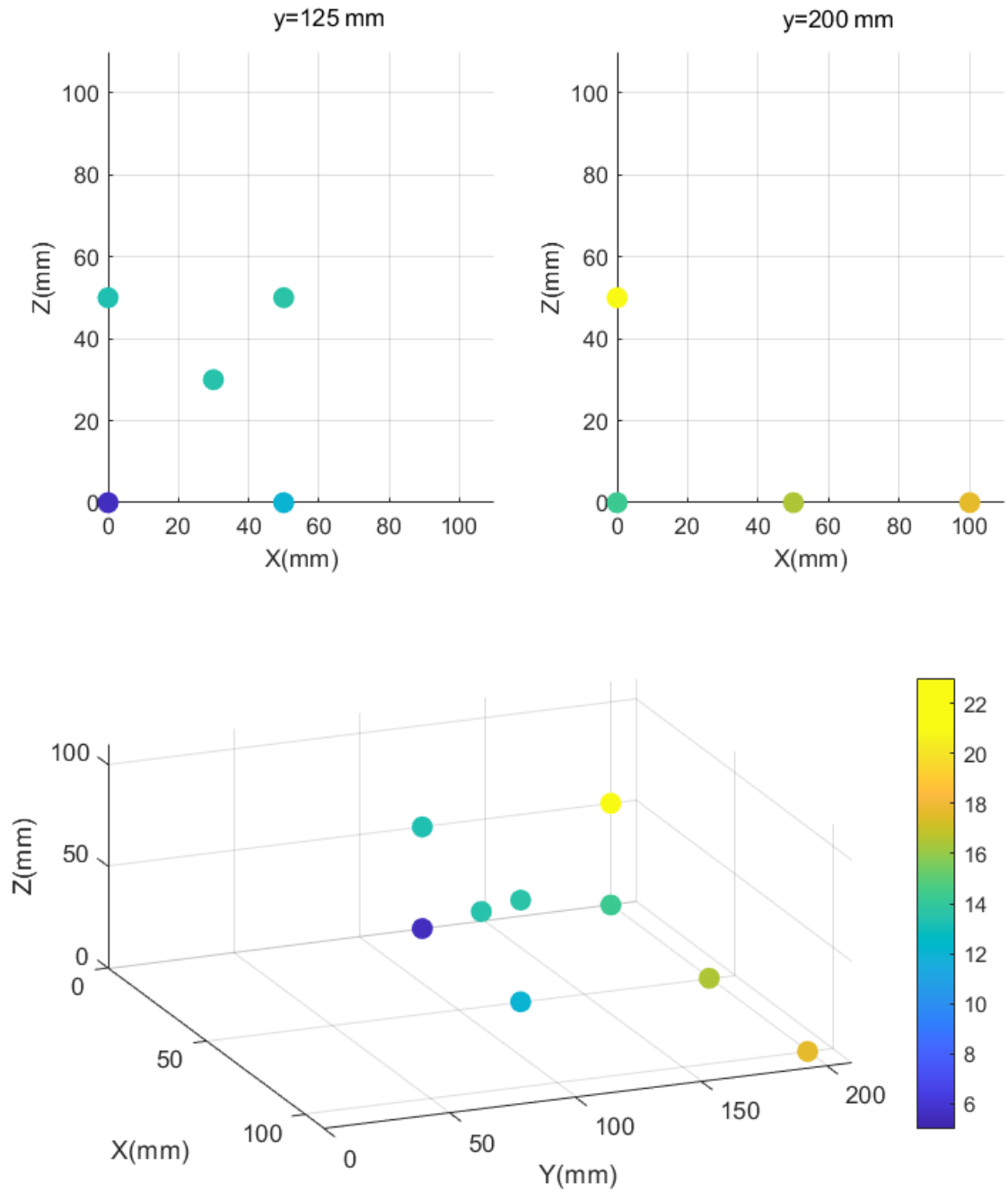


Figure 4.11. Error between measured positions and model estimate for given goal points. Each node is plotted to the goal point coordinate and color of the node indicates error. Measurements taken in [10] for axial stations $y=125$ mm, and 200mm.

tial direction, and change in radial position of tubings affect the body stiffness. Also, as shown in [10] large variance is observed for some of the position measurements due to the challenges related of measurement and repeatability of motion. These variances are a significant part of the error between model and measurement. Results show that even after applying deflection correction calculated by the quasi-static model, there will be an error between the goal point and end-effector position, as shown by Figure 4.11 because of the differences between model prediction and reality. When calculating the positioning as the ratio to the robot body length maximum calculated errors are 10.8%, and 11.4% for plane $y = 125\text{mm}$, and $y = 200\text{mm}$ respectively. Control parameters for the robot are calculated for each goal point and presented in Table 4.3. For coordinates, $(0, 125, 0)$, and $(0, 200, 0)$ actuator lengths are different from 125 mm, and 200 mm since the kinematic algorithm is aiming for a point offset a small amount in positive z axis to correct the deflection caused by end effector mass which is in negative z axis. For these coordinates difference between tendon, tensions are minor due to small curvature of the robot body. When higher curvature configurations are considered for goal point $(100, 200, 0)$, a larger difference is calculated between tendon tension which balances the bending moment of inflated actuator and the moment generated by the end effector weight.

Table 4.3. Robot control parameters for the goal points as also plotted in Figure 4.11.

Goal Point	l_1 (mm)	l_2 (mm)	l_3 (mm)	T_{01} (N)	T_{02} (N)	T_{03} (N)
(0, 125, 0)	125.0	124.8	125.3	3.48	3.50	3.46
(50, 125, 0)	131.9	140.5	141.6	4.42	3.86	3.79
(0, 125, 50)	139.6	134.0	145.2	4.06	4.42	3.70
(30, 125, 30)	131.7	133.5	140.7	4.21	4.09	3.60
(50, 125, 50)	146.7	149.3	160.5	4.57	4.42	3.78
(0, 200, 0)	200.3	199.6	201.0	3.52	3.56	3.49
(50, 200, 0)	204.8	209.6	211.5	3.99	3.78	3.70
(100, 200, 0)	225.3	234.2	237.9	4.43	4.09	3.95
(0, 200, 50)	212.4	208.3	216.5	3.90	4.08	3.72

4.6. Navigation

In this section, navigation test results for both 2D and 3D prototypes are shown. Navigation experiments performed on the 2D prototype as described in Figure 3.15 to validate the navigation capability in the 2D plane. The robot backbone is extended to 300 mm starting from 5 mm that corresponds to an extension ratio of 9.5. Figure 4.12 navigation of the robot in a closed environment is shown. The robot started from the entrance of the maze and guided to the goal point easily. The maze had a minimum radius of curvature 50 mm. In Figure 4.13 navigation of the robot through an open environment is shown. In this type of maze, robot is steered to avoid obstacles and enter from the narrow passage. Experiments on 2D maze showed a good demonstration of navigation capabilities of the 2D prototype.

Navigation tests are repeated with 3D prototypes PV1 and PV2. In Figure 4.15, images from the navigation tests of PV1 are shown. During the experiments, robot is controlled using omega 6 to steer the robot through obstacles and maze structures. In Figure 4.15a robot lifts weight of 200 g. In Figure 4.15b maneuver of the robot to the goal point indicated as yellow is shown at free space. One of the challenging navigation tests is the robot passing through the small obstacle and reaching to the goal point as shown in Figure 4.15c, similarly on Figure 4.15d robot enters the closed cavity that has an inner diameter of 70 mm requires precise control of the end-effector

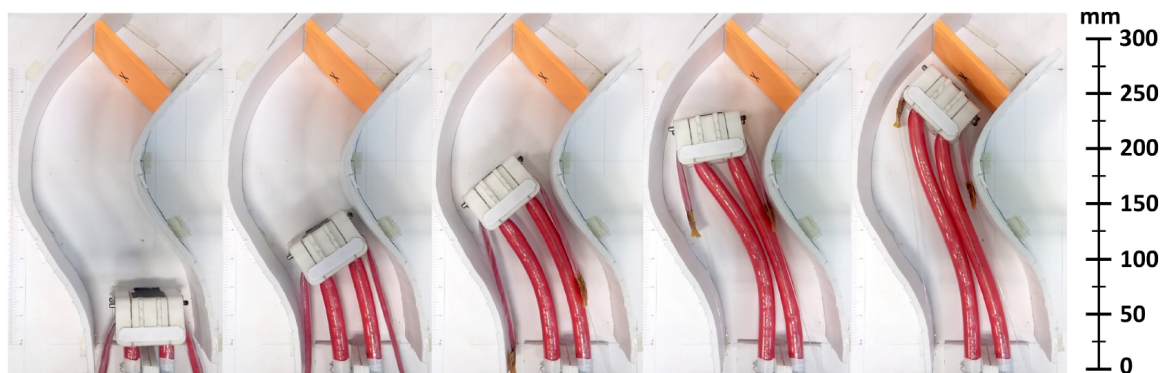


Figure 4.12. 2D prototype navigation on closed maze path [119].

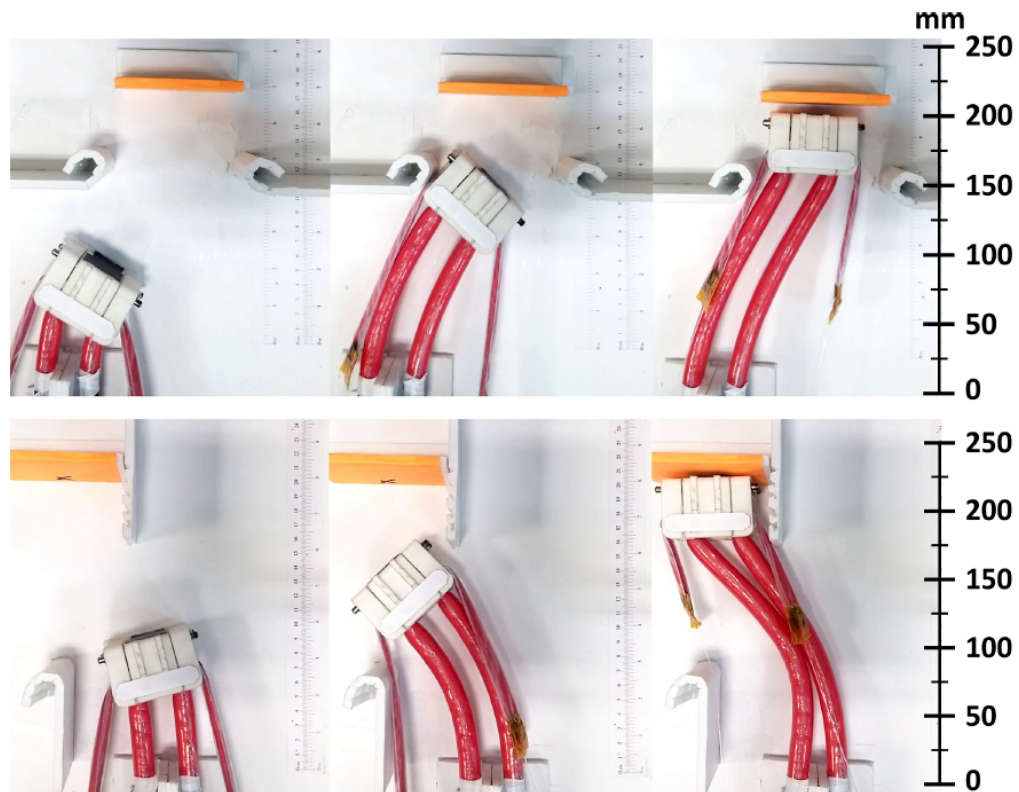


Figure 4.13. 2D prototype navigation on open maze path [119].

position. As shown in Figure 4.15e robot is progressing inside the closed cavity maze, which is similar to the human colon. The sharp turn shown in Figure 4.15e mimics the Sigmoid colon's geometry. Despite the friction between the close cavity maze and robot body, the end effector progresses through the maze without any problems. The navigation test is performed on the PV2 as well using a longer closed maze, as shown in Figure 4.17. The experiment was performed by starting the end effector from the entrance of the maze and steering the end effector by user input until reaching the target at the end of the maze. For this test end effector is controlled using omega 6. As the navigation test being done, force applied by the end effector to the maze wall is measured. As the robot is navigated through the closed maze, the camera image is reflected in the user interface, as shown in Figure 4.14.

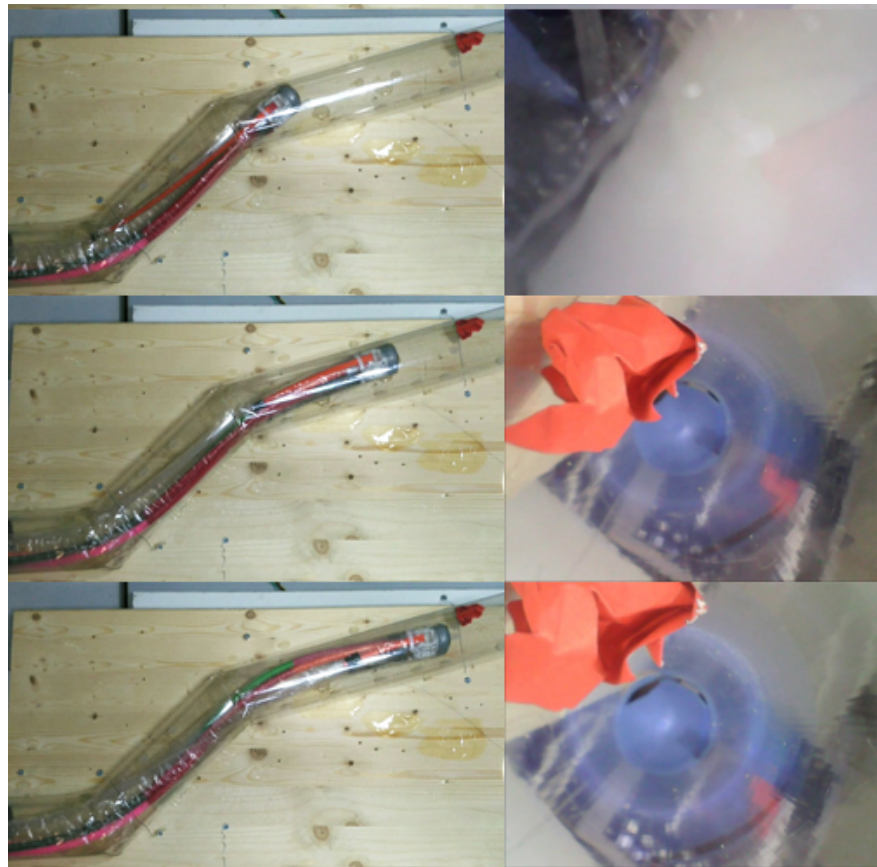


Figure 4.14. PV2 Navigation camera image.

4.7. Robot Wall Reaction Measurements

The reaction force between the robot body and the maze wall is measured as the robot advances to the goal point, indicated with the red object at the end of the maze. Force is measured in three directions, and the resultant force is calculated as plotted in Figure 4.16. Peaks on the plot are numbered based on the change in anchoring point of the body and end effector-wall contact point, as shown in Figure 4.17. The maximum reaction force is measured as 0.82 N at point “1”, at the entrance of the maze. Reaction forces vary with the change in contact points and generate a continuous contact force starting from point “3” with an average value of 0.35 N. The average speed of the robot is calculated as 5.5 mm/s as the robot travels from the entrance of the maze until it reaches to the goal object.

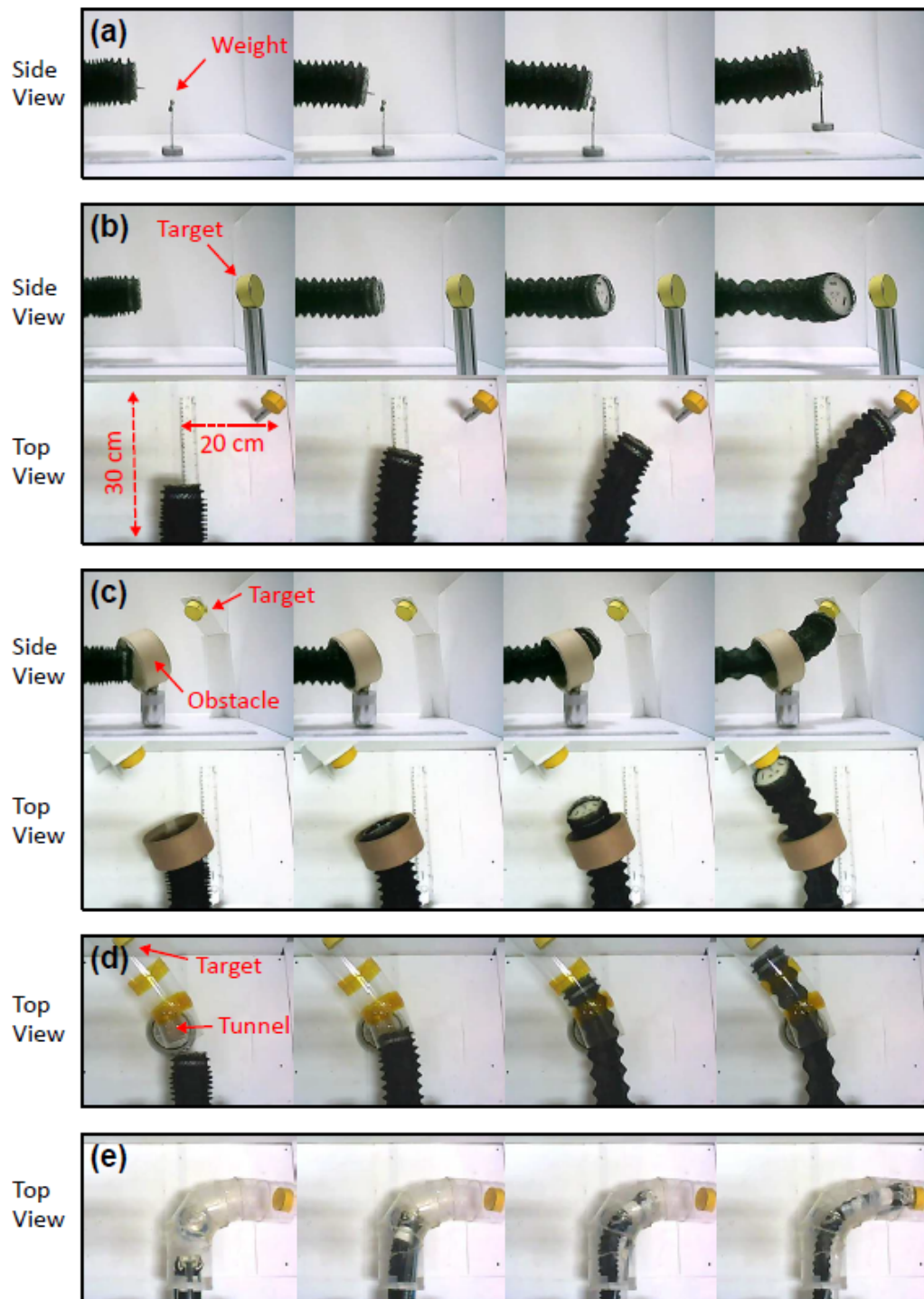


Figure 4.15. PV1 navigation tests. Lifting weight of 200 g (a) Navigation through open space (b) Passing through narrow obstacle and reaching to target (c) Entering to a tunnel and meets with the target (d) Following a closed cavity maze [119].

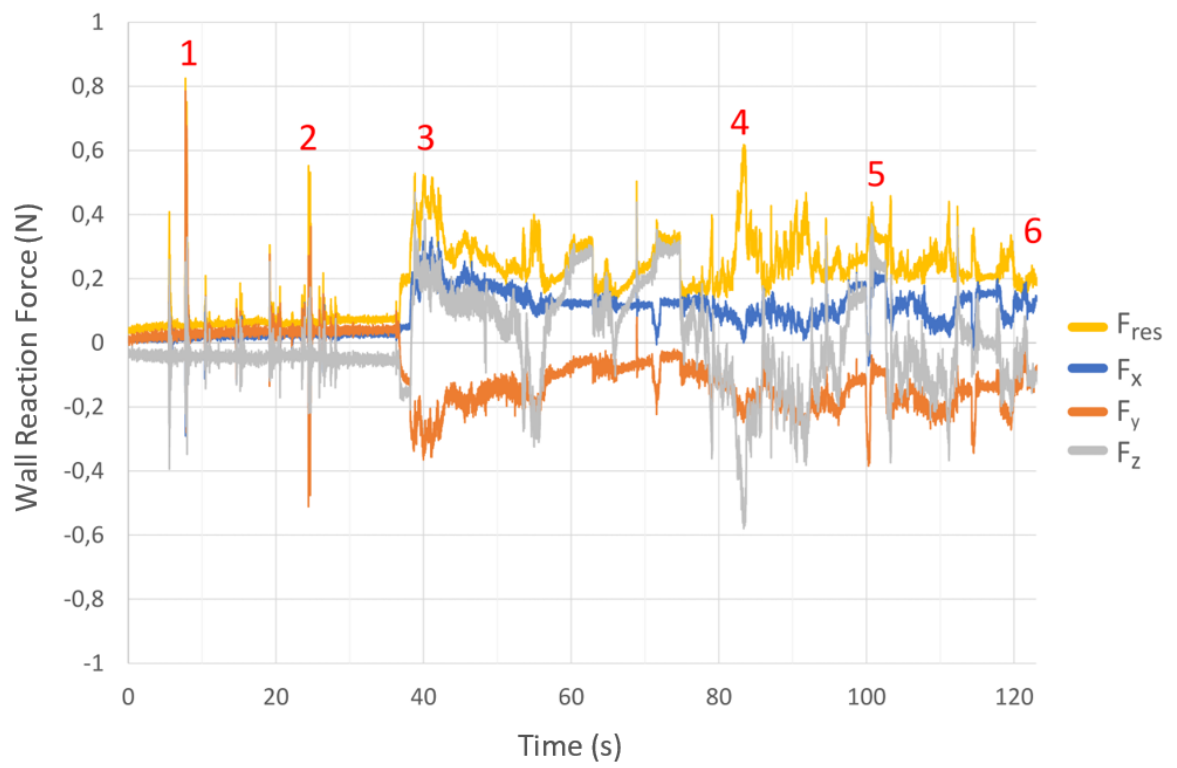


Figure 4.16. Wall reaction force measurement.

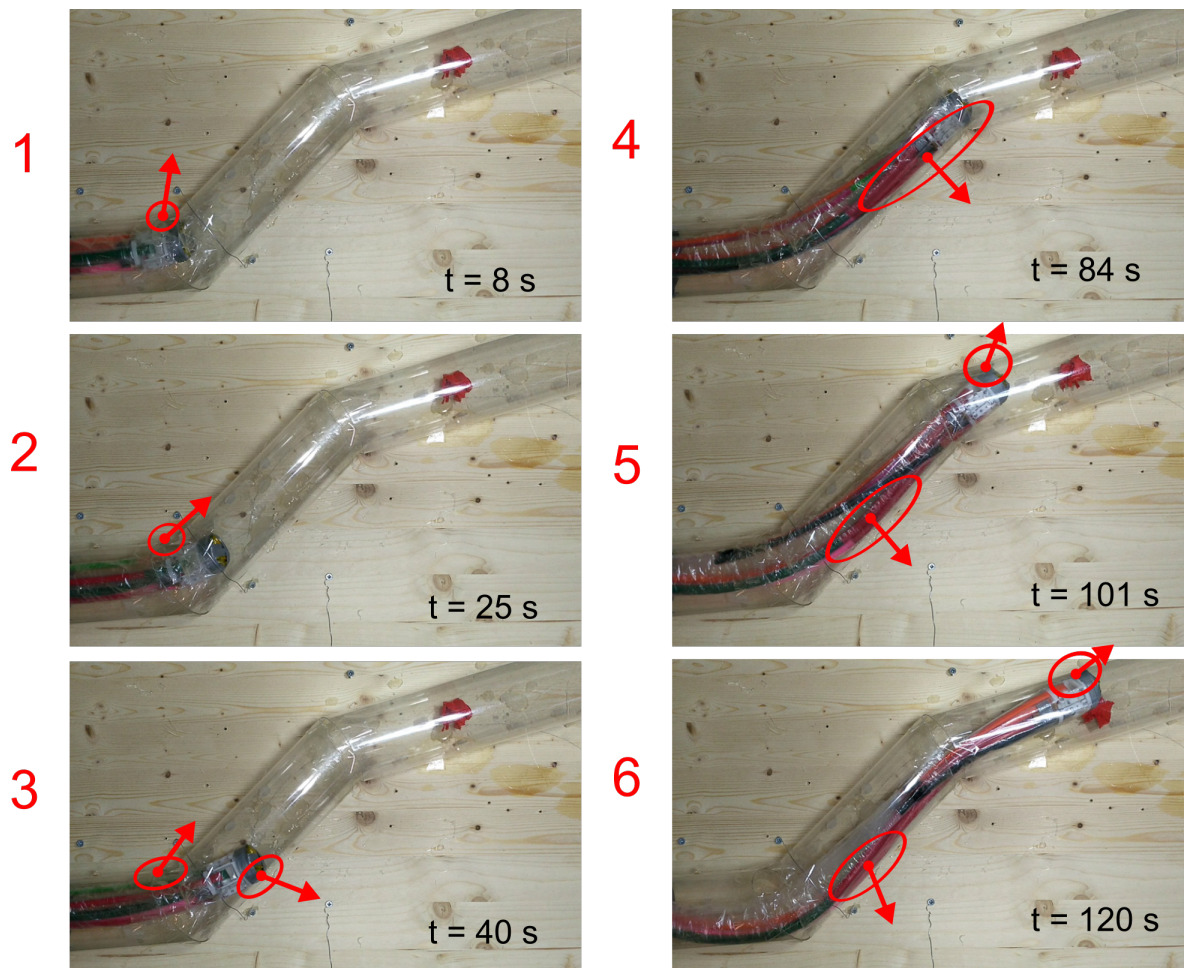


Figure 4.17. Robot progress in the maze during wall reaction measurements.

5. DISCUSSION

The system presented in this study provides improved locomotion for possible colonoscopy applications as a growing type of soft robot. As the significant difference from the conventional colonoscopy, propulsion is applied from the tip that facilitates more stable locomotion and low reaction forces. As reported in [121], during the conventional colonoscopy, maximum applied force is measured up to 16.1 N. In another study, peak applied push force is measured as 29.4 N, and 9.81 N as the continuous force application [25]. The proposed robotic system reduces robot body-wall reaction forces compared to the conventional colonoscopy (the proposed system reactions: maximum peak: 0.87 N, continuous: 0.35 N). Test data shows that the maximum force that can be generated by all three actuators is 19 N [119], however the robot can proceed in the maze by applying much lower reaction forces. Colon perforation forces are reported for various colonoscope tip configurations in [38], which is measured as 14.08 ± 2.18 N for the large (I) shaped configuration as the minimum force that results in perforation. (I) shaped configuration is considered to be the riskiest when the end of the colonoscope is being pushed into the colon wall that exceeds the force required for perforation since the applied force could be in the range of 9-21 N based on this study. Although it is not frequently reported, colon perforations are observed for a conventional colonoscopy since the applied force range exceeds the limit for failure in some cases. The robotic system has a considerably low wall reaction force compared to the minimum perforation limit that may provide safe operation. However, to show the improvement over the conventional colonoscopy, a back to back comparison has to be made by testing the system in the colon or in a colon model. For the operation in the colon, higher friction forces thus higher wall reaction forces are expected for the proposed system. In this case the improvement margin quoted with the results of maze testing may be reduced.

Robotic systems proposed in the literature are also aiming to reduce the force applied to the colon wall. One of the robotic colonoscopy systems, NeoGuide has demonstrated that the forcing on the colon wall reduced successfully [122]. Reac-

tion force experiments performed by in-vitro testing on inanimate flexible colon model showed that the maximum peak force is 20.47 N, and the average is 12.1 N [122]. Although the NeoGuide system reduced the colon forcing with the advanced steering mechanism, the robotic approach presented in this study has a lower reaction force due to the advantage of the tip growing and pulling the robot body from the tip. Another robotic approach, namely the Endotics system, has a locomotion mechanism similar to inchworm that actuates the system from the tip. The system has gone through clinical trials and in-vitro tests, and the peak reaction force was measured as 0.95 N similar to the peak force measured for the robotic system presented in this study (0.87 N). During the clinical trials, pain and discomfort scores of the Endotics system and the conventional colonoscopy were compared using a scale from 0 to 10. Pain and discomfort scores were observed as 0.9 and 1.1 respectively for the endotics system, while the conventional colonoscopy had pain and discomfort scores of 6.9 and 6.8 [44]. Mechanical forcing and colon stretching are considered to be the reason for pain and discomfort [19], thus comparing the reaction forces of the Endotics system and the proposed robotic approach, a similar improvement related to pain and discomfort may be expected against the conventional colonoscopy. The Endotics system is providing an advantage for mitigation of forcing; however it is used for screening purposes and has lower locomotion speed compared to other pneumatic actuated systems such as the Aero-Scope, Invendoscope, as well as the robotic system presented in this study [45]. Although validation tests of the robotic system performed on a large scale maze having a size that mimics the dimensional ratio between the colon and conventional colonoscopy, reaction force measurements should be performed at the small target scale with medical colon models to present more reliable benchmarking.

The average speed of the robot is measured as 5.5 mm/s in the maze test shown in Figure 4.17. The speed of the robot is compared with other robotic systems presented in the literature. Average speed until reaching the caecum is calculated from the caecal intubation time summarized in [123], by assuming the minimum colorectal length of 1200 mm as measured in [13]. As a result, the average speed during caecal intubation is calculated as 0.7 mm/s for the Endotics robotic system, 0.9 mm/s for the NeoGuide,

2.8 mm/s for the Invendioscope, and 5.7 mm/s for the Aero-O-Scope at maximum. Considering the actuation principle, the Aero-O-Scope can be used as a benchmark due to its similarity with the proposed robotic system. Experiments performed in the maze showed that the average speed measured for the robotic system (5.5 mm/s) is similar to the average speed of the Aero-O-Scope. However, both designs have higher speed than the other robotic systems due to the advantage emerging from tip actuation by air pressure rather than applying push load from the proximal end, or inch-worm locomotion.

The navigation capability of the proposed robot has been proved with the experiments for essential maneuvers, as presented in [10] detailly. Accurate end-effector position control is desired for therapeutic interventions to approach the tissue at the required tooling orientation. The performance of robot maneuvering is tested by subjecting the prototype to various navigation tests. Open-loop navigation experiments show that the robot tip is controlled accurately to meet the goal point. In addition to the open-loop navigation tests, position control experiments performed by providing the goal point coordinate to the robot kinematic algorithm, which calculates required tube lengths to reach a given goal point coordinate. The error between the goal point coordinate and the end effector coordinate at the end of motion is increasing for longer body length and higher tip loading. Applying a correction factor to the robot kinematic algorithm calculated by deflection estimation reduces the positioning error. For the condition given in Figure 4.10, the end effector can be positioned accurately for up to 210 mm body length with an error of less than 6.8 mm. Considering that the length of the free region measured between the anchoring point and the robot tip is likely to be below 210 mm, it is possible to have accurate position control with the quasi-static deflection model presented in [11]. Although the operator's feedback is corrected during the open-loop control with the feedback received from the camera, the model may be utilized to enhance the control. Without the deflection correction control input parameters such as the angle of control grip required for specific robot, the tip rotation angle varies majorly with the robot body length, loading, and robot body geometry. Thus, it is possible to utilize a quasi-static deflection model to reduce

the variation in the control characteristics. Furthermore, the model may be used for automatic navigation by providing goal point coordinates. The robot is also tested in a constraint environment as documented in [10]. In this test, robot follows a path with a sharp turn similar to sigmoid colon geometry by overcoming the friction between the tunnel and robot body that proves the concept for operation in similar environments. One of the important parameters for colonoscopy application is the minimum radius of curvature which is calculated as 50 mm for PV1 [119].

The electromechanic control interface of the robot has the capability for distant control that allows a more ergonomic working environment for the colonoscopist. This control interface facilitates coordination between propulsion and maneuvering since single control lever can control both functions, eliminate the need for two-man method, and provide better control with single hand control. A control interface different than the conventional colonoscope control hub may introduce challenges related to adaptation to the new system, especially for the experienced colonoscopists who have gained muscle memory on the conventional method. Colonoscopists will be aware of their conscious incompetence on the new device and unlikely to leave the technique they have already gained unconscious competence [24]. Although challenges introduced related with the control interface, medical robotics is an emerging technology, and the conventional control interface will experience a shift to an unconventional state to support the progress of medical robotics. The control interface used in this study is an off the shelf haptic device (Omega 6, Force Dimension) that can be adapted medical applications such as Sensei robotic catheter system (Hansen Medical), which is an application similar to the colonoscope. Such haptic devices are expected to become the new norm of the medical systems with increased penetration of robotics in medical procedures. Haptic feedback is required to generate tip reactions at the control interface end for enhanced control. In this study, haptic feedback from the colonoscope tip is not implemented, and it is considered as a future work.

The proposed robotic approach is addressing the future colonoscopy competencies as summarized in Table 2.2 by mitigating patient pain and discomfort, reducing

operation-related complications, and improve colonoscopist ergonomics during operation. In addition to these competencies, the proposed system has the potential to have a disposable body since the costly electromechanical actuators and steering systems are placed at the in-vitro section out of the body. The disposable colonoscope body has the advantage of removing the infection risk that may be a strong criterion for preferring the system.

The quasi-static model presented in this study is developed for a pneumatically driven growing soft-continuum robot. For this reason, inflated actuator stiffness is also considered during the calculation of EE reactions. As the bending reaction moment, M_b , is highly dependent on inflated beam length as well as shaft curvature, the reaction is significant for shorter shaft lengths, as shown in Figure 4.6b. Therefore, the inflated beam stiffness calculation approach for growing-type pneumatically driven robots differs from the approach for constant-length pneumatic continuum robots such as Festo's bionic arm [102, 107].

Results in Table 4.1 show that loading on the robot shaft has a significant effect on the EE positioning; thus a kinematic model alone is not sufficient to control the EE position for applications with non-negligible loading. Owing to the needs of the proposed application [110], EE position should be controlled. A slight difference between tendon tensions for a certain EE position is required to balance the bending moment. The difference between tendon tensions is necessary to maintain EE position at a certain goal point in quasi-static equilibrium, otherwise, the shaft will be deflected owing to excessive reaction moment, which will yield inaccuracy in positioning. Displacement and position of the EE are calculated per deformed shaft geometry because it is a function of shaft deformation. However, the overall shape of the shaft after deformation is not discussed. Buckling is a significant limitation for soft robots that have low shaft stiffness. In Figure 4.6d critical buckling force decreases with increasing shaft length owing to a reduction in shaft stiffness.

The model presented in this article investigates the problem on a free space, whereas a colonoscopy application presented in [110] utilized the surrounding colon structure as a support, and would have higher stiffness compared with the free-space application. Furthermore, the buckling limit can be increased by adding stiffening rods or tubes through the shaft as a feature. The stiffness model includes stiffness of the inflated tubes and the backbone of the robot however does not account for the changes in the robot body stiffness when the tool or water/ CO_2 channels are used. The robot body stiffness is expected to increase when a tool is introduced due to additional stiffness of the tool wire. Also when the water or CO_2 channel is used, stiffness of the channel increases due to fluid pressure, and it can be modelled via the relation given in [115]. Tip displacement owing to shaft deformation is accounted for in the model in an iterative process that may aggravate a model-based real-time control application; however, it is possible to generate pre-computed lookup tables to minimize the computational cost.

In Figure 4.4, the blue spline curve represents the path followed by the EE with the control parameters given in Figure 4.5a. These parameters are calculated with the iterative process, as demonstrated in Figure 4.3, to apply a correction for shaft deflection. If the deflection correction is not applied, the EE will follow the spline path shown as a dashed black line instead of the desired trajectory shown as a solid blue line. For EE positions where the robot shaft has a shorter length, such as points 1, 2, and 14, the error between the two trajectories is small such that the error vector magnitude is 3.5 mm at point 1. However, the error increases with increasing shaft length owing to decreased stiffness, and the error vector magnitude reaches 119 mm at point 5. Results show that a quasi-static model is needed to calculate the robot control parameters owing to large positioning errors because of shaft deformation, especially when the robot shaft is considerably long. Growing robots evolve their bodies through the addition of material, and locomotion is performed by growing the body and not by an external component [111]. The soft continuum robot modeled in this study is considered to be a growing-type robot because it grows by adding material from the tip similar to [72, 112, 113].

The robot is modeled based on constant curvature kinematics that may not be applicable for cases where the robot body is shaped by the surrounding structure. The quasi-static model of the robot is developed for a free space application. The approach holds for the cases where long robot body is supported and anchored by the colon at certain axial stations, and a shorter part is growing in a free space. Prototype testing also demonstrated the behaviour of anchoring of the long robot body and free growing tip consistent with the modeling approach. Another limitation of the modeling approach is the stiffness model that is solved by linearization. Thus, the error between model and true displacements are increased for longer robot shaft.

5.1. Medical Certification Procedure

The robotic colonoscopy device developed in this thesis has the potential to be used in a medical application in the future. To introduce the device into medical market, the FDA or European Union CE certification has to be obtained. The certification procedures require a product to conform to certain standards and requirements to ensure safety and quality of the medical application.

The first step for FDA certification is to determine the medical device's classification by searching the FDA classification database. Per FDA guidance, a colonoscope is classified as a Class II device and subjected to 876.1500 regulation number. As a Class II device, the robotic colonoscopy system has to implement Quality Management System (QMS) per FDA Quality System Regulation (QSR) given in 21 CFR Part 820, which is superseded by ISO 13485 recently. Due to its classification, the device requires clinical trials. The FDA's pre-submission consulting program aims to provide support through design of clinical or non-clinical study protocols for medical device manufacturers and designers. Clinical study protocols are designed in concurrence with the FDA. After completing the study, 510(k) Premarket Notification application is submitted, and the related fee is paid. As the next step Premarket Approval (PMA) the application is placed and the application fee is paid. After these applications, FDA issues a 510(k) clearance letter, and posts it online. At this step, FDA requires prod-

ucts to comply with QSRs and thus have legal right to conduct random inspections. If a nonconformance is identified, Form 483 is issued requiring product owners to take necessary actions to correct the non-conformance. As the last step FDA appoints a representative as a local point of contact, and the device is registered using FURLS system on the FDA website. After completion of the registration process, the device has clearance to be sold in the USA. The authorization does not expire as long as the device design and intended use are not changed [124].

Proving safe operation is vital for Class II medical device certification. Identifying the safety risks, and taking the preventive actions through the design phase increases maturity of the product for medical certification. For the proposed system in this thesis, risks and a mitigation plan is listed below:

- (i) Actuator burst that may cause pressurized air leakage to the colon
 - Adding safety valves to the pneumatic system that cuts the fluid flow as air leakage is detected
 - Water may be used as the pressurizing fluid instead of air which does not expand as air as it leaks
- (ii) Applying excessive force to the colon wall
 - Fluid pressure may be limited to a certain value where the total push force does not exceed the critical threshold for colon perforation
- (iii) Damaged electrical lead wires of the light source and camera may yield electric hazard for patient
 - Light and image can be transferred via fiber optics to remove electrical hardware from the colon body

6. CONCLUSION

Colonoscopy is a widely used screening method to detect CRC and abnormal tissue in the colon. The method currently used for the colonoscopy operation often yields patient discomfort and serious operation-related complications such as colon perforation in some extreme cases [17, 18]. Complications are also reported for colonoscopists such as musculoskeletal injuries due to long term colonoscopy usage. The proposed system's objective is to mitigate discomfort and complication risk on both patient and colonoscopist via a robotic approach. A novel growing soft robot is presented in this thesis that has a potential use in colonoscopy application. The proposed system is a soft continuum robot that advances by growing from the tip. The end effector is actuated by a PRD (Pinch Roller Drive) mechanism with the pressurized pneumatic tubings. Three tubings are located in the robot body with equal circumferential spacing that allows orienting end effector in three degrees of freedom. Working principle of the proposed system and design features are explained in [10–12, 110] in detail. Haptic feedback from the colonoscope tip is often lost during conventional application due to long flexible colonoscope shaft that results in excessive push force. As given in the literature [20], force applied to the colon causes the colon wall and ligament stretching, which is identified as the source of pain and discomfort. The actuation approach of the proposed system yields lower reaction forces than the conventional colonoscopy by propelling the robot shaft from the tip. Also, the system is compliant with the human colon due to its soft continuum structure. Since the system is teleoperated and the propulsion force is generated via the pneumatic actuation and mechatronic systems, the effort required from colonoscopists is reduced significantly.

The first prototype has been developed to prove the pinch roller drive mechanism concept in 1D, and test various type of actuator tubings. The concept was further validated via 2D prototypes by demonstrating basic maneuvers and proving the controllability of the system. Two different 2D prototypes have been developed and manufactured to improve the mechanism design to address the problems identified

during validation testing [119]. As the requirement of the application, 3D prototypes have been developed to control and guide the robot in a 3D space. The first developed 3D prototype (PV1) has 310 mm length and 50 mm outer diameter. The robot was guided through various types of maze during testing and controlled via the Omega 6 user interface [10]. A revision has been implemented to 3D prototype (PV2) to optimize the pinch roller drive mechanism, and increase the robot body length. As the result, robot body length is increased to 1000 mm, and the outer diameter is reduced to 40 mm. This prototype was used for navigation tests in a constraint environment and measuring the reaction force applied by the end effector. A small scale prototype that has 15 mm outer diameter has also been developed and manufactured. The small scale prototype was not used in the validation testing since the actuator tubing suitable for this size was not flexible enough to sustain the pinch roller drive mechanism's smooth motion.

Tubings of various materials and dimensions were tested for pinch roller drive mechanism. A Nylon 12 medical balloon with thin wall thickness is considered for the first prototypes of the robot, which showed a major leakage problem and length limitation to 250 mm. Further testing showed that the highest propulsion force is generated by the double-layer tubes with Latex inner layer and LDPE outer layer. The soft LATEX layer fills the micro gaps that occur between the roller contact edge, thus maintains the air seal between pressurized and deflated parts of the tubing. Outer LDPE layer provides a radial constraint for the LATEX layer, which may expand significantly with applied pressure. A co-extruded tubing has been developed for the small scale prototype with Pebax as the inner layer and Nylon 12 as the outer layer. Tests showed that the co-extruded tubings were not flexible enough to generate sufficient propulsion force and maintain smooth motion. The required tubing thickness cannot be achieved due to limitations on manufacturing, such as a wide tolerance range of Nylon 12 layer thickness.

As a part of the thesis, a quasi-static model has been developed for the growing soft-continuum robot, as documented in [11]. The quasi-static model aims to estimate

forces acting on the robot body and end effector as a function of robot body geometry and external loading. The purpose of developing such a model was to calculate the deflection of the soft robot for more accurate control of the end effector. To calculate the forces generated due to bending of the robot body, an inverse kinematic model is solved that converts task space variables into configuration and actuator space variables. The kinematic model approximates the shaft geometry using the CC approach, which is the input for the quasi-static model. The reaction moment generated by the bending of the inflated actuator is calculated based on robot body curvature and length. Forces on tendons are calculated to balance the inflated actuator bending moment and external loading, also considering the internal friction acting between tendon and robot shaft. Control parameters, namely actuator lengths, and tendon tension forces, are calculated as the functions of robot body geometry, EE loading, robot shaft internal friction, and actuator pressure. Robot shaft deformation is computed, and the kinematics is updated to correct for the EE deflection. This correction is performed using an iterative algorithm with an objective to minimize the error between the goal point and the deflected tip of the robot body. The model was simulated on a path, and the model parameters were provided for certain via-points.

The concept has been proved via in-vitro experiments using the large scale 3D prototypes. Test setups have been designed such that dimensional relation between the prototype and the test setup mimics the size of a conventional colonoscopy and the colon. The first 3D prototype (PV1) proved the robot's maneuverability in 3D free and constraint space. Those tests were also performed to validate user interface with the codes developed for robot control. This prototype was also used for force generation, speed, and bending stiffness measurements. The improved 3D prototype (PV2) is tested for navigation in 3D constraint space in a long maze, which better mimics the colonoscopy application. The reaction force between the robot and the maze wall is measured and plotted against the path followed by the robot. Validation tests showed that the robot was controllable through various types of constraint environments. Considerable reduction in reaction force between robot and wall was achieved with the proposed robotic system compared to the conventional colonoscopy.

Position control was performed using the kinematic model, and the error between goal point and end-effector position was measured which is emerged due to robot body deformation. The error was compared with the quasi-static deflection model estimation, and that showed agreement. It is concluded that positioning errors caused by the soft robot body deformation may be reduced implementing the quasi-static model that may be further improved by using a non-linear deflection model.

6.1. Contributions and Originality

The proposed robotic system is a growing type, thus, generates the propulsion force applied at the robot tip, pulling the rest of the robot body. This propulsion approach has an advantage against systems pushed from the proximal end by achieving more stable control and reduced reaction forces between the end effector and the colon wall. The soft body structure of the proposed system allows compliance to the colon shape compared to the rigid linked robots. Although robotic colonoscopy systems presented in the literature [36, 38, 42, 43, 122] have soft robot shaft that are compliant to the colon structure, they are actuated by pushing whole body from the proximal end. Thus, the proposed system presented in this thesis has the advantage to actuate the system from the tip to achieve lower reaction force applied to the colon wall. The reaction force applied by the proposed robotic system was compared to the conventional colonoscopy and the robotic colonoscopy systems presented in the literature in Chapter 5. As the result, the reaction force applied by the proposed system to the surrounding structure is lower than the conventional colonoscope and the robotic systems presented in the literature that are pushed from the proximal end. However, this comparison is presented based on in-vitro test measurements that needs to be further validated via in-vivo clinical trials. The robotic solutions that are propelled from the tip are also presented in the literature such as Aeroscope [34]. However for this design, it is required to inflate the whole colon for actuation that may cause patient discomfort [20]. Also this system is only used for imaging and not for surgical interventions since this system has no working channel. Colonosight [33] propulsion principle is very similar to the robotic system proposed in this thesis; however, the system has only single degree of freedom

pneumatic actuation. Although inch-worm [44,46–48] or caterpillar type robots [50,51] are applying the propulsion force from the tip however moving with a low speed and are not used for therapeutic purposes. In-vitro experimental data shows that the proposed system can move at higher speeds compared to inch-worm or caterpillar type robots as discussed in Chapter 5. Continuum robots introduced in the literature that may have potential colonoscopy application [72,74,76,78–80] is also compared to the proposed system. Chapter 2 shows that the proposed system is providing advantage by controlling robot body shape in 3DOF, and decoupling the stiffness and force generation controls. From the modeling perspective, the study contributes to the literature by proposing a model that applies to growing-type robots that are both pneumatic and tendon driven while also accounting for the robot shaft bending stiffness and EE statics. Secondly, the model utilizes a pinch roller drive mechanism force generation model developed for the proposed robotic system [12].

6.2. Outlook and Future Work

Based on the future expectation for colonoscopy, as discussed in the literature, improvements presented by the proposed system support the method to be a candidate for future colonoscopy application that meets the competency criteria. In this study, a small-scale robot with the dimensions of the conventional colonoscope has been developed, however not validated due to the unavailability of small size tubings. Future work will be to validate the concept at a small scale using medical colon models or clinical animal experiments. The proposed system can be further used for inspection purposes on confined spaces, or material transportation to the inaccessible areas. The soft structure of the proposed robotic system is advantageous for the applications where the robot's surrounding environment is prone to damage. For example this system may be an alternative for the robot that performs inspection in space under delicate thermal blankets [63], and gas turbine parts which are sensitive to any surface defect [64]. The growing type actuation approach allows the proposed robotic system to grow to long distances. This advantage of the system may be utilized for pipe inspection and search and rescue missions in confined areas.

REFERENCES

1. Organization, W. H., *2018 Cancer Statistics*, 2018, <https://www.who.int>.
2. Ferlay, J., I. Soerjomataram and M. Evrik, “Cancer Incidence and Mortality Worldwide.”, *GLOBOCAN, International Agency for Research on Cancer*, 2013.
3. Siegel, R., K. Miller, G. Sauer, S. Fedewa, L. Butterly, J. Anderson and J. Ahmedin, “Colorectal Cancer Statistics, 2020”, *CA CANCER J CLIN*, pp. 1–20, 2020.
4. Arnold, M., M. Sierra, M. Laversanne, I. Soerjomataram, A. Jemal and F. Bray, “Global patterns and trends in colorectal cancer incidence and mortality”, *Gut*, pp. 1–9, 2016.
5. Leggett, B. and D. Hewett, “Colorectal cancer screening”, *International Medicine Journal*, pp. 6–15, 2015.
6. Valdastrì, P., M. Simi and R. Webster, “Advanced Technologies for Gastrointestinal Endoscopy”, *Annual Review of Biomedical Engineering*, pp. 397–429, 2015.
7. Eliakim, R., K. Yassin, Y. Niv, Y. Metzge, J. Lachter and E. Gal, “Prospective multicenter performance evaluation of the second-generation colon capsule compared with colonoscopy”, *Endoscopy*, pp. 1026–1031, 2009.
8. Lin, J., P. MA, L. Perude, C. Rutter, E. Webber, E. O’Connor and E. Whitlock, “Screening for Colorectal Cancer: Updated Evidence Report and Systematic Review for the US Preventive Services Task Force”, *The journal of the American Medical Association (JAMA)*, Vol. 12, pp. 23–32, 2016.
9. Whitlock, E., J. Lin, E. Liles, T. Beil and R. Fu, “Screening for Colorectal Cancer: Updated Evidence Report and Systematic Review for the US Preventive Services

- Task Force”, *American College of Physicians, Clinical Guidelines, Annals of Internal Medicine*, 2008.
10. Talas, S., B. Baydere, T. Altinsoy, C. Tutcu and E. Samur, “Design and Development of a Growing Pneumatic Soft Robot”, *Soft Robotics*, Vol. 7, pp. 1–14, 2020.
 11. Tutcu, C., B. Baydere, S. Talas and E. Samur, “Quasi-static modeling of a novel growing soft-continuum robot”, *The International Journal of Robotics Research*, pp. 1–13, 2019.
 12. Baydere, B., S. Talas and E. Samur, “A novel highlyextensible 2-DOF pneumatic actuator for soft robotic applications”, *Sensors and Actuators A: Physical*, p. 84–94, 2018.
 13. Khashab, M., P. Pickhardt, D. Kim and D. Rex, “Colorectal anatomy in adults at computed tomography colonography: normal distribution and the effect of age, sex, and body mass index”, *Endoscopy*, Vol. 41, pp. 674–678, 2009.
 14. Harrold, E., “Anatomy of the caecum appendix and colon”, *Surgery*, pp. 1–29, 2010.
 15. Courtesy of Endoscopy Support Services, I., *Features of conventional colonoscope*, 2020, www.endoscopy.com.
 16. Soetikno, T., R. Asokkumar, T. Nguyen, T. DeSimio and T. Kaltenbach, “Holding and manipulating the endoscope: A user’s guide”, *Techniques in Gastrointestinal Endoscopy*, pp. 124–132, 2019.
 17. Ekkelenkamp, V., K. Dowler, R. Valori and P. Dunckley, “Patient comfort and quality in colonoscopy”, *World Journal of Gastroenterology*, pp. 2355–2361, 2013.
 18. Lee, I. and C. Wu, “Less patient discomfort by one-man colonoscopy examina-

- tion”, *Int. J. Clin. Pract*, pp. 635–638, 2006.
19. Shah, G., J. Brooker, C. Thapar, C. Williams and B. Saunders, “Patient Pain During Colonoscopy: An Analysis Using Real-Time Magnetic Endoscope Imaging”, *Endoscopy*, pp. 435–440, 2002.
 20. Loeve, A., P. Fockens and P. Breedveld, “Mechanical analysis of insertion problems and pain during colonoscopy: Why highly skill-dependent colonoscopy routines are necessary in the first place and how they may be avoided”, *Can J Gastroenterol*, pp. 293–302, 2013.
 21. Cotton, P., P. Connor, D. McGee, P. Jowell, N. Nickl, S. Schutz and E. Libby, “Colonoscopy: practice variation among 69 hospital-based endoscopists”, *Gastrointestinal Endoscopy*, pp. 352–357, 2003.
 22. Hull, T. and J. Church, “Colonoscopy-how difficult, how painful?”, *Surgical Endoscopy*, pp. 784–787, 1994.
 23. Rex, D., J. Petrini, T. Baron, A. Chak, J. Cohen, S. Deal and I. Pike, “Quality Indicators for Colonoscopy”, *Am J Gastroenterol*, pp. 873–885, 2006.
 24. Khanicheh, A. and A. Shergill, “Endoscope design for the future”, *Techniques in Gastrointestinal Endoscopy*, pp. 167–173, 2019.
 25. Appeleyard, M., C. Mosse, T. Mills, D. Bell, F. Castillo and P. Swain, “The measurement of forces exerted during colonoscopy”, *Gastrointestinal Endoscopy*, pp. 237–240, 2000.
 26. Ridditid, W., G. Cote, W. Leung, R. Buschbacher, S. Lynch, E. Fogel, J. Watkins, G. Lehman, S. Sherman and L. McHenry, “Prevalence and risk factors for musculoskeletal injuries related to endoscopy”, *Clinical Endoscopy*, pp. 294–302, 2015.
 27. Lau, K., Y. Leung, Y. Yam and P. Chiu, *Applications of Flexible Robots in Endo-*

- scopic Surgery. In T. C. Kong. Handbook of Robotic and Image-Guided Surgery, Elsevier, Hong Kong, 2020.*
28. Yeung, P. and P. Chiu, “Application of robotics in gastrointestinal endoscopy: A review”, *World Journal of Gastroenterology*, pp. 1811–1825, 2016.
 29. Phee, S., S. Low, V. Huynh, A. Kencana, Z. Sun and K. Yang, “Master And Slave Transluminal Endoscopic Robot (MASTER) for Natural Orifice Transluminal Endoscopic Surgery (NOTES)”, *31st Annual International Conference of the IEEE EMBS*, pp. 1192–1195, 2009.
 30. Suzuki, N., A. Hattori, K. Tanoue, S. Ieiri, K. Konishi, M. Tomikawa and M. Hashizume, “Scorpion Shaped Endoscopic Surgical Robot for NOTES and SPS With Augmented Reality Functions”, *MIAR*, pp. 541–550, 2010.
 31. M. Diana, M., H. Chung, K. Hao, B. Dallemange, N. Demartines and J. Marescaux, “Endoluminal surgical triangulation: overcoming challenges of colonic endoscopic submucosal dissections using a novel flexible endoscopic surgical platform: feasibility study in a porcine model”, *Surgical Endoscopy*, 2013.
 32. Swanstorm, L., R. Kozarek, P. Pasricha, S. Gross, D. Birkett, P. Park and P. Swain, “Development of a New Access Device for Transgastric Surgery”, *Journal of Gastrointestinal Surgery*, pp. 1129–1137, 2005.
 33. Shike, M., Z. Fireman, R. Eliakim, O. Segol, A. Sloyer, L. Cohen and A. Repici, “New Technology ColonoSight”, *OMED Colorectal Cancer Screening Meeting*, 2015.
 34. Gluck, N., A. Melhem, Z. Halpern, K. Mergener and E. Santo, “A novel self-propelled disposable colonoscope is effective for colonoscopy in humans”, *Gastrointestinal Endoscopy*, pp. 998–1004, 2016.
 35. Eickhoff, A., J. Dam, R. Jakobs, V. Kudis, D. Hartmann, M. Ulrich, M. Damian

- and M. Riemann, “Computer-Assisted Colonoscopy (The NeoGuide Endoscopy System): Results of the First Human Clinical Trial (“PACE Study”)”, *American Journal of Gastroenterology*, pp. 261–266, 2007.
36. Roesch, T., A. Adler, H. Pohl, E. Wettschureck, M. Koch, B. Wiedenmann and N. Hoepffner, “A prospective pilot study to assess technical performance of a new single use colonoscope with inverted sleeve technology”, *Gastrointest Endos*, 2007.
 37. Groth, S., T. Rösch and N. Hoepffner, “High cecal intubation rates with a new computer-assisted colonoscope: a feasibility study”, *Am J Gastroenterol*, pp. 1075–1080, 2011.
 38. Johnson, P., C. Serrano, M. Castro, R. Kuenzler, H. Choset and S. Tully, “Demonstration of Transoral Surgery in Cadaveric Specimens with the Medrobotics Flex System”, *Laryngoscope*, pp. 1168–1172, 2013.
 39. Medrobotics, “Flex robotic system”, *www.medrobotics.com*, 2020.
 40. Lau, K., Y. Leung, Y. Yam and P. Chiu, *Implementation of Novel Robotic Systems in Colorectal Surgery. In C. Clinic, Handbook of Robotic and Image-Guided Surgery*, Elsevier, Cleveland, 2020.
 41. Shang, J., D. Noonan, C. Payne, J. Clark, M. Sodergren and A. Darzi, “An Articulated Universal Joint Based Flexible Access Robot for Minimally Invasive Surgery”, *IEEE International Conference on Robotics and Automation (ICRA)*, pp. 1147–1152, 2011.
 42. Chen, G., M. Pham and T. Redarce, “Sensor-based guidance control of a continuum robot for a semi-autonomous colonoscopy”, *Robotics and Autonomous Systems*, pp. 712–721, 2009.
 43. Sars, V. D., S. Haliyo and J. Szewczyk, “A practical approach to the design and control of active endoscopes”, *Mechatronics*, pp. 251–264, 2010.

44. Cosentino, F., E. Tumino, G. Passoni, E. Morandi and A. Capria, “Functional evaluation of endotics system, a new disposable self-propelled robotic colonoscope: in vitro tests and clinical trial”, *International Journal of Artificial Organs*, pp. 517–527, 2009.
45. Consentino, F., E. Tumino, G. P. A. Rigante, R. Barbera, A. Tauro and P. Cosentino, “Robotic colonoscopy”, *Colonoscopy*, pp. 517–527, 2009.
46. Bernth, J. E., A. Arezzo and H. Liu, “A Novel Robotic Meshworm with Segment-Bending Anchoring for Colonoscopy”, *IEEE Robotics and Automation Letters*, pp. 1–7, 2017.
47. Ortega, A., L. Pearson and M. E. Rentschler, “Design, modeling and control of a SMA-actuated biomimetic robot with novel functional skin”, *Proceedings of the IEEE International Conference on Robotics and Automation*, pp. 4338–4345, 2017.
48. Wang, K., J. Ma, F. Wang, Z. Wang, G. Yan and Y. Zhou, “Full-driving soft robotic colonoscope in compliant colon tissue”, *Med. Eng. Technol.*, pp. 662–669, 2017.
49. Yamamoto, T., M. Konyo, K. Tadakuma and S. Tadokoro, “High-speed sliding-inchworm motion mechanism with expansion-type pneumatic hollow-shaft actuators in-pipe inspections”, *Mechatronics*, pp. 101–114, 2018.
50. Kim, D., D. Lee, S. Joe, B. Lee and B. Kim, “The flexible caterpillar based robotic colonoscope actuated by an external motor through a flexible shaft”, *Med. Eng. Technol.*, pp. 4415–4420, 2014.
51. Formosa, G., J. Prendergast, S. Edmundowicz and M. Rentschler, “Soft material adhesion characterizat on for in vivo locomotion of robotic capsule endoscopes”, *IEEE Trans. Robot.*, pp. 545–552, 2019.

52. Norton, J. C., P. R. Slawinski, H. S. Lay, J. W. Martin, B. F. Cox, G. Cummins, M. P. Y. Desmulliez, R. E. Clutton, K. L. Obstein, S. Cochran and P. Valdastri, “Intelligent magnetic manipulation for gastrointestinal ultrasound”, *Medical Robots*, pp. 1–13, 2019.
53. Iddan, G., G. Meron, A. Glukhovsky and P. Swain, “Wireless capsule endoscopy”, *Nature*, p. 417, 2000.
54. Redondo-Cerezo, E., A. D. Sanchez-Capilla, P. D. L. Torre-Rubio and J. D. Teresa, “Wireless capsule endoscopy: Perspectives beyond gastrointestinal bleeding”, *World Journal of Gastroenterology*, pp. 15664–15673, 2014.
55. Schoofs, N., J. Deviere and A. V. Gossum, “PillCam colon capsule endoscopy compared with colonoscopy for colorectal tumor diagnosis: a prospective pilot study”, *Endoscopy*, pp. 971–977, 2006.
56. Delvaux, M., M. Frederic, I. Fassler and G. Gay, “Does the Colonic Capsule PillCam Colon Efficiently Screen Patients Who Would Deserve a Complete Colonoscopy for Colo-Rectal Cancer Screening?”, *Gastrointestinal Endoscopy*, Vol. 67, pp. 132–149, 2008.
57. Delvaux, M. and G. Gay, “Capsule Endoscopy: Technique and indications”, *Best Practice & Research Clinical Gastroenterology*, pp. 813–837, 2008.
58. Woods, S. and T. G. Constandinou, “Wireless capsule endoscope for targeted drug delivery: mechanics and design considerations”, *IEEE Trans Biomed Eng*, pp. 945–953, 2013.
59. Gao, M., C. Hu, Z. Chen, H. Zhang and S. Liu, “Design and fabrication of a magnetic propulsion system”, *IEEE Trans Biomed Eng*, pp. 2891–2902, 2010.
60. Gorlewicz, J., S. Battaglia, B. Smith, G. Ciuti, J. Gerding, A. Manciaci, K. Obstein, P. Valdastri and R. Webster, “Wireless insufflation of the gastrointestinal

- tract”, *IEEE Trans Biomed Eng*, pp. 1225–1233, 2013.
61. van der Stap, N., E. Rozeboom, H. Pullens and F. van der Heijden, “Feasibility of automated target centralization in colonoscopy”, *Int J CARS*, pp. 25–35, 2015.
 62. Santiago, J., I. Walker and I. Godage, “Continuum robots for space applications based on layer-jamming scales with stiffening capability”, *IEEE Aerospace Conference*, p. 1–13, 2015.
 63. Mehling, J., M. Diftler, M. Chu and M. Valvo, “A minimally invasive tendril robot for in-space inspection”, *The First IEEE/RAS-EMBS International Conference on Biomedical Robotics and Biomechatronics, 2006 (BioRob 2006)*, p. 690–695, 2006.
 64. Dong, X., D. Axinte and D. Palmer, “Development of a slender continuum robotic system for on-wing inspection/repair of gas turbine engines”, *Robotics and Computer-Integrated Manufacturing*, p. 218–229, 2017.
 65. Wolf, A., H. Brown and R. Casciola, “A mobile hyper redundant mechanism for search and rescue tasks”, *Proceedings 2003 IEEE/RSJ International Conference on Intelligent Robots and Systems (IROS 2003)*, p. 2889–2895, 2003.
 66. Burgner-Kahrs, J., D. Rucker and H. Choset, “Continuum robots for medical applications: A survey”, *IEEE Transactions on Robotics*, p. 1261–1280, 2015.
 67. Dupont, P., J. Lock, B. Itkowitz and E. Butler, “Design and control of concentric-tube robots”, *IEEE Transactions on Robotics*, p. 209–225, 2010.
 68. Hadi, A., H. Akbari, B. Tarvirdizadeh and K. Alipour, “Developing a novel continuum module actuated by shape memory alloys”, *Sensors and Actuators A: Physical*, p. 90–102, 2016.
 69. Hong, W., J. Liu, L. Xie and K. Li, “Design of the continuum robotic system for

- nasal minimally invasive surgery”, *IEEE International Conference on Real-time Computing and Robotics (RCAR)*, p. 388–391, 2017.
70. Li, Z., H. Ren, P. Chiu, R. Du and H. Yu, “A novel constrained wire-driven flexible mechanism and its kinematic analysis”, *Mechanism and Machine Theory*, p. 59–75, 2017.
 71. Li, J., Z. T. Z, J. Xiao, A. Kapadia, A. Bartow and I. Walker, “Autonomous continuum grasping”, *IEEE/RSJ International Conference on Intelligent Robots and Systems*, p. 4569–4576, 2013.
 72. Hawkes, E., L. Blumenschein, J. Greer and A. Okamura, “A soft robot that navigates its environment through growth”, *Science Robotics*, pp. 2–8, 2017.
 73. Aliff, M., S. Dohta, T. Akagi and H. Li, “Development of a simple-structured pneumatic robot arm and its control using low-cost embedded controller”, *Procedia Engineering*, p. 134–142, 2012.
 74. Maghooa, F., A. Stilli, Y. Noh, K. Althoefer and H. Wurdemann, “Tendon and pressure actuation for a bio-inspired manipulator based on an antagonistic principle”, *2015 IEEE International Conference on Robotics and Automation (ICRA)*, p. 2556–2561, 2015.
 75. McMahan, W., B. Jones and I. Walker, “Design and implementation of a multi-section continuum robot: Air-Octor”, *IEEE/RSJ International Conference on Intelligent Robots and Systems.*, p. 2578–2585, 2005.
 76. Yarbasi, E. and E. Samur, “Design and evaluation of a continuum robot with extendable balloons”, *Mechanical Sciences*, p. 51–60, 2018.
 77. Yukisawa, T., S. Nishikawa, R. Niiyama, Y. K. Y and Y. Kuniyoshi, “Ceiling continuum arm with extensible pneumatic actuators for desktop workspace”, *2018 IEEE International Conference on Soft Robotics (RoboSoft)*, p. 196–201, 2018.

78. Jones, B., W. McMahan and I. Walker, “Design and Analysis of a Novel Pneumatic Manipulator”, *International Federation of Automatic Control*, pp. 102–130, 2014.
79. Putzu, F., T. Abrar and K. Althoefer, “Plant-Inspired Soft Pneumatic Eversion Robot”, *International Conference on Biomedical Robotics and Biomechanics (Biorob)*, pp. 1–6, 2018.
80. Dehghani, H., C. Welch, A. Pourghodrat, C. Nelson, D. Oleynikov, P. Dasgupta and B. Terry, “Design and preliminary evaluation of a self-steering pneumatically driven colonoscopy robot”, *Journal of Medical Engineering & Technology*, pp. 2–14, 2017.
81. Hannan, M. and I. Walker, “Analysis and experiments with an elephant’s trunk robot”, *Advanced Robotics*, pp. 847–858, 2001.
82. Gravange, I., C. Rahn and I. Walker, “Large deflection dynamics and control for planar continuum robots”, *IEEE/ASME Transactions on Mechatronics*, pp. 99–307, 2003.
83. Camarillo, D., C. Milne, C. Carlson, M. Zinn and J. Salisbury, “Mechanics modeling of tendon-driven continuum manipulators”, *IEEE Trans. Robot.*, pp. 1262–1273, 2008.
84. Cianchetti, M., T. Ranzani, G. Gerboni, T. Nanayakkara, K. Althoefer, P. Dasgupta and A. Menciassi, “Soft Robotics Technologies to Address Shortcomings in Today’s Minimally Invasive Surgery: The STIFF-FLOP Approach”, *Soft Robotics*, pp. 122–131, 2014.
85. Arezzo, A., Y. Mintz, M. Ettore, S. Arolfo, M. Bonino, G. Gerboni, M. Braccadoro, M. Cianchetti, A. Menciassi, H. Wurdemann, Y. Noh, K. Althoefer, J. Fras, J. Glowka, Z. Nawrat, G. Cassidy, R. Walker and M. Morino, “Total

- mesorectal excision using a soft and flexible robotic arm: a feasibility study in cadaver models”, *Surg Endosc*, pp. 1–10, 2016.
86. Shiva, A., A. Stilli, Y. Noh, A. Faragasso, I. D. Falco, G. Gerboni, M. Cianchetti, A. Menciassi, K. Althoefer and H. A. Wurdemann, “Tendon-based stiffening for a pneumatically actuated soft manipulator”, *IEEE Robotics and Automation Letters*, pp. 1–6, 2016.
 87. Kim, Y., S. Cheng and S. Kim, “A novel layer jamming mechanism with tunable stiffness capability for minimally invasive surgery”, *IEEE Trans Robot*, pp. 1031–1042, 2013.
 88. Li, Y., Y. Chen and Y. Yang, “Passive particle jamming and its stiffening of soft robotic grippers”, *IEEE Trans Robot*, pp. 446–455, 2017.
 89. Mori, Y., H. Tsukagoshi and A. Kitagawa, “Flexible Sliding Actuator Using A Flat Tube And Its Application To The Rescue Operation”, *IEEE International Conference on Robotics and Automation*, pp. 3266–3272, 2010.
 90. Yamamoto, T., M. Konyo and S. Tadokoro, “A High-speed Locomotion Mechanism Using Pneumatic Hollow-shaft Actuators for In-pipe Robots”, *IEEE/RSJ International Conference on Intelligent Robots and Systems (IROS)*, pp. 4724–4730, 2015.
 91. Hammond, Z., N. Usevitch, E. Hawkes and S. Follmer, “Pneumatic Reel Actuator: Design, Modeling, and Implementation”, *IEEE International Conference on Robotics and Automation (ICRA)*, pp. 628–633, 2017.
 92. Chikhaoui, M., K. Rabenorosoana and N. Andreff, “Kinematics and performance analysis of a novel concentric tube robotic structure with embedded soft micro-actuation”, *Mechanism and Machine Theory*, p. 234–254, 2016.
 93. Falkenhahn, V., T. Mahl, A. Hildebrandt, R. N. R and O. Sawodny, “Dynamic

- modeling of constant curvature continuum robots using the Euler–Lagrange formalism”, *IEEE International Conference on Intelligent Robots and Systems*, p. 2428–2433, 2014.
94. Jones, B. and I. Walker, “Kinematics for multisection continuum robots”, *IEEE Transactions on Robotics*, p. 43–55, 2006.
 95. Jones, B., W. McMahan and I. Walker, “Design and analysis of a novel pneumatic manipulator”, *IFAC Proceedings Volumes*, p. 687–692, 2004.
 96. Luo, M., R. Yan and Z. Wan, “OriSnake: Design, fabrication, and experimental analysis of a 3-D origami snake robot”, *IEEE Robotics and Automation Letters*, p. 1993–1999, 2018.
 97. Mishra, A., A. Mondini and E. D. Dottore, “Modular continuum manipulator: Analysis and characterization of its basic module”, *Biomimetics*, p. 3, 2018.
 98. Neppalli, S., M. Csencsits, B. Jones and I. Walker, “Closed-form inverse kinematics for continuum manipulators”, *Advanced Robotics*, p. 2077–2091, 2009.
 99. Webster, R. and B. Jones, “Design and kinematic modeling of constant curvature continuum robots: A review”, *The International Journal of Robotics Research*, p. 1661–1683, 2010.
 100. Rucker, D. and R. Webster, “Statics and dynamics of continuum robots with general tendon routing and external loading”, *IEEE Transactions on Robotics*, p. 1033–1044, 2011.
 101. Renda, F. and C. Laschi, “A general mechanical model for tendon-driven continuum manipulators”, *IEEE International Conference on Robotics and Automation*, p. 3813–3818, 2012.
 102. Trivedi, D., A. Lotfi and C. Rahn, “Geometrically exact models for soft robotic

- manipulators”, *IEEE Transactions on Robotics*, p. 773–780, 2008.
103. Mahl, T., A. Hildebrandt and O. Sawodny, “A variable curvature continuum kinematics for kinematic control of the bionic handling assistant”, *IEEE Transactions on Robotics*, p. 935–949, 2008.
 104. Lock, J., G. Laing, M. Mahvash and P. Dupont, “Quasistatic modeling of concentric tube robots with external loads”, *IEEE/RSJ International Conference on Intelligent Robots and Systems. IEEE*, p. 2325–2332, 2010.
 105. Mochiyama, H. and T. Suzuki, “Dynamical modelling of a hyper-flexible manipulator”, *Proceedings of the 41st SICE Annual Conference. SICE 2002*, p. 1505–1510, 2002.
 106. Dehghani, M. and S. Moosavian, “Modeling and control of a planar continuum robot”, *IEEE/ASME International Conference on Advanced Intelligent Mechatronics*, p. 966–971, 2011.
 107. Falkenhahn, V., T. Mahl, A. Hildebrandt, R. Neumann and O. Sawodny, “Dynamic modeling of bellows-actuated continuum robots using the Euler—Lagrange formalism”, *IEEE Transactions on Robotics*, p. 1483–1496, 2015.
 108. Slade, P., A. Gruebele, Z. Hammond, M. Raitor, A. Okamura and E. Hawkes, “Design of a soft catheter for low-force and constrained surgery”, *2017 IEEE/RSJ International Conference on Intelligent Robots and Systems (IROS)*, p. 174–180, 2017.
 109. Comer, R. and S. Levy, “Deflections of an inflated circular cylindrical cantilever beam”, *AIAA Journal*, p. 1652–1655, 1963.
 110. Altinsoy, T., B. Baydere, S. Talas, O. Erkan, C. Tutcu and E. Samur, “Design of an extensible colonoscopy robot”, *Hamlyn Symposium on Medical Robotics*, p. 25–26, 2018.

111. Dottore, E. D., A. Sadeghi, A. Mondini, V. Mattoli and B. Mazzolai, “Toward growing robots: A historical evolution from cellular to plant-inspired robotics”, *Frontiers in Robotics and AI*, pp. 5–16, 2018.
112. Sadeghi, A., A. Mondini and B. M. B., “Toward selfgrowing soft robots inspired by plant roots and based on additive manufacturing technologies”, *Soft Robotics*, p. 211–223, 2017.
113. Kayser, M., L.Cai and C.Bader, *Toward growing robots: Fiberbots: Design and digital fabrication of tubular structures using robot swarms. Robotic Fabrication in Architecture, Art and Design*, Springer, NewYork, 2018.
114. Li, C. and C. Rahn, “Design of continuous backbone, cabledriven robots”, *Journal of Mechanical Design*, p. 265, 2002.
115. van, A. L. and C. Wielgosz, “Bending and buckling of inflatable beams: Some new theoretical results”, *Thin-Walled Structures*, p. 1166–1187, 2005.
116. Cowper, G., “The shear coefficient in Timoshenko’s beam theory”, *Journal of Applied Mechanics*, p. 335–340, 1966.
117. Subramani, G. and M. Zinn, “Tackling friction-an analytical modeling approach to understanding friction in single tendon driven continuum manipulators”, *2015 IEEE International Conference on Robotics and Automation (ICRA). IEEE*, p. 610–617, 2015.
118. Rajasekaran, N., “A Nonlinear Constitutive Model for High Density Polyethylene at High Temperature”, *M.Sc. Thesis, University of Cincinnati*, 2015.
119. Baydere, B., “Design of a Highly-Extensible Pneumatic Actuator for Soft Robotic Applications”, *M.Sc. Thesis, Bogazici University*, 2019.
120. Talas, S., “Control System Design of a Highly-Extensible Soft Continuum Robot”,

M.Sc. Thesis, Bogazici University, 2019.

121. Korman, L., V. Egorov, S. Tsuryupa, B. Corbin and M. Sarvazyan, “Characterization of forces applied by endoscopist during colonoscopy by using a wireless colonoscopy force monitor”, *Clinical Endoscopy*, pp. 327–334, 2010.
122. Eickhoff, A., R. Jakobs, A. Kamal, S. Mermash, J. Riemann and J. Dam, “In vitro evaluation of forces exerted by a new computer-assisted colonoscope (the NeoGuide Endoscopy System)”, *Endoscopy*, pp. 1224–1229, 2006.
123. Yeung, C., J. Cheung and B. Sreedhar, “Emerging next-generation robotic colonoscopy systems towards painless colonoscopy”, *Digestive Diseases*, pp. 196–205, 2019.
124. FDA, *FDA Overview of Device Regulation*, 2020, <https://www.fda.gov>.
125. Altinsoy, T., “Design of an Extensible Colonoscope”, *M.Sc. Thesis, Bogazici University, 2019.*

APPENDIX A: BENDING STIFFNESS EQUATION OF THE INFLATED BEAM

Deflection of the inflated tubing under pure moment loading is derived from the equations given in [115] as given in Equation A.1, and Equation A.2

$$V_{,x} = \frac{P + kGA_0}{N^0 + kGA_0} \theta - \frac{C}{N^0 + kGA_0} \quad (\text{A.1})$$

$$\left(E + \frac{N^0}{A_0} \right) I_0 \theta_{,xx} + \frac{F + kGA_0}{N^0 + kGA_0} (P - N^0) \theta = -\mu + C \frac{F + kGA_0}{N^0 + kGA_0} \quad (\text{A.2})$$

From the equations given in [115] equilibrium equations are solved with following boundary conditions.

$$M(0) = M(l_0) = M_b \quad (\text{A.3})$$

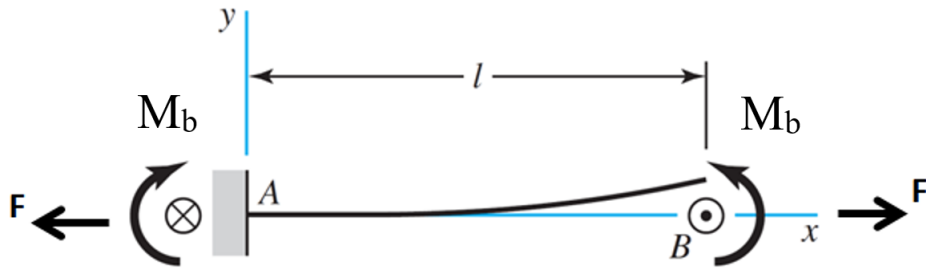


Figure A.1. Inflated beam FBD.

$$\left(E + \frac{N^0(0)}{A_0}\right) I_0 \theta_{,x}(0) = M_b \quad (\text{A.4})$$

$$\left(E + \frac{N^0(l_0)}{A_0}\right) I_0 \theta_{,x}(l_0) = M_b \quad (\text{A.5})$$

$$N^0(0) = N^0(l_0) = F \quad (\text{A.6})$$

Boundary in Equation A.6 is applied on the Equation A.1, and Equation A.2 and following equilibrium equations are obtained. Where C is the constant of integration.

$$V_{,x} = \theta - \frac{C}{F_p + kGA_0} \quad (\text{A.7})$$

$$C = \left(E + \frac{F_p}{A_0}\right) I_0 \theta_{,xx} \quad (\text{A.8})$$

Equation A.8 is integrated and BCs are applied and following is obtained

$$\theta_{,x} = \frac{C}{\left(E + \frac{F_p}{A_0}\right)} + C_1 \quad (\text{A.9})$$

Constants of integration are as following where $C=0$

$$C_1 = \frac{M_b}{\left(E + \frac{F_p}{A_0}\right) I_0} \quad (\text{A.10})$$

By integrating Equation A.9 slope of bent inflated beam as a function of axial location is calculated as,

$$\theta(x) = \frac{M_b x}{\left(E + \frac{F_p}{A_0}\right) I_0} \quad (\text{A.11})$$

From Equation A.11 Relation between bending moment and tip calculated as

$$M_i = \frac{2\delta \left(E + \frac{F_p}{A_0}\right) I_0}{l_i^2} \quad (\text{A.12})$$

APPENDIX B: TENDON FRICTION FORCE

Tendon friction force equation is obtained taking the model developed in [117] as reference. Forces acting on the infinitesimal tendon element are shown in Figure B.1.

Sum of the forces in y direction is given as

$$dN - \sin\left(\frac{d\theta}{2}\right)T - \sin\left(\frac{d\theta}{2}\right)(T + dT) = 0 \quad (\text{B.1})$$

Sum of the forces in x direction is given as

$$df_u + \cos\left(\frac{d\theta}{2}\right)T - \cos\left(\frac{d\theta}{2}\right)(T + dT) = 0 \quad (\text{B.2})$$

Where $df_u = \mu dN$. For small θ $\cos\theta = 1$, $\sin\theta = \theta$, and $\lim_{\theta \rightarrow 0} dT d\theta = 0$, thus following relation is obtained

$$dT = T\mu d\theta \quad (\text{B.3})$$

Integrating this relation relation between tension at end effector T_e , and tension at the root T_0 is obtained as following.

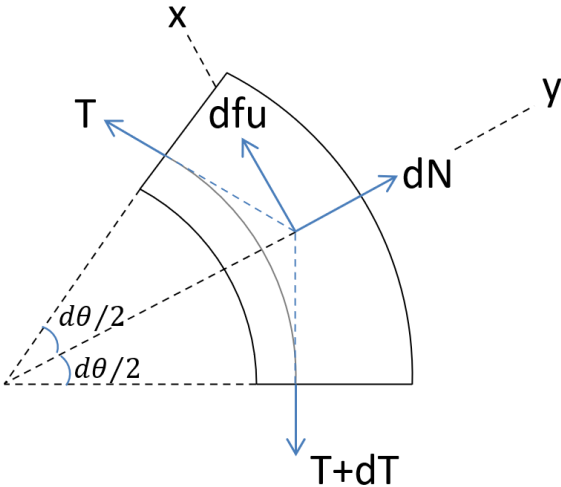


Figure B.1. Infinitesimal tendon element.

$$T_0 = T_e e^{\mu\theta} \tag{B.4}$$

APPENDIX C: COMPARISON OF ACTUATOR TUBINGS

Properties of various tubings tested for prototypes are shown in Table C.1. The table shows comparison between off the shelf medical tubings and fabricated double layer tubings in Bogazici University laboratory. Different than the tubings shown in Table 3.2 in Table C.1 off the shelf tubings that have length below 1000 mm is also shown, and the comparison is made to identify suitable material and cross-section dimensions independent of tubing length.

Table C.1. Actuator tubings tested for prototypes. Vendor information is not given for the tubings fabricated in house. The table also contains information for the off the shelf tubings that have length below 1000 mm. Dimension are in mm [119].

#	Code	Material	Vendor	OD	Thickness	Hardness
1	PA12(5)	Polyamide 12	Simeks	5	0.035	75D
2	PA12(10)	Polyamide 12	Simeks	10	0.035	75D
3	PEL	Pellethane	Lubrizol	4.572	0.254	80A
4	HDPE/L	HDPE+Latex	-	16	0.400	68D+35A
5	LDPE/L	LDPE+Latex	-	10	0.390	55D+35A
6	PA12/L(10)	PA12+Latex	-	10	0.3352	75D+35A
7	PA12/L(5)	PA12+Latex	-	5	0.335	75D+35A
8	PB72	Pebax	Vention	5.613	0.127	72D
9	PB55	Pebax	Vention	5.613	0.127	55D
10	PTFE	PTFE	Zeus	7.823	0.127	60D

PA12(5) and PA12(10) are the medical balloons manufactured by Simeks medical have flexibility per requirements of the application however show poor air seal characteristics. Although the wall thickness of PEL is high compared to PA12(5) and PA12(10) since it is manufactured from a soft material, this tubing meets the flexibility requirement. However, PEL has the worst force generation characteristics among other



Figure C.1. Actuator tubings tested as given in Table C.1.

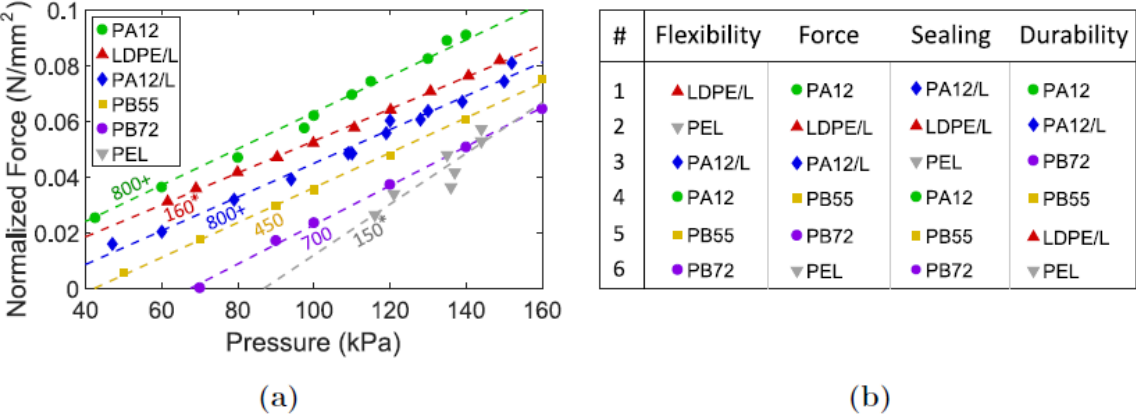


Figure C.2. Comparison of tubing force generation. Tests performed using 1D test setup. Force is normalized per the cross-section area that the pressure is acting on (a) Ranking of tubings per various significant application parameters [119].

samples as shown in Figure C.2 since the thick soft tubing is crushed between rollers and generating high friction force. Due to high stiffness of PB72 and PB55 required flexibility cannot be achieved for those samples. Among all LDPE/L which is a fabricated tubing is advantageous in terms of flexibility, force, and sealing. Although durability of LDPE/L is low, the tubing could be utilized by operating the robot at low pressures.

APPENDIX D: MAIN ROBOT CONTROL ALGORITHM

Control loops are assembled on a single code on the RTOS of the cRIO, which is directly connected to the FPGA. The state controller on LabVIEW has a GUI with buttons and numerical inputs for control, showing the sensor outputs such as tubing pressures and system state. System states are chosen from the GUI: 'forward,', 'backward', and 'stop'. The idle state is to make mechanical settings of the PRD actuator. In this state, the motors are disabled and free to rotate, inlet valves are closed, and exhaust valves are open to have unpressurized tubings. In the forward state, both motors are active, and inlet valves are open while the exhaust valves are closed. The backward state, motors are rotating in reverse direction such that deflated tubing is retrieved, and exhaust valves are controlled with PWM signal to release the extra pressure caused by the decrease in the volume. In the stop state, the inlet valves are open, the exhaust valves are closed, and the motors are enabled, however broke to prevent motion.

The control loop period is calculated by Equation D.1 as given in, where T_m is the control loop period, ω is the motor speed, and μ is the step resolution.

$$T_m = \mu \frac{1.5 \times 10^5}{\omega} \quad (\text{D.1})$$

The teleoperation controller is designed that is using omega 6 as the commanding device. The commanding device generates position output, orientation output that is given via rotation angles on two different axes, and push-button output. The position output is of omega 6 is mapped into real world coordinates which is $\pm 60\text{mm}$ from the workspace center of the device. Orientation angle outputs does not require any mapping and given as $\pm 100^\circ$ from the straight state of the knob.

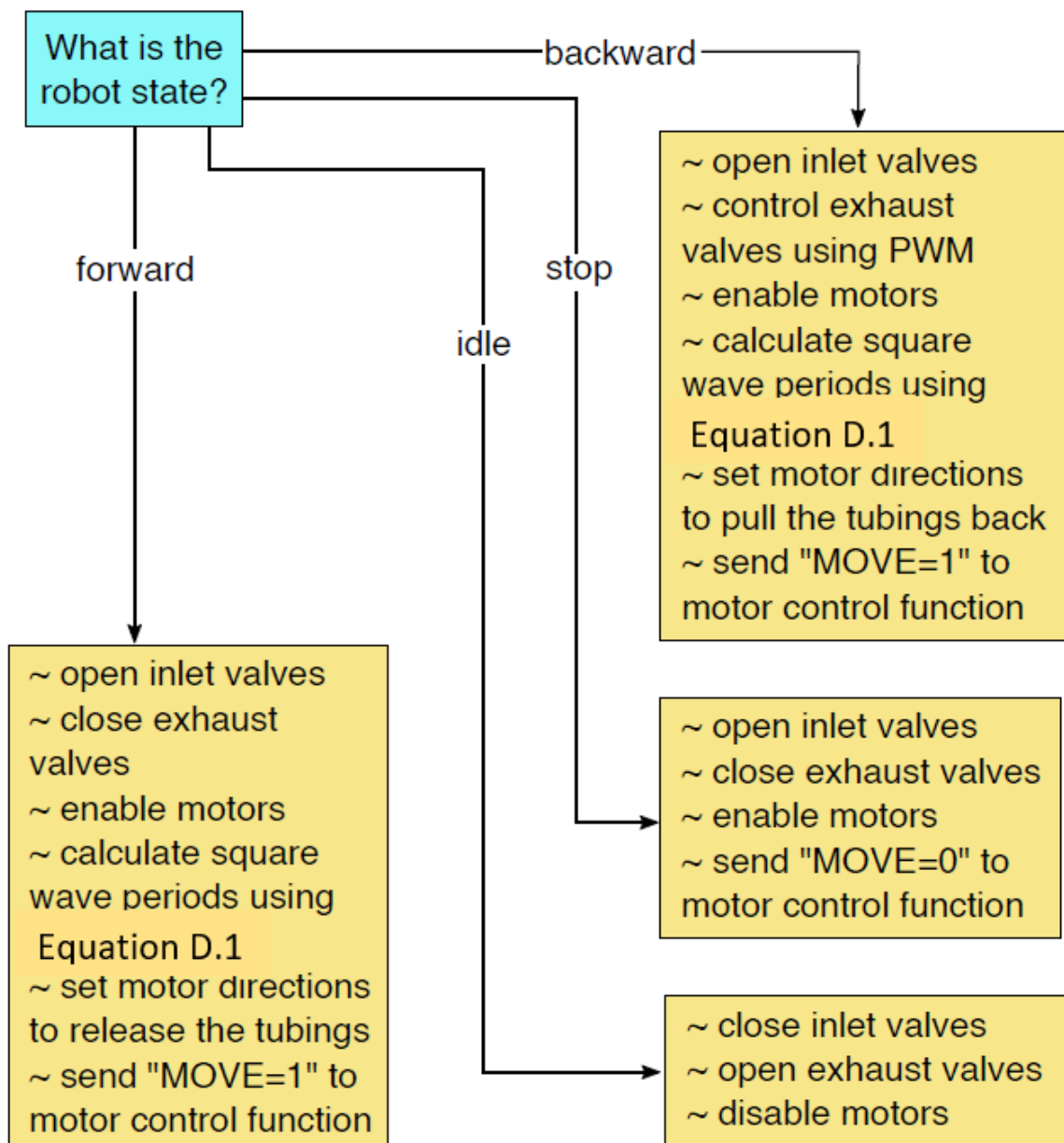


Figure D.1. Main state control algorithm [120].

APPENDIX E: TECHNICAL DRAWINGS



Figure E.1. Small scale end effector roller technical drawing.

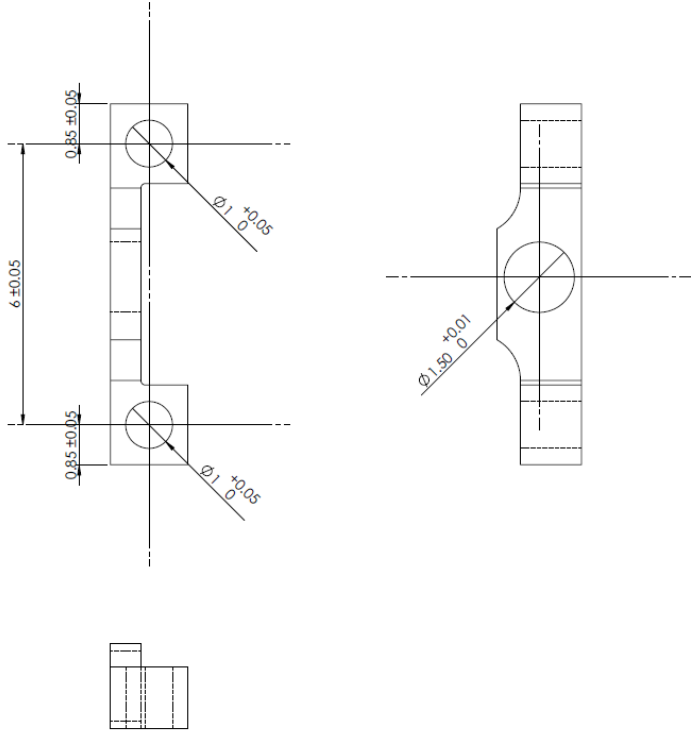


Figure E.2. Small scale end effector moving base technical drawing.

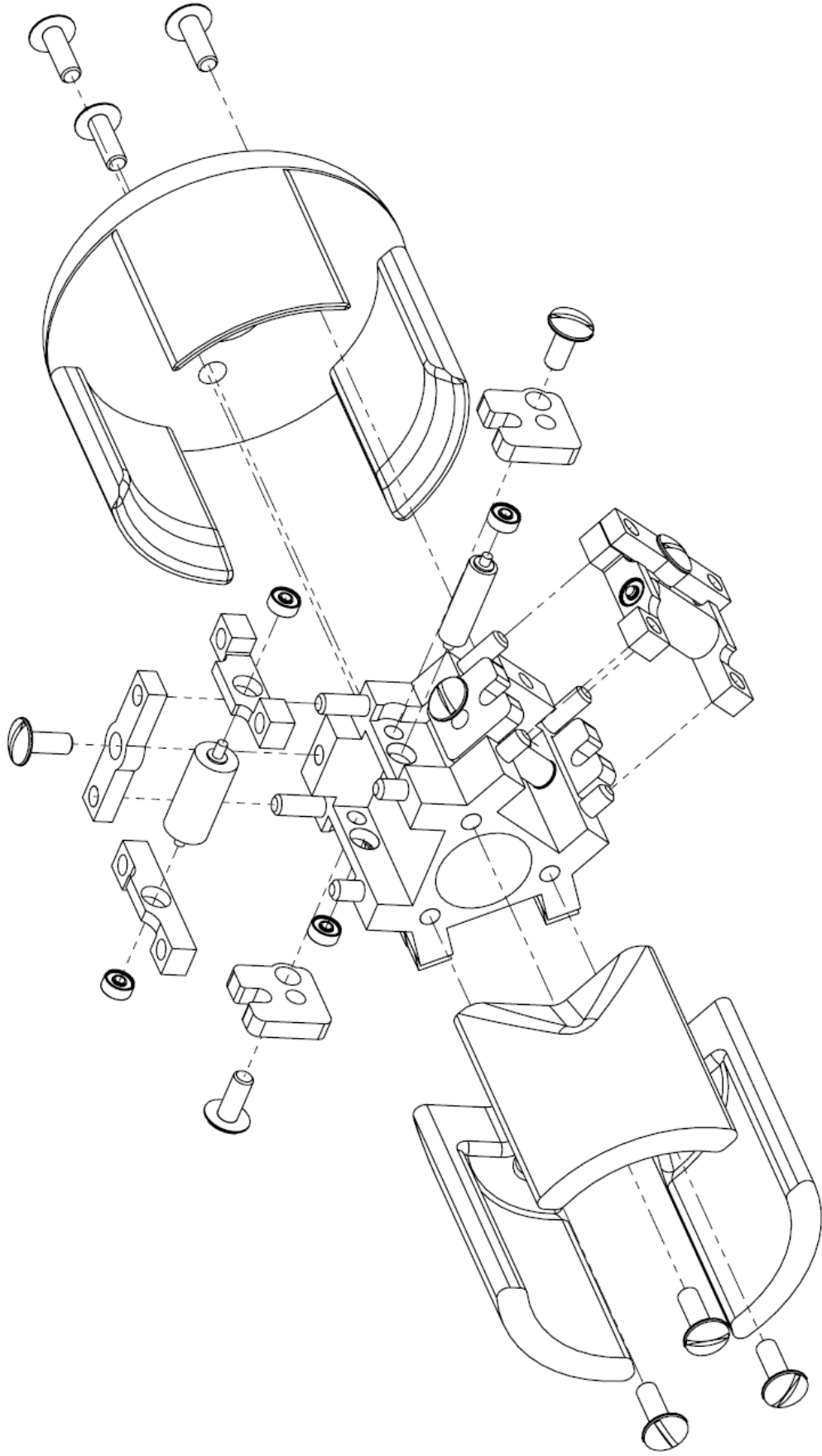


Figure E.3. Exploded view of small scale end effector [125].

